Summer 2016

Three-dimensional printing and nanotechnology for enhanced implantable materials

Karthik Kumar Tappa

THREE-DIMENSIONAL PRINTING AND NANOTECHNOLOGY FOR ENHANCED IMPLANTABLE MATERIALS

by

Karthik Kumar Tappa, B.Pharm., M.S.

A Dissertation Presented in Partial Fulfillment
of the Requirements of the Degree
Doctor of Philosophy

COLLEGE OF ENGINEERING AND SCIENCE
LOUISIANA TECH UNIVERSITY

August 2016

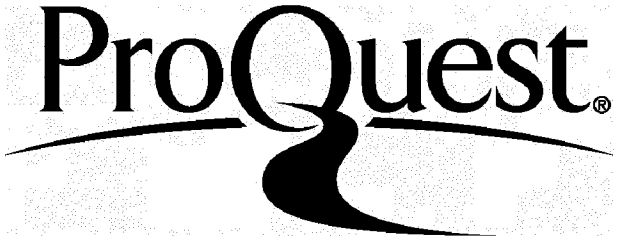

LOUISIANA TECH UNIVERSITY

THE GRADUATE SCHOOL

MAY 11, 2016
Date

We hereby recommend that the dissertation prepared under our supervision by **Karthik Kumar Tappa,** B.Pharm., M.S.

entitled **Three-Dimensional Printing and Nanotechnology for Enhanced Implantable Materials**

be accepted in partial fulfillment of the requirements for the Degree of **Doctor of Philosophy in Biomedical Engineering**

Supervisor of Dissertation Research

Head of Department
Biomedical Engineering
Department

Recommendation concurred in:

Advisory Committee

Approved:

Director of Graduate Studies

Dean of the College

Approved:

Dean of the Graduate School

ABSTRACT

Orthopedic and oro-maxillofacial implants have revolutionized treatment of bone diseases and fractures. Currently available metallic implants have been in clinical use for more than 40 years and have proved medically efficacious. However, several drawbacks remain, such as excessive stiffness, accumulation of metal ions in surrounding tissue, growth restriction, required removal/revision surgery, inability to carry drugs, and susceptibility to infection. The need for additional revision surgery increases financial costs and prolongs recovery time for patients. These metallic implants are bulk manufactured and often do not meet patient's requirements. A surgeon must machine (cut, weld, trim or drill holes) them in order to best suit the patient specifications.

Over the past few decades, attempts have been made to replace these metallic implants with suitable biodegradable materials to prevent secondary/revision surgery. Recent advances in biomaterials have shown multiple uses for lactic acid polymers in bone implant technology. However, a targeted/localized drug delivery system needs to be incorporated in these polymers, and they need to be customized to treat orthopedic implant-related infections and other bone diseases such as osteomyelitis, osteosarcoma and osteoporosis. Rapid Prototyping (RP) using additive manufacturing (AM) or 3D printing could allow customization of constructs for personalized medicine. The goal of this study was to engineer customizable and biodegradable implant materials that can elute bioactive compounds for personalized medicine and targeted drug delivery.

Post-operative infections are the most common complications following dental, orthopedic and bone implant surgeries. Preventing post-surgical infections is therefore a critical need that current polymethylmethacrylate (PMMA) bone cements fail to address. Calcium Phosphate Cements (CPCs) are unique in their ability to crystallize calcium and phosphate salts into hydroxyapatite (HA) and hence is naturally osteoconductive. Due to its low mechanical strength, its use in implant fixation and bone repair is limited to non-load-bearing applications. Novel CPCs were formulated and were doped with drug loaded Halloysite Nanotubes (HNTs) to enhance their mechanical and anti-infective properties.

In this study we also explored the use of customized biopolymer filaments and 3D printing technology to treat bone diseases such as osteomyelitis, osteosarcoma, and osteoporosis. Biopolymer filaments were successfully loaded with antibiotics, chemotherapeutics and hormones (female sex hormones). Using a Fused Deposition Modeling (FDM)-based 3D printer, these customized filaments were fabricating into 3D scaffolds. Constructs with variable mechanical strengths and porosities were successfully designed and 3D printed. Scanning electron microscopy was used to study the surface architecture of the scaffolds. Compression and flexural testing was conducted for testing the mechanical strength of the constructs. Bacterial and suitable cell culture studies were applied to test bioactivity of the constructs. From above experiments, this study showed that 3D printing technology can be used to fabricate bioactive biopolymers for personalized medicine and localized drug delivery.

APPROVAL FOR SCHOLARLY DISSEMINATION

The author grants to the Prescott Memorial Library of Louisiana Tech University the right to reproduce, by appropriate methods, upon request, any or all portions of this Dissertation. It is understood that "proper request" consists of the agreement, on the part of the requesting party, that said reproduction is for his personal use and that subsequent reproduction will not occur without written approval of the author of this Dissertation. Further, any portions of the Dissertation used in books, papers, and other works must be appropriately referenced to this Dissertation.

Finally, the author of this Dissertation reserves the right to publish freely, in the literature, at any time, any or all portions of this Dissertation.

Author 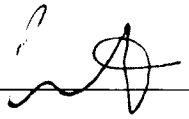

Date 07/20/2016

DEDICATION

To my parents, Vijaya Kumar Tappa and Sudha Rani Tappa, brother, Kranthi Kumar Tappa, sister-in-law, Vasantha Veena and niece, Hethvika Tappa.

TABLE OF CONTENTS

ABSTRACT iii

DEDICATION vi

LIST OF TABLES xii

LIST OF FIGURES xiii

ACKNOWLEDGMENTS xviii

CHAPTER 1 INTRODUCTION 1

1.1 Bone Implant Technology 1

1.2 Need for Improved Implant Technology 2

1.3 Objectives 5

1.3.1 CPCs Doped with HNTs 6

1.3.2 3D Printing Antibiotic and Chemotherapeutic Constructs 7

1.3.3 3D Printing Hormones 8

1.4 Organization of Dissertation 8

CHAPTER 2 BACKGROUND 9

2.1 Bone 9

2.1.1 Types of Bone 9

2.1.2 Bone Cells 10

2.1.3 Extracellular Matrix (ECM) 11

2.2 Osteosarcoma 11

2.3 Osteomyelitis 13

2.4 Osteoporosis 15

2.5 Calcium Phosphate Bone Cements 17
2.6 Nanoparticle Technology 19
2.7 Additive Manufacturing 21
2.8 Fused Deposition Modeling (FDM) 25
2.8.1 Stereolithography Files (STL) 26
2.8.2 Computer Aided Design (CAD) 27
2.8.3 Slicer 27
2.9 Applications of 3D Printing in Implant Technology 28
2.9.1 Bioprinting Tissues and Organs 29
2.9.2 Customized Implants and Prostheses 30
2.9.3 Anatomical Models and Tools for Surgical Preparations 31
2.10 Biopolymers 31
2.10.1 Types of Biopolymers 32
2.10.1.1 Natural Biodegradable Polymers 32
2.10.1.2 Synthetic Biodegradable Polymers 33
CHAPTER 3 NANO-ENHANCED CALCIUM PHOSPHATE BONE CEMENTS 35
3.1 Materials and Methods 36
3.1.1 Materials 36
3.1.2 Formulation of CPCs 36
3.1.3 Loading HNTs 39
3.1.4 Mechanical Properties 40
3.1.5 Scanning Electron Microscopy (SEM) 41
3.1.6 XTT Assay 41
3.1.7 Drug Release Profile 42
3.1.8 Bacterial Cultures 43

3.2 Results and Discussion 44
3.2.1 Mechanical Properties 44
3.2.1.1 Compression Strength 44
3.2.1.2 Flexural Strength 48
3.2.2 Morphology of CPC Scaffolds 49
3.2.3 XTT Assay 51
3.2.4 Drug Release Profile 52
3.2.5 Bacterial Culture 55
3.3 Conclusions and Future Work 58
3.3.1 Conclusions 58
3.3.2 Future Work 59
CHAPTER 4 3D PRINTING ANTIBIOTIC AND CHEMOTHERAPEUTIC LOADED BIODEGRADABLE SCAFFOLDS 60
4.1 Introduction 60
4.2 Materials 61
4.2.1 Bioplastics 62
4.2.2 Computer Modeling 63
4.2.3 Filament Extruder 64
4.2.4 3D Printer 65
4.2.5 3D Scanner 67
4.3 Extruding Drug Loaded Filaments 68
4.3.1 Coating Pellets with Drugs 69
4.3.2 Filament Extrusion 71
4.4 Optimization of 3D Printing Parameters 72
4.5 Scaffold Design and Fabrication 73
4.6 Thermal Decomposition Testing 74

4.7 Scaffold Characterization 74
4.7.1 Morphology 74
4.7.2 Mechanical Properties 74
4.7.3 Drug Release Profile 77
4.7.4 Bacterial Cultures 78
4.7.5 Osteosarcoma Cell Culture 79
4.7.6 Statistics 79
4.8 Results and Discussion 80
4.8.1 Scanning Electron Microscopy (SEM) 81
4.8.2 Mechanical Properties 83
4.8.3 Drug Release Profiles 87
4.8.4 Bacterial Culture 90
4.8.5 Osteosarcoma Cell Culture 94
4.8.6 Scanning Bone Defects 96
4.9 Conclusion 98
CHAPTER 5 3D PRINTING HORMONES LOADED BIODEGRADABLE CONSTRUCTS 100
5.1 Introduction 100
5.2 Materials 103
5.2.1 Bioplastics 104
5.2.2 Hormones 105
5.2.3 Micro-plate Reader 105
5.2.4 ELISA Kits for Hormone Quantification 106
5.2.5 Estrogen Receptor Luciferase Reporter Cell Line 106
5.3 Fabricating Hormone Loaded Scaffolds 106
5.3.1 Extruding Hormone Loaded Filaments 107

5.3.2 Optimizing 3D Printing Parameters 107
5.3.3 Scaffold Design and Fabrication 107
5.4 Scaffold Characterization 107
5.4.1 Morphology 108
5.4.2 Hormone Elution Profiles 108
5.4.3 Estrogen Receptor Luciferase Cell Culture 108
5.5 Statistical Analysis 109
5.6 Results and Discussion 109
5.6.1 Scanning Electron Microscopy (SEM) 110
5.6.2 Quantification through ELISA 112
5.6.3 *In vitro* Assay 116
5.7 Conclusions 117
CHAPTER 6 CONCLUSIONS AND FUTURE WORK 119
6.1 Conclusions 119
6.2 Future Work 121
6.2.1 Surgical Mesh 121
6.2.2 Live Vascular Grafts 122
APPENDIX A STANDARD GRAPHS FOR DRUG ELUTION PROFILES 124
APPENDIX B PROTOCOLS FOR CELL CULTURE TECHNIQUES 129
BIBLIOGRAPHY 132

LIST OF TABLES

Table 3-1: Formulation number, composition of calcium phosphate salts and type of setting liquid used 38

Table 3-2: Table showing the values of peak load and compression pressure for each specimen 45

Table 5-1: Concentration of E2 hormone released from PCL-E2 discs on Individual days. (mean ± SD, n = 3) 113

Table 5-2: Concentration of E3 hormone released from PCL-E3 discs on Individual days 115

LIST OF FIGURES

Figure 2-1: Types of rapid prototyping [69] 22

Figure 2-2: Selective Laser Sintering (SLS) 22

Figure 2-3: Stereolithography (SLA) 23

Figure 2-4: Fused Deposition Modeling (FDM) [74] 24

Figure 2-5: Laminated Object Manufacturing [75] 25

Figure 2-6: Steps involved in making a 3D object from a CAD model 26

Figure 2-7: A) 3D model of a cube, B) STL format of a cube, C) STL file of a complex design 27

Figure 3-1: Admet 2600 Dual Column Bench Top Universal Testing Machine 40

Figure 3-2: Stress-Strain curves for different trails of CPC constructs 46

Figure 3-3: Compressive strengths of CPC samples with different concentrations of HNTs (mean ± SD, n = 5). Statistical significant differences are marked with * for $p < 0.05$ [105, 106] 47

Figure 3-4: Flexural strengths of CPC samples with different concentration of HNTs (mean ± SD, n = 3). Statistical significant differences are marked with * for $p < 0.05$ [105, 106] 49

Figure 3-5: SEM of CPC scaffolds with different concentrations of HNTs. A) 0%, B) 5%, C) 10%, and D) 15% [105] 50

Figure 3-6: SEM showing cluster of HNTs on the surface of the CPC-HNT (5% wt) scaffolds. Image B was also used in Uday Jammalamadaka's dissertation [106] 50

Figure 3-7: Cell viability assessed in human osteoblast culture on different CPC-HNT scaffolds (mean ± SD, n = 6). Statistical significant differences are marked with * for $p < 0.05$ 51

Figure 3-8: Cumulative concentration of GS released from HNTs and CPC-HNT scaffolds (mean ± SD, n = 3) [105] 53

Figure 3-9: Cumulative concentration of NS released from HNTs and CPC-HNT scaffolds (mean ± SD, n = 3) [105] 54

Figure 3-10: Inhibition zones of CPCs loaded with different concentrations of HNT-GS against *E. coli* (A-B) *P. aeruginosa* (C-D) 55

Figure 3-11: Inhibition zones of CPCs loaded with different concentrations of HNT-NS against *E. coli* (A-B) and *P. aeruginosa* (C-D) 56

Figure 3-12: Inhibition diameters for *E. coli* and *P. aeruginosa* at different concentrations of HNT-GS in CPC scaffolds (mean ± SD, n = 3) 57

Figure 3-13: Inhibition diameters for *E. coli* and *P. aeruginosa* at different concentrations of HNT-NS in CPC scaffolds (mean ± SD, n = 3) 57

Figure 4-1: A bag of PLA pellets and its molecular structure 63

Figure 4-2: Solidworks 2015 interface showing a design of the stent 64

Figure 4-3: A) ExtrusionBot filament extruder, B) Piston based auger system inside ExtrusionBot 65

Figure 4-4: A) MakerBot Replicator 1st Generation, B) MakerBot Replicator 5th Generation 66

Figure 4-5: Screenshot of Makerware software showing customizable settings 67

Figure 4-6: Roland LP-250 desktop 3D scanner 68

Figure 4-7: The process of coating PLA pellets with drugs. A) Coating oil is added, B) Tube is vortexed, C) Pellets are transferred to a new tube, D) Drug is added, E) Tube is vortexed, F) Coated pellets are removed [117] 70

Figure 4-8: Drug coated PLA pellets. A-B) Control PLA, C-D) 1% wt GS coated pellets, E-F) 1% wt MTX coated pellets [117] 71

Figure 4-9: Printing PLA constructs with A) Different Infill ratios, B) Different Orientations 75

Figure 4-10: Printing PLA constructs. A) MTX-PLA mechanical testing samples, B) GS-PLA mechanical testing samples 76

Figure 4-11: Image showing three point bend testing performed on PLA samples 77

Figure 4-12: A) 1% wt GS-PLA catheters, B) 1% wt MTX-PLA catheter, compression cylinder and bead, C) 1% wt GS-PLA beads, D) 1% wt MTX-PLA beads 80

Figure 4-13: SEM of A) Control pellet, B) GS powder, C) 1% wt GS-PLA pellet, D) MTX pellet, E) 1% wt MTX-PLA pellet. Images D and E were also used in Jeffery Weisman's dissertation [117, 119] 81

Figure 4-14: SEM of A) Control filament, B) 1% wt GS-PLA filament, C) 5% wt GS-PLA filament, D) 1% wt MTX-PLA filament, E-F) MTX crystals on the surface of filament at different levels of magnification. Images D and F were also used in Jeffery Weisman's dissertation [117, 119] 82

Figure 4-15: SEM of A) 1% wt MTX-PLA bead, B) MTX powder on surface of the bead, C) 1% wt MTX-PLA catheter, D) 1% wt GS-PLA catheter, E) GS on the surface of the catheter, F) 1% wt GS-PLA bead. Images D-F were also used in Jeffery Weisman's dissertation [119] 83

Figure 4-16: Flexural strengths of PLA constructs printed in different infill ratios and orientations (mean ± SD, n = 5). Statistical significant differences are marked with * for $p < 0.05$ 84

Figure 4-17: Flexural strengths of control, GS and MTX-PLA constructs. (mean ± SD, n = 5). Statistical significant differences are marked with * for $p < 0.05$ 85

Figure 4-18: Stress-Strain curves for different trails of PLA constructs 86

Figure 4-19: Compression strengths of PLA constructs printed at different infill ratios and orientations (mean ± SD, n = 5). Statistical significant differences are marked with * for $p < 0.05$ 86

Figure 4-20: Compression strengths of control, GS and MTX-PLA constructs (mean ± SD, n = 5). Statistical significant differences are marked with * for $p < 0.05$ 87

Figure 4-21: Cumulative concentration of GS eluted from 3D printed PLA bead, catheter and hand mold PMMA bead (mean ± SD, n = 3) 88

Figure 4-22: Cumulative concentration of MTX released from 3D printed PLA catheters (mean ± SD, n = 3) 89

Figure 4-23: Cumulative concentration of MTX eluted from PMMA bead (mean ± SD, n = 3) 89

Figure 4-24: Zone of Inhibitions for GS heated at different temperatures on *E. coli* cultures A) Controlled uncooked, B) 175°C, C) 195°C, D) 205°C, E) 215°C, F) 225°C and G) 235°C 90

Figure 4-25: Zone of inhibition for GS heated at different temperatures (mean ± SD, n = 3) 91

Figure 4-26: Zone of Inhibitions for *E. coli* cultures A) PLA-GS pellet, B) PLA and PMMA filaments with and without GS, C) PLA and PMMA discs with and without GS. Image A was also used in Jeffery Weisman's dissertation 92

Figure 4-27: Zone of Inhibitions for PLA-GS bead and catheter on *E. coli* 93

Figure 4-28: A) 1 wt% tobramycin PMMA disc, B) 1 wt% tobramycin PLA disc, C) 2.5 wt% tobramycin PMMA disc, D) 2.5 wt% tobramycin PLA disc [119, 117] 93

Figure 4-29: Absorbance values of XTT assay performed on osteosarcoma cells with different MTX groups at day one (mean ± SD, n = 3) 94

Figure 4-30: Absorbance values of XTT assay performed on osteosarcoma cells with different PLA scaffolds enhanced with MTX (mean ± SD, n = 6) [117] 95

Figure 4-31: A) Cow femur with irregular bone defect, B) Cow femur with 6 mm diameter defects 1 wt% [119] 96

Figure 4-32: A) 3D raw scan of cow femur showing 360 degrees of defect in 180 degree image, B) CAD rendering of negative 6 mm diameter defect, C) CAD rendering of negative of irregular defect, D) 1wt% gentamicin print of irregular defect with control, E) MTX print of irregular defect. Images in A-D were also used in Jeffery Weisman's Dissertation 97

Figure 4-33: A) Femur with irregular defect, B) Femur with control-PLA fitted insert, C) Femur with GS-PLA fitted insert [119] 97

Figure 5-1: IUD positioned in the uterus [131] 102

Figure 5-2: Pessaries of different shapes and sizes [135] 103

Figure 5-3: SpectraMax M2e multimode multiplate reader 105

Figure 5-4: 3D printed constructs A) Control donut shaped pessary, B) Control gellhorn shaped pessary, C) Control IUD, D) Pessary printed combinations of filaments (red- PLA and white- PCL-E2), E) PCL-E1 IUD, and F) PCL-E2 IUD. 110

Figure 5-5: SEM images of A) E1, B) E2, C) E3 110

Figure 5-6: SEM images of A) E1, B) E2, C) E3 111

Figure 5-7: SEM images of (A,D) PCL-E1 Disc, (B,E) PCL-E2 Disc, (C,F) PCL-E3 Disc 112

Figure 5-8: Cumulative concentration of E2 released from PCL-E2 discs (mean ± SD, n = 3) 114

Figure 5-9: Cumulative concentration of E3 released from PCL-E3 discs (mean ± SD, n = 3) 116

Figure 5-10: RLU values of Estrogen receptor luciferase reporter cells incubated with different groups of E2 scaffolds (mean ± SD, n = 5)..... 117

Figure 6-1: A) 3D printed Plain PLA surgical mesh, B) zone of inhibition of 1%wt GS-PLA on *E. coli* bacterial plate..... 122

Figure 6-2: A) CAD model of vascular stent, B) 3D printed stent using PVA, C) Seeding cells on to the scaffold, D-E) Cells growing on the stent 123

Figure A-1: Standard graph used for calculating GS concentration for CPC samples.. 124

Figure A-2: Standard graph used for calculating NS concentration for CPC samples.. 125

Figure A-3: Standard graph used for calculating GS concentration from 3D printed constructs 126

Figure A-4: Standard graph used for calculating MTX concentration from PLA-MTX..... 126

Figure A-5: Standard graph used for calculating E2 concentration from PCL-E2 Discs..... 127

Figure A-6: Standard graph used for calculating E3 concentration from PCL-E3 discs..... 128

ACKNOWLEDGMENTS

I owe my sincere gratitude to all those who have made this dissertation possible, and because of whom my graduate experience has been one that I will cherish forever. Foremost, I would like to express my deepest gratitude to my advisor, Dr. David K. Mills, for his motivation, great enthusiasm, and immense knowledge. I have been amazingly fortunate to have such an advisor whose tremendous patience and continuous support helped me overcome many crisis situations. I am deeply grateful to my committee members, Dr. Steven A. Jones, Dr. Teresa A. Murray, Dr. Bryant Hollins, and Dr. William Campbell for their understanding, support and interest in this study.

My sincere thanks to Dr. Jeffery Weisman who went out of his way to help me understand, plan, and make this study successful, as well as Dr. Steven Alexander from LSU-HSC, Shreveport for his continuous support, encouragement, and valuable suggestions and discussions. I am also thankful to Mr. Udayabhanu Jammalamadaka for his timely help. My research would not have been possible without their unselfish help.

CHAPTER 1

INTRODUCTION

1.1 Bone Implant Technology

Bone fractures are the most common injuries resulting from accidents, age, and bone-related diseases. As bone is a metabolically active tissue, it undergoes continuous interplay between the bone-resorbing osteoclast and the bone-forming osteoblast cells throughout life, enabling it to repair small defects [1]. However, bone tissue cannot repair large bone defects and severe fractures. The choice of treatment modality depends on the severity of the fracture. When a bone cannot regenerate itself, bone grafts are implanted. Bone grafting is defined as "a surgical procedure that places new bone or a replacement material into spaces between or around broken bone (fractures) or in holes in bone (defects) to aid in healing" [2]. Bone implants are also used to treat bone disorders such as osteomyelitis and osteosarcoma, where the infected parts of the bone are resected and filled with drug eluting bone implants.

Autograft, allograft, and synthetic materials are the three material choices used in modern grafting procedures. A graft made from a patient's own bone (usually hip bones or ribs) is called an autograft. To obtain a piece of bone for an autograft, the patient is subjected to surgery under general anesthesia, and the bone is removed, typically from the iliac crest. An incision is made, the bone is removed, and the wound site is closed. An

allograft uses bone taken from a cadaver or, less frequently a living donor, and frozen and stored [2, 3]. Chemical compounds, such as calcium phosphate (CP), PMMA and polyether ether ketone (PEEK) are used as synthetic materials to fill the fractured spaces [4].

An ideal bone graft should have the bioactive properties of osteogenesis (the formation of new bone), osteoinduction (the chemical process of inducing a conversion of patient's osteoprogenitor cells into osteoblasts), and osteoconduction (providing a scaffold for cells to form new bone) [3].

1.2 Need for Improved Implant Technology

A surgeon places the graft by making an incision in the skin over the bone defect and shapes the replacement material into the graft site. Pins, plates, or screws are used to position the graft, and the incision is stitched closed. The supply of allografts and xenografts is limited. These materials can be rejected by the host's immune system, can transmit diseases, and pose a high risk of contamination.

Currently available metallic implants have been used clinically for more than 40 years and have been medically efficacious. However, in spite of their success, they are subject to several drawbacks, such as excessive stiffness, accumulation of metal ions in the surrounding tissue, growth restriction, required removal/revision surgery, inability to carry drugs, and susceptibility to infection [5, 6, 7]. Moreover, additional revision surgery results in increased financial costs and prolonged recovery time for patients.

The search for an alternative to replace these metal implants has been largely focused on bioabsorbable materials. Many biopolymers such as poly-lactic acid and poly glycolic acid have showed multiple of uses in the implant technology. However, these

polymer's properties such as mechanical strength and time of degradation need to be customized according to the site of implantation [6]. Biopolymers when used as implants will not necessitate a secondary surgery and they can also be engineered to degrade at the rate of new tissue formation, transforming the load gradually from implant to the newly formed tissue. In addition, they are widely available in different forms (solids, gel, fibers) and can be easily molded into different shapes and compositions. Therefore, there is a need to replace the traditional metallic implants with biodegradable materials.

Contamination during the medical process can be caused by many factors, such as biomaterial chemistry of the implant material, their surface physical properties, design of the medical device, anatomical site of implantation, the extension of surgical invasion, and the time of application [8]. In orthopedic surgeries, use of biomaterials involves a high risk of developing infections [9]. Because bacteria can attach to these biomaterials and develop resistance by forming biofilms, treating these infections systemically is difficult and localized treatment was proven efficient [10]. High-infection rate also imposes a high financial cost [11]. It is therefore important to prevent infection during bone implantation.

In medical conditions such as osteomyelitis, where bone is infected by microorganisms, the infected parts of the bone are resected and filled with antibiotic eluting implants. Bone cements added with anti-infective agents molded in the shape of beads or pellets are commonly used for this purpose [12]. Similarly, in osteosarcoma, cancerous bone is resected and voids are filled with chemotherapeutic eluting implant materials [13]. Commercially available Poly Methyl Methacrylate (PMMA) bone cements have good mechanical properties, but they are not biodegradable. They cause

cytotoxicity to the surrounding tissues due to the methyl methacrylate monomer release. So replacement of the currently available bone implant material with biodegradable or bioresorbable implants would be beneficial.

Most bone cements currently used undergo a chemical reaction within the mixture and form micro pores of different sizes. These pores can act as a starting point of cracks and cause premature failure of the cement. To avoid this pore formation, cement can be mixed under vacuum conditions. Unfortunately, when cement is mixed under vacuum, it leads to reduction in volume during polymerization, causing high shrinkage and worse adhesion when compared to non-vacuum mixed cement [9].

Several approaches have been used to fabricate anti-infective bone cement. Different antimicrobial agents have been used, as well as different ways to bind these agents within the bone-cement matrix. Typically, drugs are dry mixed with the bone cement and administered into the body. However, the addition of antibiotics reduces mechanical properties in the bone cement. Furthermore, the release of the antibiotic is short-lived and results in less than maximal antibiotic release [14].

The use of nanoparticle technology as a drug delivery system is a well established strategy for enhancing the bioavailability, allowing targeted drug delivery and improved therapeutic efficacy. Currently, many nanoparticles are under investigation for treatment of diseases, more specifically for chemotherapeutic and antibiotic drug delivery. Due to unique features, such as large surface to mass ratio, ability to load a vast variety of compounds and biocompatibility, nanoparticles such as Carbon Nanotubes (CNT) and Halloysite Nanotubes (HNT) are widely used for medical purposes. Gomol *et al.* replaced micro-particles (usually barium sulfate or zirconium oxide) with nanoparticles on

commercially available PMMA bone cement and found a 41% increase in tensile strain-to-failure and a 70% increase in tensile work-of-fracture. They attributed the increase in mechanical properties to crack-tip blunting. It is phenomenon where a propagating crack is deflected or stopped when a solid particle obstructs its path [15].

Currently available metallic implants and therapeutic drugs are bulk manufactured and often do not meet the patient's requirements many times. A surgeon needs to modify them (cut, weld, trim, or drill holes for implants and change dosages for drugs) to suit the patient's specifications. Every individual has unique physiology and reacts differently to drugs and therapies. Generic medicines do not account for these individual differences. Personalized medicine can modify the methods of therapies and drug delivery to best suit the individual. This personalization may help reduce the failure of treatments and improve the functionality of the tissue. Major advances in biomedical engineering have led to new patient's specific technologies which treat diseases with controlled drug delivery and/or replace wounded tissue with biocompatible materials. The 3D printing using FDM is one of them. FDM printing's high speed, accuracy, affordability, and feasibility have led to its increased use in medicine and biotechnology. This technology is used in printing prosthesis, human tissues, medical devices, and surgical implants for dental and orthopedic applications.

1.3 Objectives

The objective of all three projects is to design customizable and biodegradable materials that are cytocompatible and can elute bioactive compounds such as antibiotics, chemotherapeutics and hormones. The following objectives will be the core focus of this research:

1. To formulate novel calcium phosphate cements (CPC) with enhanced mechanical properties and sustained anti-infective drug release profiles using doped HNTs.
2. To engineer novel methods for fabricating customized anti-infective and chemotherapeutic implant materials using biodegradable polymers.
3. To design bioactive polymers enhanced with hormones for personalized medicine and hormone replacement therapy.

1.3.1 CPCs Doped with HNTs

CPCs are well known for their osteoinductive and osteoconductive nature, but their usage is limited to non-load bearing regions because they have poor mechanical properties. Whereas commercially available PMMA bone cements have good mechanical strength, they are non-degradable and do not have osteoinductive properties. Moreover, their cytotoxicity, caused by the release of MMA monomer, and their excessive stiffness are undesirable qualities. A crucial need exists to increase the mechanical properties of CPCs. Novel calcium phosphate bone cements are formulated with various combinations of calcium phosphate salts mixing with different aqueous solutions. Natural polymers will be added to these combinations to achieve anti-washout properties and increase the mechanical strength. They will be allowed to set at ambient temperatures and checked for their anti-washout properties. HNTs will be used to increase the mechanical properties and also as a drug delivery system.

Change in mechanical properties will be evaluated by compression and flexural testing. Surface modifications due to the addition of HNTs will be studied using SEM. Antibiotic drugs will be loaded in HNTs using vacuum loading techniques and drug elution studies will be done to compare anti-infective compound release over time.

Cytocompatibility of these formulated cements will be checked by conducting XTT assay on osteoblast cells cultured along with the CPC scaffolds. Bacterial testing using *E. coli* will be performed to check the antibacterial activity.

1.3.2 3D Printing Antibiotic and Chemotherapeutic Constructs

The objective of this research is to develop a novel method of 3D printing customized implants using biodegradable materials doped with drugs such as antibiotics and chemotherapeutics. Filaments used in a 3D printer will be customized accordingly in order to achieve this objective. ExtrusionBot filament extruder will be used to extrude bioplastics doped with drugs. These customized extruded filaments will be used in MakerBot 3D printer for printing constructs. The goal will also focus on the capability to customize the 3D printing parameters in order to match the modified materials.

Thermoplastics are heated for extrusion and printing processes, thermal degradation of bioactive compounds doped in them may occur. So to test their activity bacterial cultures for antibiotic constructs and osteosarcoma cultures for chemotherapeutic constructs will be done. Images of the extruded filaments and printed constructs will be taken to study the surface morphology. Compression and flexural strengths of the constructs with and without drugs are compared in order to study the effect of drug doping on the mechanical properties.

In most of the bone diseases and disorders, the surgeon resects the infected bone and fills the resected area with drug eluting implants. Using patient's data such as X-ray or CT scan, defective parts can be processed, 3D printed, and used as implant material. To test the proof of principle, defects will be made on the cow femur bone and scanned

using a 3D scanner. These scanned files will be processed, imported as STLs and will be printed with the customized filaments.

1.3.3 3D Printing Hormones

The objective of this study is to 3D print customizable implant materials which can elute hormones for personalized medicine and targeted drug delivery. In this part of the research, hormones (female reproductive hormones) will be coated on to the biodegradable thermoplastic materials and filaments of the required dimensions will be extruded. These extruded filaments will be 3D printed and the scaffolds will undergo a series of tests. For surface morphology, SEM will be used; for drug elution profiles, spectroscopy will be used, and for testing the bioactivity of the scaffolds, cell culture using estrogen reporter stable cell line will be used.

1.4 Organization of Dissertation

This dissertation is comprised of six chapters. Chapter 1 is a brief introduction of bone implant technology and its problems, the need for improving the implant technology, and the objectives of this research. Chapter 2 is a detailed review of bone biology, bone diseases and their current treatment modalities. It also focuses on 3D printing technology and its applications in the medical field. Chapter 3 focuses on HNTs as a potential additive material for enhancing the mechanical properties of CPCs and also as drug delivery system. Chapter 4 covers the novel 3D printing techniques that involves manufacturing of customized biodegradable implants that can elute anti-infective and chemotherapeutic drugs and tests for their bioactivity. Chapter 5 investigates 3D printing of hormone eluting implantable materials and their tests for bioactivity. Chapter 6 draws conclusions and describes potential future work.

CHAPTER 2

BACKGROUND

2.1 Bone

The bone is a skeletal connective tissue which provides a structural framework for the body. It is a dynamic and highly vascularized tissue that undergoes remodeling, a process involving local resorption and formation of bone, throughout the lifetime of an individual [16]. It also serves as a mineral reservoir, protects internal organs, creates motion by opposing muscular contractions, and is a site of hematopoiesis. It is made up of both organic and inorganic matter. Bone, like most biological tissues, is hierarchically structured to provide the maximum strength with a minimum of material [17]. In order to expedite a full characterization of the bone, each separate constituent of the bone that contributes to the whole system must be evaluated.

2.1.1 Types of Bone

Based on the different proportions of osseous tissue, bone is classified into compact (cortical) and spongy (cancellous). Compact bone is dense, smooth, and homogeneous. It also stores calcium and has 70-80% of its matrix calcified [18]. Compact bone is composed of many cylindrical shaped units called osteons, or haversian canals. This type of bone is abundant in the diaphysis region of long bones and plays a mechanical and protective role [18, 19].

On the other hand, spongy bone does not contain osteons. It has needle-like bony structures with an irregular lattice of thin columns and plates called trabeculae [20]. This type of osseous tissue has low density and strength but has a high surface area and forms the inner cavity of the epiphyses called bone marrow [19, 21, 22]. Bone formation and deposition depend upon the mechanical stress applied to them [16, 22]. In a study conducted by Rubin and Lanyon, functionally isolated avian bone showed an increased bone deposition on an application of rigid-external load and a substantial remodeling on removal of it [23, 24].

2.1.2 Bone Cells

Osteogenic cells, osteoblasts, osteoclasts and osteocytes are the four different types of cells present in the bone. Osteogenic cells are stem cells that undergo mitosis and develop into osteoblasts. These are also called osteoprogenitor cells and are present on all non-resorptive bone surfaces. They form the deep innermost layers of the periosteum and endosteum.

Osteoblasts are single-nucleated, cuboidal shaped cells that secrete extracellular matrix. They also secrete many non-collagenous proteins, such as osteocalcin and osteopontin that initiate bone mineralization and maintain calcium homeostasis [25]. The lifespan of osteoblasts is about eight weeks in humans. These cells are anchorage-dependent and rely on extensive cell-matrix and cell-cell contacts to maintain its cellular functions. Some osteoblasts get trapped in their own calcified matrix and change their phenotype to develop into osteocytes [22].

Osteoclasts are macrophages and are derived from hematopoietic stem cells. These highly migratory, multinucleated and polarized cells carry lysosomal enzymes. The

most intriguing feature of osteoclasts is the presence of apical membrane which can form a tight seal with the calcified matrix. An activated osteoclast can resorb 20,000 μm^3 of bone minerals per day [22].

Osteocytes are smaller in size than osteoblasts, contain fewer organelles and have a high nucleus-to-cytoplasm ratio [22]. They have a high number of filopodia or cytoplasmic extensions interconnecting other osteocytes. These help in the exchange of nutrients and waste [18].

2.1.3 Extracellular Matrix (ECM)

Bone extracellular matrix consists of both organic and inorganic compounds. Organic matrix forms 30% of the complete bone. It contains proteoglycans, glycosaminoglycans, osteonectin (anchors bone minerals to collagen) and osteocalcin (a calcium binding protein). During the process of mineralization, glycoproteins, such as osteopontin and osteonectin are expressed more and hence serve as the markers for the matrix mineralization. Bone has collagen fibers dispersed all over the matrix, providing strength and resilience. The inorganic matrix is primarily composed of mineral salts with almost 70% being apatites of calcium and phosphate. This mineral crystal form, called hydroxyapatite, precipitates around collagen fibers of osteoids and makes the bone hard, resistant to crushing [19].

2.2 Osteosarcoma

Osteosarcomas are the most common primary malignancy of connective tissue, with approximately 900 cases reported every year in the United States [26]. The etiology of this disease remains unknown. Although, several risk factors such as age, gender, use of tobacco and alcohol increase the incidence of osteosarcoma. People with inherited

genetic conditions such as retinoblastoma, Li-Fraumeni syndrome, bloom and werner syndrome have an increased risk of developing this disease [26, 27]. The incidence of osteosarcoma has a bimodal age distribution, having the first peak during adolescence and the second peak in the seventh and eighth decade of life [27, 28].

The most common primary sites of osteosarcoma are usually the distal femur and the proximal tibia (around knee joints). Pain and swelling in the affected area are the common symptoms of this disease. Pain may become worse, especially during physical activity or at night. Several weeks after the pain starts, lumps may be formed at the affected site and bones become fragile and vulnerable to fractures. Accurate diagnosis is an essential prerequisite for treating the osteosarcoma. Imaging and histological confirmation are the two current techniques used for diagnosis. An MRI of the entire bone in which the primary tumor is located, is the first diagnosis test that an osteosarcoma patient receives. A Computer Tomography (CT) scan of the chest will be performed to detect any lung metastases. Bone scintigraphy using technetium (commonly called as bone scan) of the whole body is employed to check any distant spread of the disease and a biopsy of the tumor is done finally to characterize the type and stage of the tumor [26, 29, 30].

For a successful treatment of osteosarcoma, both surgery and chemotherapy are necessary. Chemotherapy is administered as neoadjuvant (preoperative) and adjuvant (post operative) therapies. Neoadjuvant therapy is used to measure the chemo-responsiveness of the tumor, attempt to shrink the tumor and avoid extensive surgical procedures. This therapy is administered for a period of 8-10 weeks before the surgery [31]. Following the surgery, adjuvant therapy is administered for 12-29 weeks [32]. High

doses of drugs methotrexate, doxorubicin, cisplatin and ifosfamide are used in both phases. Chemotherapy on its own cannot eradicate primary cancer. Therefore, surgical treatment is necessary. Amputational and limb-salvage surgeries are the two most common, currently performed surgical strategies for osteosarcoma. Due to the recent advances in imaging techniques and novel drug delivery systems, approximately 80% of osteosarcoma surgeries are performed by limb-salvage surgery [30]. Reconstructions in these surgeries are possible with orthopedic implants such as rods, plates, screws, bone cements, and other osteoarticular grafts. Amputational surgeries are conducted only in severe cases.

Recurrence rate for cancers are generally high. A total of 30-40% of patients suffer localized osteosarcoma recurrence [33]. For this reason, novel surgical implants with drug-eluting capabilities became the focus of several studies [34].

2.3 Osteomyelitis

Osteomyelitis is one of the devastating infectious disease of the bone, and it remains a challenge to the physicians in both diagnosis and treatment [35]. Bones can be infected in many ways; infection may spread to the bone from another part of the body through the blood stream, fracture and/or open wound can expose the bone, and peripheral vascular diseases or bacteremia can occur. Bones of the lower extremity (foot and ankle) tends to be more susceptible to infections due to thin soft tissue layers, boney prominences, and poor vascular supply. Certain chronic conditions such as diabetes, sickle cell anemia and hemodialysis increase the risk of osteomyelitis [36]. The annual incidence of osteomyelitis is about 54.6 per 100,000 individuals, as per the statistics

conducted in 2012 [37]. The risk of foot ulceration is high in diabetic patients, and these ulcerations are often complicated by osteomyelitis [38, 39, 40].

Bone infections begin with adhesion of bacteria (or any other infectious organism) to the bone matrix. The attached organism causes inflammatory responses leading to bone necrosis. In addition, inflammatory factors such as IL-1 and TNF trigger the osteoclast activity, causing demineralization of bone [41]. Osteomyelitis is classified as acute or chronic, based on the duration of infection. Acute myelitis occurs over a period of a few days to weeks and has symptoms of localized pain, edema and redness at the site of infection. Chronic myelitis is a prolonged recurrence of an acute case and is characterized by ischemia and bone necrosis [42]. Most of the osteomyelitis is polymicrobial in nature. Microbes such as *Staphylococcus aureus, Escherichia coli* and *Pseudomonas aeruginosa* are the most robust. *Staphylococcus aureus* is the most common causative microorganism for osteomyelitis [43].

The success of these microbes is due to their ability to form biofilms which inhibits wound healing process and increases the susceptibility of the host to osteomyelitis. In addition, these biofilms are tough and do not allow easy penetration of antibiotics into their matrix, making them more resistant to anti-infective agents [35]. Thus, a method is needed to treat the biofilms in the wound and on the surface of the surgical implants in order to prevent osteomyelitis.

Since osteomyelitis is a progressive destructive process, accurate and early detection is necessary. Physical examination of the wound and microbiology of the bone biopsy are the two modalities used in combination to diagnose osteomyelitis. Swelling, redness, drainage from the wound, and deep chronic pain are common symptoms of this

disease. Bone fragmentation and necrosis with purulent drainage are the strong indications of the bone infection. Imaging techniques such as x-ray and CT scans are used to know the extent of debridement within the body.

To treat osteomyelitis efficiently, both medical and surgical methods are used either individually or in combination, depending upon the severity of the infection. The choice of antibiotic therapy depends on microbiology of bone biopsy. If the microbiology cannot be determined, broad spectrum antibiotics are administered parenterally for 5-6 weeks and then a prolonged course of oral administration is suggested. When antibiotic therapy is not adequate and a considerable amount of necrotic tissue is present, a surgical intervention of the wound is necessary. A surgeon cuts open the wound and removes all the necrotic bone and infected soft tissue around it. Despite the use of surgical intervention and prolonged course of antibiotic therapy, chronic recurrence of osteomyelitis is about 30% within a year of primary treatment [44]. To avoid this recurrence, the surgeon fills the resected area with antibiotic loaded spacers that elute antibiotics for an extended period of time preventing the biofilm formation and thus avoiding chronic recurrence of osteomyelitis [45].

2.4 Osteoporosis

Osteoporosis is a systemic bone disorder represented as one of the major health problem in the medical field. It is a skeletal disease characterized by a decrease in bone mass and deterioration of osseous tissue resulting in increased risk of bone fractures [46]. It occurs in both middle aged males and females, but is most common in post-menopausal women [47]. Depending upon the etiology, this disorder is classified as primary and secondary osteoporosis. Primary osteoporosis, also known as senile

osteoporosis, is caused by aging and accelerates at menopause. Its etiology is not clearly understood. Secondary osteoporosis is caused by nutritional factors and medical conditions such as hypogonadism, endocrine or hematological disorders, and auto-immune diseases [48].

Currently, about 200 million people suffer with osteoporosis worldwide. Approximately one-third of the female population above 60 years of age are commonly affected [49]. Several clinical studies have demonstrated that primary cause of osteoporosis in post menopausal women is due to sex-hormone deficiency, particularly due to estrogen deficiency [50]. Estrogen deficiency leads to down regulation of pro-inflammatory cytokines synthesis leading to increased formation of pre-osteoclast cells. These pre-osteoclast cells resorb bone minerals into blood causing osteoporosis. Approximately 2% of bone loss per year occurs within the first couple of years after menopause, clearly increasing the risk for fracture [51].

Long term Hormone Replacement Therapy (HRT) is generally prescribed to treat osteoporosis in elderly women. Estrogens are a group of female sex hormones responsible for the development and maintenance of normal sexual characteristics and functions. The three main types of estrogens are estrone (E1), estradiol (E2) and estriol (E3). E2 is the major estrogen produced in the ovaries and, in small quantities, in the adrenal glands and fat cells. It is the most active and predominant form of all estrogens and is responsible for most of the estrogenic effects. E2 and E1 are interconvertible. E1 is less potent than E2 and is mostly produced by adipose cells. E3 is secreted during pregnancy by the placenta and is the least potent of all the hormones. Depending upon the

individual hormone levels, HRT is prescribed as either estradiol alone or in combination with other hormones such as E1, E3, and progesterone.

2.5 Calcium Phosphate Bone Cements

Brown and Chow were the first to propose the use of calcium phosphate cement in bone repair [52]. In 1920, Albee reported the first successful medical application of calcium phosphate bio-ceramics in humans [52]. These cements are easily moldable, set at physiological temperatures, and have HA as their end product. These properties make them advantageous over other cements in the market. In addition, HA (its end product) is easily resorbed by the osteoclast cells leading to new natural bone formation at the bone-implant interface. This process is called osteotransductivity [53].

All CPCs are formulated by mixing a solid and a liquid component. The solid component consists of two or more calcium phosphate salts. The liquids can be water, alginates, chitosan, or sodium phosphates. To obtain maximum biological use, these components are mixed in predetermined proportions to form HA. Resorbability of the CPCs completely depends on its end product [4]. The physicochemical reactions that occur during mixing are complex.

The solid phase usually consists of a basic and an acidic salt, which react together in an aqueous medium and precipitates HA as a final product. In **Eq. 1**, Tetra-calcium phosphate (TTCP, $Ca_4(PO_4)_2O$, basic salt) reacts with β-Tri-calcium phosphate (β-TCP, $Ca_3(PO_4)_2$, acidic salt) in the presence of water and precipitates HA ($Ca_{10}(PO_4)_6(OH)_2$), whereas in **Eq. 2**, TTCP reacts with Di-calcium phosphate dehydrate (DCPD, $CaHPO_4.2H_2O$), an acidic salt in an aqueous medium and precipitates HA [54].

$$Ca_4(PO_4)_2O+2Ca_3(PO_4)_2+H_2O \rightarrow Ca_{10}(PO_4)_6(OH)_2 \quad \textbf{Eq. 1}$$

$$2Ca_4(PO_4)_2O+2CaHPO_4.2H_2O \rightarrow Ca_{10}(PO_4)_6(OH)_2+4H_2O \quad \textbf{Eq. 2}$$

In this process, water is a dissolving agent and is not a reactant in the setting process. It allows dissolution of particles and precipitation of the products. Relatively low strength, high brittleness, inadequate adaptability in clinics, and a high possible rate of dissolution at the initial setting stages due to formation of unstable phases are common disadvantages of water when used as a setting liquid [55]. These properties of water limit its use in clinical applications. It cannot be used for treating defects with bleeding or with the continuous flow of tissue liquids, like saliva, nor can it be used where the bone defect is at mechanical load bearing site.

Adding water soluble biocompatible polymers in the calcium phosphate cement either in the liquid or solid form increased properties such as cohesion, toughness, biological response, and resorption of material [56]. If the cement does not set and disintegrates, it provokes an inflammatory response and may lead to cell apoptosis at the site of cement application [57].

The introduction of gelatin or chitosan as a mixing liquid can affect the kinetics of setting and hardening of CPCs [58]. Chitosan is a linear copolymer of N-acetyl D-glucosamine and of D-glucosamine [54]. An increase in flexural strength of CPC composite reported when 15-20 wt% chitosan was incorporated in it [54, 56]. No cytotoxicity was found in chitosan containing CPCs. In addition, a considerable increase in ALP activity was observed when mesenchymal stem cells were cultured on TTCP-DCPA composite [56]. These bioactive properties have led to an increased use of chitosan in CPC.

Cement setting time depends on factors such as solid-liquid composition, liquid-to-powder ratio, and particle size of the powder. Setting conditions also influence the mechanical properties of the cement [59].

2.6 Nanoparticle Technology

Pathogens, even a small fraction, can induce devastating effects on humans. Antibiotic usage is an effective treatment for infections. However, recurrence of the infection is commonly seen and it tends to develop into a chronic problem in no time. In order to guarantee sufficient protection against microbes, developing novel therapeutic approaches to treat infections is of utmost importance [60]. The use of nanoparticle technology as a drug delivery system is a well established strategy for enhancing the bioavailability, allowing targeted drug delivery and improved therapeutic efficacy. Currently, many nanoparticles are under investigation for the treatment of diseases, more specifically for chemotherapeutic and antibiotic drug delivery. Due to unique features, such as large surface to mass ratio, ability to load a vast variety of compounds and biocompatibility, nanoparticles such as Carbon Nanotubes (CNT) and Halloysite Nanotubes (HNT) are widely used for medical purposes.

CNTs are graphite sheets commonly found as single-wall nanotubes (SWNTs) and multi-wall nanotubes (MWNTs). Due to their good mechanical, electrical, and electrochemical properties, they are widely used as biosensors [61]. Though CNTs are potential carriers for drug delivery, they cause toxicity due to the presence of ferric impurities, degree of functionalization, physical form, and agglomeration state [62]. Research conducted by Yang *et al.* on mice showed adverse effects due to accumulation of CNTs in major organs, such as the liver, spleen and lungs [62, 63]. Due to their high

cost, reduced availability and toxic effects, CNTs are less likely to be used than other nanotubes.

HNTs are commercially inexpensive, bi-layered aluminosilicate nanotubes found naturally as raw mineral deposit. These are commercially made by dehydrating 15-20 clay layers, which rolls up to form a hollow tubule capable of carrying drugs. The inside of the lumen is positively charged, and the external surface is negatively charged, permitting additional functional modifications of these surfaces. This charge on both outer and inner surfaces affects the efficiency of loading the drugs and other chemical agents. Substances with overall negative charge can be easily loaded into the lumen when compared to positively charged particles. The size of HNTs varies from 500-1000 nm with an inner diameter of 15-100 nm depending on the deposit [64].

Due to physical properties such as nanosized lumens, high L/D (length to diameter) ratio, low hydroxyl group density, low cost and abundant natural deposits, HNTs are studied as sustained drug releasing agents. They also reported improved mechanical performances and stability when used in the fabrication of polymer nanocomposites [65]. Loading HNTs with pharmaceuticals showed low initial release concentrations, preventing an initial outburst and uniform drug delivery (particularly with drugs, such as antibiotics, chemotherapeutics, hormones and other growth factors). The drugs gentamicin sulfate, nitrofurantoin, dexamethasone, furosemide and nifedipine gave an extended 6-10 hr release profile [66]. Under optimal conditions, a maximum loading of 12% volume (very close to theoretical capacity) was obtained [66]. When HNTs are added without an active agent, they act as skin-cleansing agents due to adsorptive

properties. HNTs adsorb dead skin cells and unpleasant oils from the skin, resulting in a fresh and healthy look [67].

2.7 Additive Manufacturing

3D printing is a process of making three-dimensional objects from a digital file. It can be achieved by either subtractive or additive manufacturing. In subtractive manufacturing, an object is created by removing sections from a block of material by cutting or drilling away the excess material. This type of prototyping is limited by cutting and routing technology, cannot create hollow parts from a single block of material, and generates excess material waste [68]. In additive manufacturing, the product is created by adding materials layer by layer until the final product is obtained. As shown in **Figure 2-1**, the desired construct is built by assembling many thin cross sectional layers, offering the ability to build complex and intricate designs [69]. Since the object is made in layers, a slicing software is required to slice the object's digital file into multiple layers. Each layer can be then analyzed separately and the set of instructions given to the machine can be customized as necessary. Depending on the form of material used, this process is categorized into solid based, liquid based, and powder based manufacturing. Presently, selective laser sintering (SLS), stereolithography (SLA), fuse deposition modeling (FDM), and laminated object manufacturing (LOM) are the widely used additive manufacturing techniques.

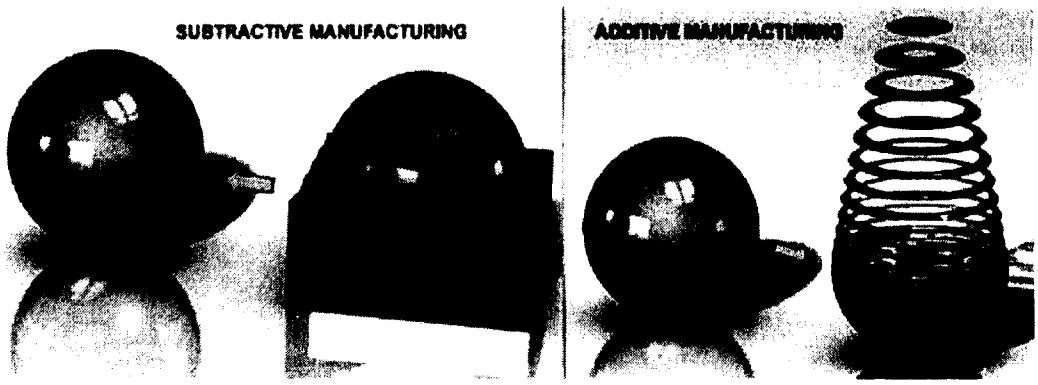

Figure 2-1: Types of rapid prototyping [69].

SLS uses high power laser beam to selectively fuse powdered materials (plastic, metal, ceramic or glass powders) into a desired 3D object [70]. Here, the laser beam act as a heat source to sinter the powders in pre-determined size and shape. After the first layer is selectively sintered, rollers deposit the second layer of loose powder from the feed bins, as shown in **Figure 2-2**, and the process is repeated from bottom to top until the desired object is formed.

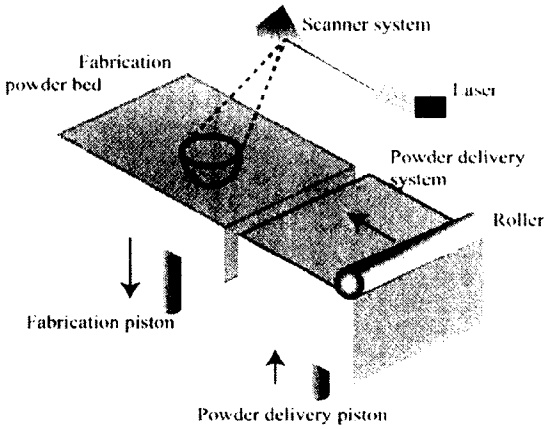

Figure 2-2: Selective Laser Sintering (SLS).

The performance of SLS process depends on laser power, thickness of the powder layer, roller speed and print bed's heating/cooling rate [71]. A wide range of materials

can be used for this process and the unused powder can be recycled. In order to avoid oxidation and to maintain the process at a constant melting point temperature, an inert gas atmosphere must be maintained [72].

SLA is a liquid based additive manufacturing process which uses precise and sufficiently powered UV laser beam to solidify photo-reactive polymer resin. Laser beam illuminates the surface of the resin in the shape of the desired object, as shown in **Figure 2-3**, resulting in solidification of polymer and adhering to the platform. Once the first layer is solidified, the support platform descends, allowing the liquid resin of calculated thickness to flow over the built layer and the process is repeated until desired artifact is built [73]. Excess liquid resin is drained or re-used. For better mechanical properties, finished objects are often exposed to the UV light, a process called post resin-curing. This process is limited only to photosensitive polymers such as low-molecular weight poly acrylate and epoxy macromeres.

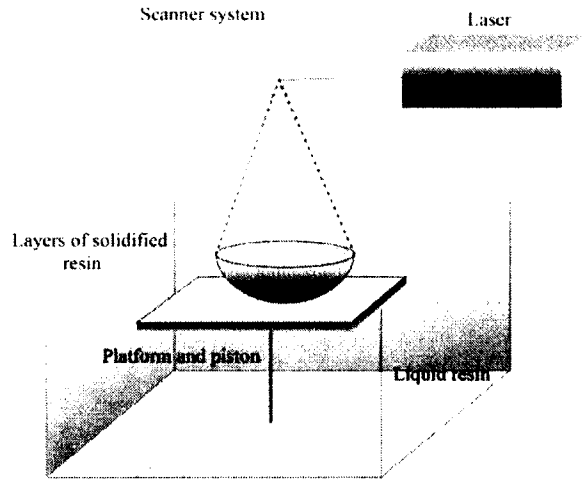

Figure 2-3: Stereolithography (SLA).

FDM is a solid based additive manufacturing technique. It builds 3D objects by depositing thin layers of thermoplastic filament on to a platform in layer-by-layer fashion

as shown in **Figure 2-4**. Plastic filaments including Acrylonitrile butadiene styrene (ABS), Polylactic acid (PLA), Polyamide (Nylon), Polyethylene terephthalate (PET), and Thermoplastic polyurethane (TPU) are commonly used for FDM. This method does not need any chemical post processing or resin-curing. Due to their cost effectiveness and wide range of material use, this type of prototyping is advantageous over others and is widely used. In this current study, 3D printer based on FDM principles are used.

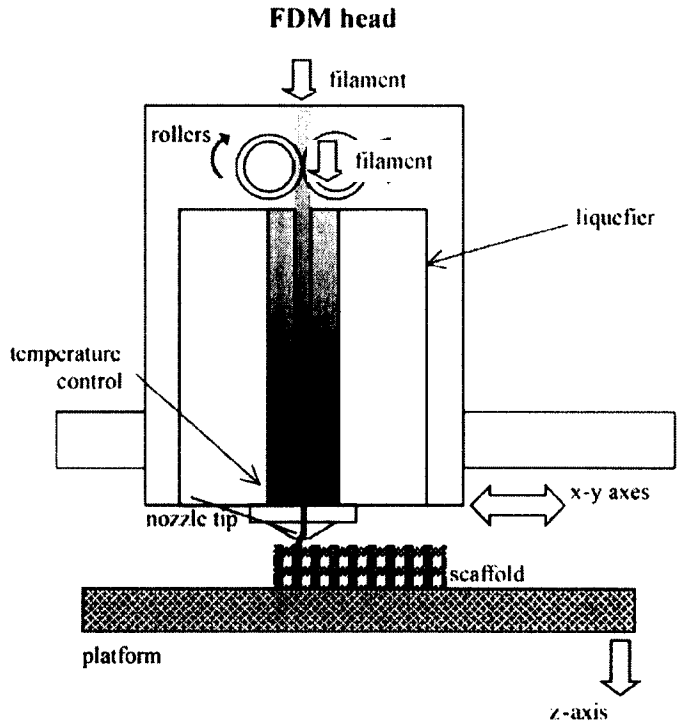

Figure 2-4: Fused Deposition Modeling (FDM) [74].

In LOM, layers of adhesive-coated material is glued together and cut into the required shape using a laser beam to obtain a 3D object. Materials used in this process include glued paper, plastic and metal sheets. A heated roller runs through a thin layer of adhesive material to make sure it adheres to the substrate properly as shown in **Figure 2-5**. A laser cutter traces through the sheet into the desired shape and then another layer

of the material is rolled over it. This process is repeated until the final artifact is built. Since the objects printed have wood like characteristics, this process is used to make relatively large subjects and additional drilling and machining of the parts are required. As paper and glue are used in this process, external factors like temperature and humidity affect the structure and composition of the part.

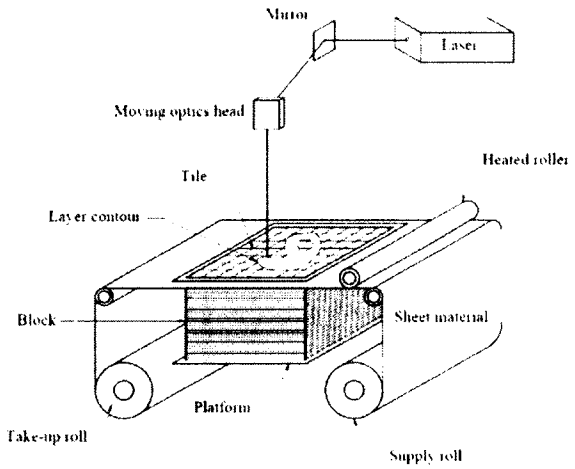

Figure 2-5: Laminated Object Manufacturing [75].

2.8 Fused Deposition Modeling (FDM)

FDM is an additive manufacturing technology developed by Scott Crump in the late 1980s. Later in1990, Stratasys Inc. patented and commercialized it as a technology [76]. In this process, a plastic filament is melted through a nozzle tip of the required diameter and laid on a platform in layer-by-layer fashion to build a three dimensional construct of the required shape as shown in **Figure 2-4** [74]. Plastic filaments including Acrylonitrile butadiene styrene (ABS), Polylactic acid (PLA), Polyamide (Nylon), Polyethylene terephthalate (PET), and Thermoplastic polyurethane (TPU) are commonly

used for FDM. A computer aided design (CAD) model is used to guide the nozzle tip accordingly to lay the material in the required shape.

For a 3D CAD model to be printed as 3D object, it has to go through the following steps as shown in **Figure 2-6**.

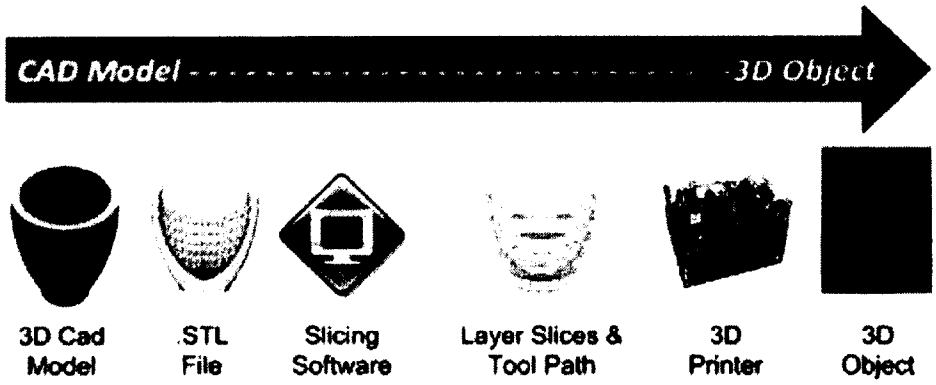

Figure 2-6: Steps involved in making a 3D object from a CAD model.

2.8.1 Stereolithography Files (STL)

STL also has several backronyms such as "Standard Tessellation Language" and "Standard Triangle Language". In order to interact with FDM machines, data files are saved as STL file format. It is a triangulated representation of a 3D CAD model. This format approximates the surface of an object with many triangles. For a simple object like a cube as shown in **Figure 2-7**, its surface is approximated with 12 triangles. As the complexity of the object increases, more number of triangles are used to estimate the surface.

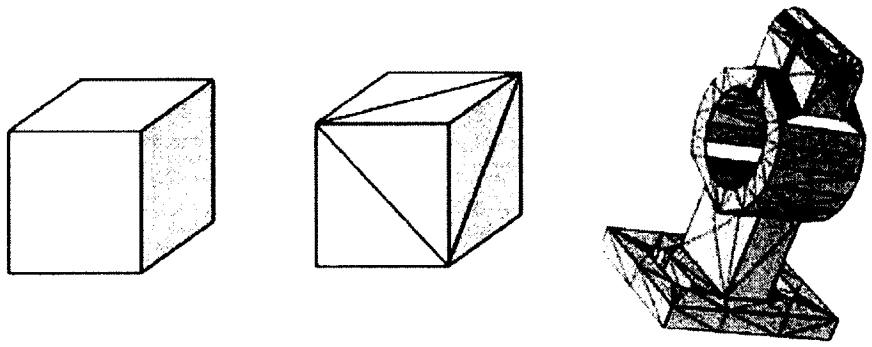

Figure 2-7: A) 3D model of a cube, B) STL format of a cube, C) STL file of a complex design.

Most of the CAD software currently available are capable of producing an STL file. AutoDesk, Solidworks, IronCAD are some of the widely used CAD software for making an STL model.

2.8.2 Computer Aided Design (CAD)

CAD is a program which helps users to create STL files. It helps in designing, analyzing and optimizing 3D models. This software helps in designing ideas and visualizing the concepts through photorealistic renderings. They also simulate the performance of the design in the real world. Solidworks 2015 and AutoCAD are the two softwares used in this research to design constructs of required shape and dimensions.

2.8.3 Slicer

Slicer is a software which cuts a CAD model into many horizontal slices (layers). It generates tool path by converting the design data into movement of the filament deposition head of the 3D printer along the X, Y, and Z axis over the build area. Printing parameters such as deposition head speed, rate of material flow from the head, and cooling fan speed can be modified according using this software. In the current research, slic3R and ReplicatorG were used for slicing the designed constructs.

2.9 Applications of 3D Printing in Implant Technology

High degree of freedom to produce custom medical devices is the greatest advantage of a 3D printer in the biomedical field [77]. This technology has been applied in the medical field since the early 2000, when custom dental implants and prostheses were first 3D printed and implanted surgically [78]. In 2011 Kaiba Gionfriddo, a six months old boy form Ohio, stopped breathing and turned blue. He was diagnosed with a rare condition called tracheobronchomalacia in which periodical collapse of the windpipe due to weakening of tracheal cartilage was observed, preventing him from normal breathing. Dr. Glenn Green, an associate professor of pediatric otolaryngology and his colleague Dr. Scott Hollister, professor of biomedical engineering and associate professor of surgery at the University of Michigan, were able to 3D print a custom tracheal-splint implant from CT scan data of the patient's trachea. These splints were made on a laser-based 3D printer using biodegradable polymer and was surgically implanted into the patient. The splint printed had a slit along its length in order to expand as the child grows. The baby recovered and within three years a full resorption of the implant occurred. Before this procedure, newborn babies with tracheobronchomalacia had no cure and little chance of survival. Now this procedure was patented and successfully replicated with three other babies having similar conditions [79].

Since Kaiba's story, 3D printing for biomedical applications has been gaining more importance. Customization of implants and surgical tools can have a positive impact on the success of the surgery, time required for surgery, and patient recovery time [80]. Another benefit of this technology is the ability to build the objects at low cost on a

small-scale production. The following are some of the applications of 3D printing in biomedical engineering.

2.9.1 Bioprinting Tissues and Organs

Allotransplantation from either a deceased or living donor is the current treatment for organ or tissue failure. There is always shortage of human organs available for transplant. Additionally, finding tissue which matches the host body is a difficult task. For the organ donor shortage, tissue engineering and regenerative medicine are considered as potential solutions. In tissue engineering, pluripotent cells are isolated, multiplied by adding external growth factors, seeded onto scaffolds, inducing cell differentiation and developing into a required functioning tissue [81]. 3D bioprinting offers additional advantages to this method by highly customizing the parameters such as precise placement of cells, cell concentration, drop volume and diameter of printed cells [82]. In this technology, print head is filled with living cells and are deposited onto the substrate to reproduce tissue or organ. To fabricate a heterogeneous tissue or organ, multiple print heads each filled with different types of cell lines can be used. Researchers at Cornell University used this technique to fabricate a living aortic valve that have similar anatomical features as that of the native valve. They used multiple print heads filled with smooth muscle cells and valve-interstitial cells suspended in an alginate-hydrogel system. They could successfully fabricate living heart valve conduits with a strong resemblance to the original value [83].

Similarly, many researchers have provided proof of concept to build bone, cartilage, spinal discs, artificial ear, and other types of tissues using bioprinting. However, if the bioprinted tissue has a thickness greater than 200 μm, the oxygen

diffusion between the host and transplanted tissue will be limited. In order to avoid this, organs with precise vascular network should be bioprinted, which has not yet been done [78].

2.9.2 Customized Implants and Prostheses

Traditionally, a surgeon had to modify standard implants according to the patient's anatomy by cutting pieces of metal/plastic to a desired shape, size and fit. Currently, CAD programs can convert digital files such as x-ray, MRI or CT scan into STL files and can be easily printed used a 3D printer. Due to this ability, 3D printing technology has been used in the health care sector to print complex, customizable prostheses and implants. For the first time technicians at the Biomedical Research Institute of Hasselt University in Belgium, 3D printed a titanium mandibular prosthesis and successfully implanted it to an 83-year-old woman [84]. This implant was made by fusing layers of titanium powder using a high power laser beam. In 2013, FDA approval for 3D printing polyetherketoneketone (PEKK) was received by Oxford Performance Materials and a skull implant was successfully printed and implanted in the same year [84].

The ear canal is structured differently in every individual and use of 3D printing allows making customizable ear prosthesis efficiently and cost-effectively. Using biomaterials such as silicon, silver nanoparticles and chondrocytes suspended in collagen, a prosthetic ear which can detect electromagnetic frequencies and anatomically similar to a human ear has been 3D printed successfully [85]. Use of 3D printing in orthodontics made the dental procedures cheaper and more efficient. To make dentures, crowns and bridges, all that is needed is a 3D digital scanner and a 3D printer. This process skips the

step of casting physical molds of patient's oral cavity and makes the surgical procedures less invasive and more accurate.

2.9.3 Anatomical Models and Tools for Surgical Preparations

Gaining insight into a patient's anatomy prior to a surgical procedure is of utmost importance for a successful surgery. Current imaging procedures such as MRI, CT scans and x-rays, which are viewed in 2D, are the only source to study and simulate surgery. Cadavers are also used for this purpose, but they lack appropriate pathology and provide more of an anatomy lesson than a representation of surgical procedure [77, 85]. Using 3D printer tangible models with exact patient specific anatomy can be printed. In Kobe University Hospital, Japan, surgeons started using 3D printed replica's of patient's liver to determine how to best carve a donor liver with minimal tissue loss, preserving its function and to best fit it in the abdominal cavity. In complex cases, like in neurosurgery, where a small error can even lead to potentially devastating consequences, 3D models with exact anatomy of the patient will help a lot in studying the case thoroughly and simulate surgery prior to operating on the patient. Clear or partially transparent materials with water content and texture similar to human tissues such as acrylic resins or polyvinyl alcohol were used to maximize the simulation conditions [78].

2.10 Biopolymers

Polymers were first synthesized from glycolic acid in the 1920s. At that time, polymer degradation was viewed negatively since they have a tendency to deteriorate eventually and are not suitable for long-term industrial uses [6]. However, this instability has proven to be greatly important in the medical field in the last four decades. In the late 1960s, the application of biodegradable implants using PLA biopolymer was introduced

by Kulkarni *et al.* [5]. Later in 1984, Rokkanento first used this material as the internal fixation device for treating fractured ankles [86]. Since then, many polymers such as poly lactic acid (PLA), polyglycolic acid (PGA), polyethylene glycol (PEG), poly (glycolide-co-lactide) (PLGA), and other lactic/glycolic copolymers have been used for medical purposes. An ideal bioimplantable polymer must be easily sterilizable, does not evoke any inflammatory reaction, and should be metabolized in the body completely without leaving any traces [6].

Traditionally used metal implants have been clinically efficacious, but they are excessively stiff, stay at the site of implantation permanently, need secondary revisions, and require surgical removal upon healing [5]. Biopolymer implants do not need additional or revision surgery, available in different forms and can be customized into different shapes and and compositions.

2.10.1 Types of Biopolymers

Biopolymers and bioplastics are often confused for one another. Polymers that are obtained from renewable sources are biopolymers and synthetic materials manufactured from biopolymers are called as bioplastic. Based on their origin, biodegradable polymers are classified as natural and synthetic polymers.

2.10.1.1 *Natural Biodegradable Polymers*

Collagen and chitosan are the two major natural biodegradable polymers available abundantly and widely used. In addition to those, fibrin, gelatin, chitin, silk and starch are the other natural polymers been under research interest currently. Collagen is a high molecular weight polymer (M_w=300 KDa) with a long helical shaped structure (length = 300 nm). It is enzymatically degraded by collagenase enzyme in the body. The rate of

degradation can be customized by altering the cross-linkings in the polymer chain. Its osteoinductive, osteoconductive, and osteogenic properties have led to a wide use in bone implant technology. Because a large portion of human bone minerals consists of HA and collagen, collagen is coupled with other biomaterials such as calcium phosphates to obtain a complete biomimetic system for osseous replacement [87].

Chitosan is a linear polysaccharide made of glucosamine and *N*-acetyl glucosamine. Depending on the processing method and its source, it has a molecular weight ranging from 250 to 1000 KDa. Chitosanase degrades this polymer *in vitro*. *In vivo* degradation is regulated by hydrolysis of acetylated residues in the presence of enzyme lysozyme. The biodegradation of chitosan depends on its molecular weight and degree of polymer crystallinity [88, 89]. Its good mechanical properties and osteoconductivity have led to increased use in calcium phosphate cements for orthopedic surgery. Researchers have shown that the scaffolds made of calcium phosphate cements mixed with nano-crystalline chitosan have 20-fold greater surface area and roughness when compared with calcium phosphate cements alone [90].

2.10.1.2 *Synthetic Biodegradable Polymers*

Among synthetic biodegradable polymers, Poly (α-hydroxy acid) class polymers are most extensively investigated and widely used. PLA, PGA and PLGA are few of the biopolymers of this class used extensively for medical purposes. Their biodegradable and biocompatible nature account for their wide use in implant technology. These polymers undergo *in vivo* degradation through de-esterification process mediated by hydrolysis and the monomer end products are removed through excretory pathways [91, 92]. Several factors including crystallinity, chemical structure and composition, physical dimensions

of implant, surface area and site of implantation affect the rate of polymer biodegradation.

PLA is an aliphatic thermoplastic polyester which melts around 175°C and has a glass transition temperature of 60-65°C. It is formed by the polymerization of cyclic diester of lactic acid (lactide). Lactide exists in two optical isomer forms, D and L-lactide. PLA made from L-lactide are more crystalline in nature and biodegrade at a low pace when compared to PLA made out of D-lactide. Due to this reason L-PLA is used more in orthopedic surgeries. Wide use of this polymer, than any others, is due to its excellent mechanical and thermal properties added with biocompatible and biodegradable nature. PLA in the body is hydrolyzed into lactic acid, which enters into citric acid cycle and subsequently excreted as carbon dioxide from the lungs [93]. Research conducted by Brady *et al.* showed an absorption rate of about 1.5 years for 50-90 mg of radiolabeled PLA implanted in a rat's abdominal wall [94]. In another research, L-PLA bone implants attached to a sheep femora showed small traces of the polymer still after 4 years of implantation [95]. However, in both cases, PLA is well tolerated by the surrounding tissue and most of the polymer is primarily metabolized through respiration.

PCL is a semi-crystalline aliphatic polyester, melts at 65°C and has a glass transition temperature of -60°C. It is formed by the ring opening polymerization process of ε-caprolactone. In the body, PCL degrades in two phases. It first undergoes hydrolysis of esters bonds and form fragments of caprolactone oligomers. These oligomers are then engulfed by macrophages and they undergo degradation inside phagosomes by lysozyme enzymes [95]. Since this polymer exhibits low mechanical strength, its use in implant technology is limited to non-load bearing regions only.

CHAPTER 3

NANO-ENHANCED CALCIUM PHOSPHATE BONE CEMENTS

Currently available PMMA bone cements cause tissue damage around the bone/cement interface due to the release of toxic methylmethacrylate (MMA) monomers [96, 97]. These cements exhibit a high exothermic setting temperature ranging from 70°C to120°C [98]. In an experiment conducted by Stancyk and Rietbergen, on bovine cancellous bone, the temperature exposure of 70°C by a fraction (10%) of the bone at bone/cement interface was recorded [99]. In addition, PMMA cements lack elasticity and have dense structure which does not allow bone growth inside the cement.

CPCs, on the other hand, are osteoconductive and osteogenetic [57]. They set endothermically at body temperature. They have even shown an x-ray diffraction spectra similar to the mineral phase of the bone [4]. In addition low shrinkage, durability, density or porosity (depending on site of injury), and formability (ability to fill cavities of complex configurations) are positive qualities of CPCs [55].

Risk of contamination is common in all implantable biomaterials used. The objective of the present study is to increase the mechanical properties of the CPCs along with inculcating anti-infective properties to it. HNTs were used to enhance mechanical properties and to introduce anti-infective nature to the CPCs. The basic foundation for this work was a part of a group project with Uday Jammalamadaka. Data obtained from mechanical testing and SEM were shared with Uday Jammalamadaka.

3.1 Materials and Methods

Different compositions of calcium phosphate salts were mixed, and formulated CPCs were tested for their compression strengths. Formulation with highest compression strength was selected and further used. HNTs were loaded with antibiotics: Gentamicin Sulfate (GS) and Neomycin sulfate (NS). Surface morphology was studied using SEM imaging. For evaluating mechanical properties, compression testing and flexural testing were conducted. *Escherichia coli* and *Pseudomonas aeruginosa* were used to evaluate the anti-infective properties of the HNT loaded CPCs.

3.1.1 Materials

Calcium phosphate dibasic anhydrous ($HCaO_4P$, DCPA, Catalog no. 21177), β-tri calcium phosphate ($Ca_3O_8P_2$, β-TCP, Catalog no. 16483), calcium phosphate monobasic monohydrate ($H_4CaO_8P_2.H_20$, MCPM, Catalog no. 21053), chitosan oligosaccharide lactate (Catalog no. 523682), chitosan (low molecular weight, Catalog no. 448869), polycaprolactone ($C_6H_{10}O_2$, PCL, Catalog no. 440744), calcium L-lactate ($C_6H_{10}CaO_6.xH_20$, Catalog no. L4388), HNTs (Catalog no. 685445) were from Sigma-Aldrich, St. Louis, MO. Tetra calcium phosphate (Ca_4O_4P, TTCP, Catalog no. 010813A) was ordered from CaP Biomaterials, E. Troy, WI. Cupric chloride ($CuCl_2$, Catalog no. SA09487M) and calcium carbonate ($CaCO_3$, Catalog no. SA09409M) were delivered from Nasco, Fort Atkinson, WI. Sodium phosphate dibasic (Na_2HPO_4, Catalog no. 7782856) was from Fisher Scientific Company, Waltham, MA.

3.1.2 Formulation of CPCs

Different types of calcium phosphate salts were mixed in different proportions using various liquid phases and were labeled as shown in **Table 3-1**.

All samples were hand mixed, using mortar and pestle, under ambient conditions (room temperature and atmospheric pressure). The powder phase was mixed thoroughly until all of the salts were uniformly dispersed. To this phase, the liquid phase was added in small quantities and triturated until the mixture became a thick, moldable paste. This paste was molded into compression cylinders of 6 mm in diameter and 12 mm in length in accordance with ASTM F451-99a [100]. These samples were left to set for 24hours, then removed from the molds.

The compression testing was performed using ADMET expert 2600 universal testing machine with an axial cross-head speed of 1 mm/min [54]. To minimize the error, five samples for each formulation were tested and an average was calculated. The formulation with the best compressive strength was chosen and used for further testing.

Table 3-1: Formulation number, composition of calcium phosphate salts and the type of setting liquid used.

Formulation number	Solid phase (weight in gm)	Liquid phase (volume in ml)
1	MCPM (2)	Na_2HPO_4 (1)
2	DCPA (2)	Na_2HPO_4 (1)
3	MCPM (1) + DCPA (1)	Na_2HPO_4 (1.8)
4	$CaCO_3$ (1.5) + MCPM (0.5)	Na_2HPO_4 (1.5)
5	MCPM (1) + DCPA (1) + HNTs (7%)	Na_2HPO_4 (0.6)
6	MCPM (1) + DCPA (1) + HNTs (5%)	Na_2HPO_4 (0.6)
7	DCPA (2) + PCL (5%)	Na_2HPO_4 (0.6)
8	MCPM (0.4) + DCPA (0.4) + β-TCP (0.1) + Chitosan (0.1)	Na_2HPO_4 (1.6)
9	MCPM (0.4) + DCPA (0.4) + β-TCP (0.1) +	Na_2HPO_4 (1.6)
10	MCPM (0.45) + DCPA (0.45) + β-TCP (0.1)	Na_2HPO_4 (0.9)
11	MCPM (0.45) + DCPA (0.45) + β-TCP (0.05) + HNTs (0.05)	Na_2HPO_4 (0.9)
12	MCPM (0.75) + DCPA (0.75) + $CaCO_3$ (0.5)	Na_2HPO_4 (0.9)
13	MCPM (0.45) + DCPA (0.45) + $CaCO_3$ (0.5) + Chitosan (0.5)	Na_2HPO_4 (1.2)
14	MCPM (0.47) + DCPA (0.48) + $CaCO_3$ (0.5)	Na_2HPO_4 (1.2)
15	MCPM (0.5) + DCPA (0.5)	Na_2HPO_4 (0.4)
16	MCPM (0.5) + DCPA (0.5)	Na_2HPO_4 (0.4) + PCL (0.4)
17	MCPM (0.4) + DCPA (0.4) + PDDA (0.2)	1% Chitosan (1.2)
18	MCPM (0.4) + DCPA (0.4) + Alginate (0.2)	5% Chitosan Lactate (1.2)
19	TTCP (1.5) + DCPA (0.5)	5% Chitosan lactate (1.4)
20	MCPM (0.4) + DCPA (0.4) + β-TCP (0.1) + PDDA (0.1)	10% Chitosan lactate (1.4)
21	TTCP (1.5) + DCPA (0.5)	10% Chitosan lactate (1.2)
22	TTCP (1.4) + DCPA (0.4) + β-TCP (0.2)	10% Chitosan lactate (1.2)

Molds of inner dimensions 65 mm × 10 mm × 4 mm were prepared using paraffin wax in accordance with the ASTM F417-78 standards [101]. Using the same machine, flexural strength, using three-point bending test, was conducted at a cross-head speed of 0.75 mm/min with 20 mm distance between two consecutive points. Three samples for each concentration of HNTs were used and an average was calculated.

Flexural strengths of CPCs were calculated using the formula in **Eq. 3** and the peak force values obtained from the three-point bending test:

$$\sigma = \frac{3FL}{2bd^2}, \qquad \textbf{Eq. 3}$$

where σ is the flexural strength; F is the peak force; L is the distance between extreme points; b is the sample's width; d is the sample's height.

For cell-culture techniques, specimens 5 mm × 1 mm were made using steel molds. The liquid phase used in this process was prepared from sterile deionized water. After setting, the samples were removed from the molds, dipped in alcohol and dried under a class II hood. Samples of size 5 mm X 1 mm were cast in steel molds, then alcohol treated and dried for use in bacterial culture studies.

3.1.3 Loading HNTs

A 500 mg of Gentamicin Sulfate (GS) (Catalog no. G3632, Sigma, MO, US) was dissolved in 10 ml of deionized water, then sonicated until the drug was completely dissolved and a clear solution was formed. To this solution, 1 gm of HNT powder was added and sonicated for 30 minutes. This solution was then kept under the vacuum for 20 minutes, then kept at room atmosphere for 20 minutes. This process of alternate vacuum and room atmosphere was repeated three times. It was then washed with water to remove the drug on the surface of the HNTs and dried under open air, until it took a powder form.

The same procedure was followed for loading Neomycin Sulfate (NS) (Catalog no. 21810031, Gibco, NY, US).

3.1.4 Mechanical Properties

Different concentrations of HNTs were added to the strongest formulation and tested for both compression and flexural strengths. Data from these samples were compared. **Figure 3-1** shows the ADMET expert 2600 universal testing machine used to test the mechanical properties of the CPC scaffolds.

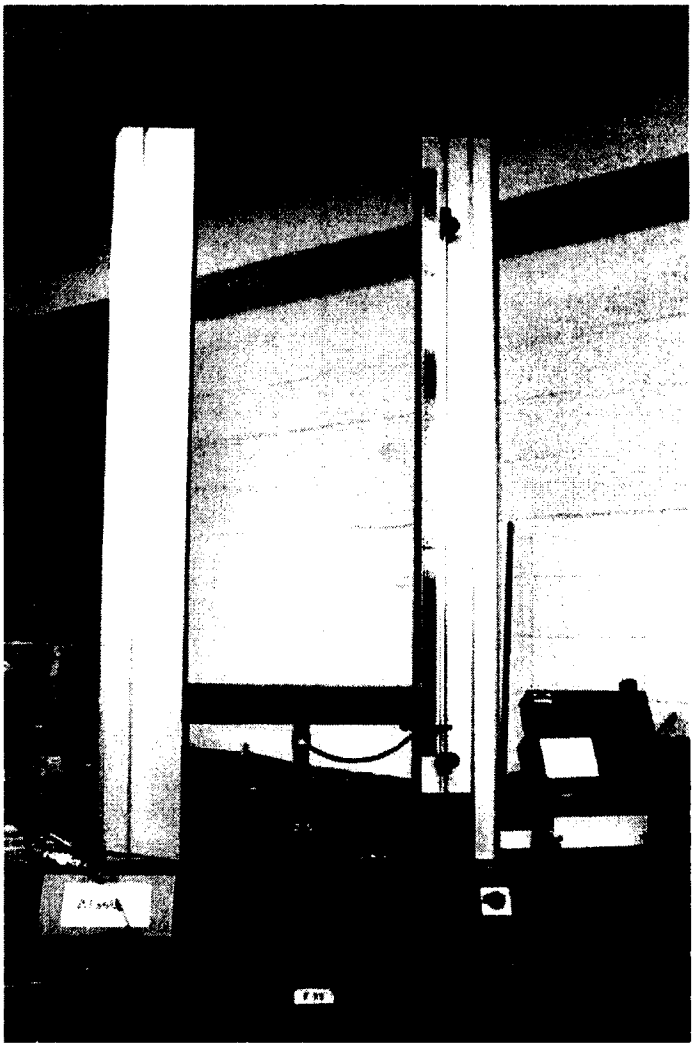

Figure 3-1: Admet 2600 Dual Column Bench Top Universal Testing Machine.

3.1.5 Scanning Electron Microscopy (SEM)

To observe the surface properties of the CPC samples, a scanning electron microscope was used. Images were taken of the fracture interface of the cement samples using a S4800 Field Emission SEM, HITACHI Scanning Electron Microscope. A 3 nm layer of gold was coated on to the surface of the scaffolds prior to imaging to make the samples conductive. Images were taken for samples with and without HNTs, and also for different concentrations of HNTs in CPC scaffolds.

3.1.6 XTT Assay

XTT or (2,3-Bis-(2-Methoxy-4-Nitro-5-Sulfophenyl)-2H-Tetrazolium-5-Carboxanilide) is a sensitive and reliable quantitative assay. It is a colorless or slightly yellow color tetrazolium dye which gets converted into bright orange color formazan upon reduction. When this dye is used in cell cultures, the dehydrogenase enzymes produced from the mitochondrial cycle of actively respiring cells reduces the dye to an orange color formazan. This assay is greatly improved by adding an electron accepting agents such as PMS (N-methyl dibenzopyrazine methyl sulfate). Unlike MTT, this assay does not require to go through laborious procedures such as solubilization prior to quantization, making this process quick and easy.

To check the cytocompatibility of the formulated scaffolds, XTT was performed on Human Osteoblast Cells (HOB) C-12760 purchased from PromoCell, Heidelberg, Germany. XTT assay kit (X4751) with 1% PMS was ordered from Sigma-Aldrich. CPC discs of 5 mm × 1 mm dimensions were molded using different concentrations of HNTs

(5%, 10% and 15%). Control discs without any HNTs and blank cell lines were also cultured for comparative studies.

Osteoblast cells, upon reaching to 90% confluency, were trypsinized and re-suspended into culture media. In a 96 well plate, 100 µl of cell suspension was added in each well and incubated for 24 hours. Activated XTT solution (20 µl) was then added to each well and incubated for 2 hours and optical densities were measured using Phenix LT-4000 absorbance microplate reader at 450 nm.

3.1.7 Drug Release Profile

A total of 50 mg of loaded HNTs (GS and NS separately) were transferred to 1.5 ml eppendorf tubes. Simulated body fluid (SBF, 1 ml) was added and placed on a rocker for continuous movement of the liquid. Samples were collected at 5, 10, 15, 20, and 30 minutes, as well as 1, 2, 4, 6, 12, and 24 hours for the first day and then one sample a day for 7 days. To avoid HNTs in the collected samples, eppendorf tubes were centrifuged for 2 minutes at 5000 rpm. The same amount of fresh SBF was replaced into the tubes each time the sample was removed and was vortexed until the sediment of HNTs was redispersed. The same procedure was followed for sampling the CPC scaffolds. Discs of 10 mm × 2 mm were used for the drug release profiles.

As GS cannot be detected directly by UV-Visible spectroscopy, an indirect method of detection by ophthalaldehyde reagent was used. This reagent was prepared by adding 250 mg of ophthalaldehyde powder (Sigma, MO, US) to 6.25 ml of 95% methanol. This mixture was sonicated for 30 minutes until a clear solution was obtained. 0.3 ml of 2- hydroxy ethyl mercaptan (Catalog no. M6250, Sigma, MO, US) was added to 56 ml of 0.04 M sodium borate (Catalog no. B9876, Sigma, MO, US) and mixed

thoroughly [102]. Both of these mixtures were added, then sonicated for 15 minutes before being stored in an amber color container for 24 hours. A total of 1 ml each of the collected gentamicin sample, isopropanol (to prevent sedimentation) and ophthalaldehyde reagent, were mixed and left undisturbed for 20 minutes at room temperature [103]. The absorbance for the GS was measured at 333 nm using a Thermo Scientific NanoDrop 2000c spectrophotometer.

Spectrophotometric determination of NS was performed using copper chloride. This reagent was prepared by dissolving 12.5 mg copper chloride (sigma, MO, US) in 25 ml of a water-ethanol (4:1) mixture, then sonicating until a clear solution was formed [104]. Collected sample (1 ml) was diluted with deionized water to 10 ml. To this sample, 2 ml of copper chloride solution was mixed and absorbance values were measured at 277 nm [104].

3.1.8 Bacterial Cultures

Bacterial strain *Escherichia coli* and *Pseudomonas aeruginosa* were used in this study. Both were clinical grade strains kindly provided by Dr. Giorno, Department of Biological Sciences, Louisiana Tech University, LA. A single colony from each plate was picked using a sterile toothpick and was inoculated separately into 3 ml of liquid broth (LB) medium. These cultures were incubated at 37°C for 24 hours with gentle rocking. From this medium, 50 µl was pipetted into LB-agar plates and spread using sterile glass beads. Discs of 5 mm × 2 mm with different concentrations of HNTs loaded with the drug were placed on the plates, then incubated at 37°C for 24 hours in an incubator. Inhibition zones were determined by measuring the diameter of the inhibited area at three different points and averaged. The measured zones included the sample at

the center. Three agar plates were tested for each sample. The principle objective of this study was to determine the effectiveness of antibiotics in HNTs incorporated into CPCs by means of measuring the release profiles and determining the zone of inhibition.

3.2 Results and Discussion

3.2.1 Mechanical Properties

3.2.1.1 *Compression Strength*

All formulations were subjected to compression testing. Five samples were tested for each formulation and the average was taken. **Table 3-2** shows the compression strengths of all compositions. Most of the samples washed off when they were immersed in water for a day. Specimens 1, 2, 3, 4, and 7 were brittle and were broken before they could be removed from the molds. Sample 11 was strong enough and showed great mechanical properties, but it was washed out in a day when immersed in water for testing the cohesive property (anti-washout property). None of the samples which used sodium phosphate as a setting liquid could give a good anti-washout property. When 5% w/v chitosan lactate was used, the samples were hard, flexible and cohesive (Sample 18). Chitosan lactate, 10% w/v, was already a thick viscous liquid and hence higher concentrations of it was not attempted.

Table 3-2: Table showing the values of peak load and compression pressure for each specimen.

Formulation No.	Peak Load (Kg)	Compression Pressure (Mpa)
1	0	0
2	0	0
3	0	0
4	0	0
5	78.84	11.72
6	107.93	11.82
7	0	0
8	18.57	2.78
9	40.41	6.32
10	38.07	4.90
11	81.97	14.18
12	1.79	0.23
13	17.28	2.25
14	22.45	3.10
15	29.51	3.81
16	33.00	9.85
17	76.00	8.32
18	32.5	3.61
19	70.00	7.86
20	58.27	6.65
21	119.00	15.10
22	72.00	8.11

Sample 21 gave the largest compression strength. This composition, TTCP (1.46 gm) and DCPA (0.54 gm) mixed in 10% w/v chitosan lactate, showed a cohesive nature and remained solid without disintegrating for several days when suspended in water. This formulation was used for all further experiments.

When HNTs were added to this formulation, an increase in compressive strength was recorded. This strengthening may be caused by crack-tip blunting [15], a process where a propagating crack is either deflected, cracked or stopped because of solid particle obstruction. Different concentrations of HNTs in this formulation were subjected to compression testing, and the composition with 5% wt of HNTs showed the highest compression resistance than the others. **Figure 3-2** shows the stress-strain curves of individual CPC scaffolds with different concentrations of HNTs and **Figure 3-3** shows the compression strengths of CPCs with different HNT concentrations.

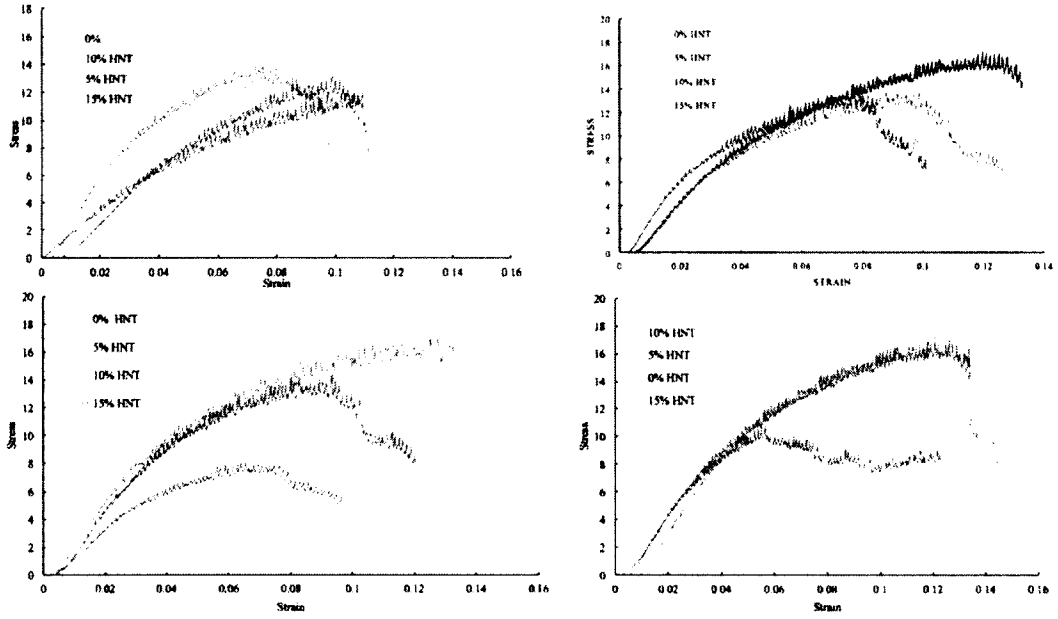

Figure 3-2: Stress-Strain curves for different trails of CPC constructs.

The compressive stress-strain curves for all the constructs had increasing strain until breakage of the sample. With the increasing stress, all the scaffolds showed initial fast increase followed by a slow decrease in strain. For all the control CPC constructs, the increasing strain curve was much smaller than HNT loaded CPCs. The stress-strain curve for 5% wt HNT CPC scaffolds had elongated, increasing the strain followed by a slow decrease. Upon further addition of HNTs, the stress-strain curves showed a similar trend as that of the control CPCs. This indicates that the compression strengths of the CPCs were increased upon the addition of 5% wt HNTs.

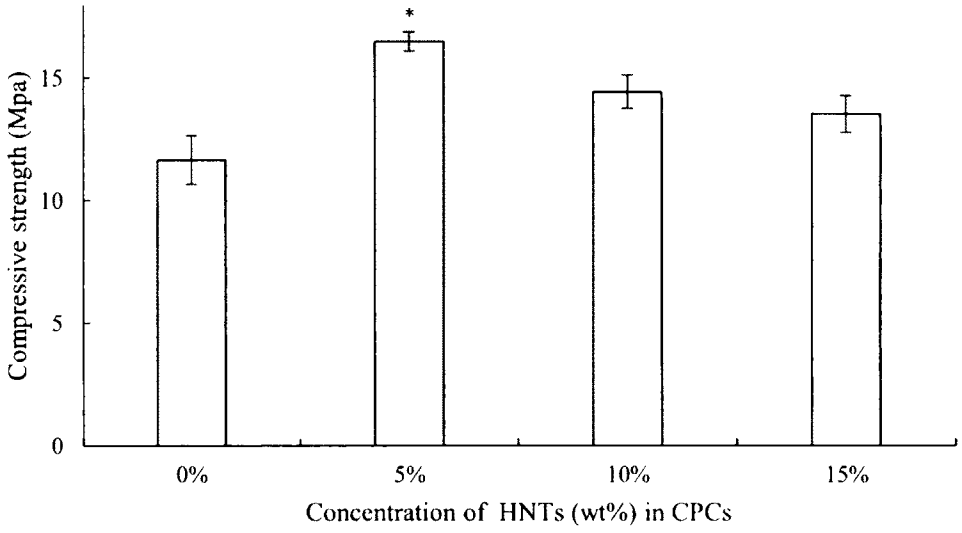

Figure 3-3: Compressive strengths of CPC samples with different concentrations of HNTs (mean ± SD, n = 5). Statistical significant differences are marked with * for $p < 0.05$ [105, 106].

A one-way ANOVA was conducted on these samples and a significant difference in the mean values among groups was seen. Using Tukey's post hoc analysis, the highest average among the groups were identified as 5% wt HNT. Control CPC scaffolds had 11.65 ± 2.24 MPa compressive strength, whereas CPCs with 5% wt HNTs had 16.5 ±

0.95 MPa of compressive strength. A 41% increase in strength upon the addition of 5% wt HNTs were observed.

Upon further increasing the concentration of HNTs, compressive strength decreased. Samples with 10% and 15% wt HNTs had 14.43 ± 1.64 MPa and 13.54 ± 1.67 MPa of compressive strength, respectively. Compressive strength of both 10% and 15% wt HNT scaffolds was smaller than that of the 5% wt HNT scaffolds but higher than that of the controls. The reduced strength may be due to uneven distribution of HNT particles or may be due to hindering the HA formation around their surfaces.

3.2.1.2 *Flexural Strength*

Figure 3-4 shows the flexural strength values of CPCs scaffolds with and without HNTs added to them. The Control group (0% HNT) showed a strength of 13.9 ± 2.5 MPa, whereas 5% wt HNT samples had 17.1 ± 2.5 MPa of flexural strength. Three samples for each batch were subjected to flexural testing. One-way ANOVA was conducted on these samples at 0.05 significance level. No significant difference among the mean values was observed. However, mean values of the groups showed a 23.51% increase in flexural strength of the samples upon addition of 5% wt HNTs to the CPC samples. Similar to the compression strength values, further addition of HNTs decreased the flexural strength of the samples.

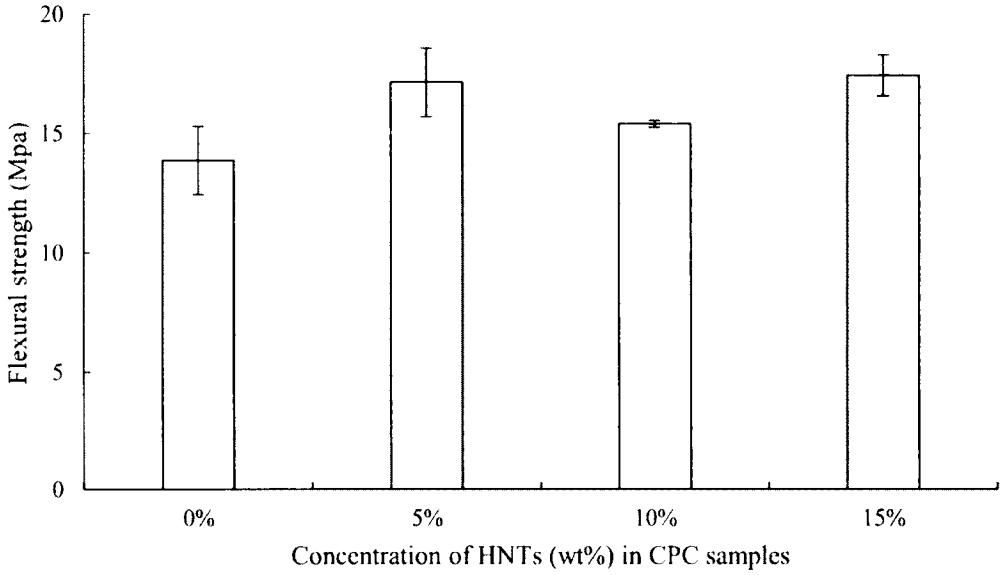

Figure 3-4: Flexural strengths of CPC samples with different concentration of HNTs (mean ± SD, n = 3). Statistical significant differences are marked with * for $p < 0.05$ [105, 106].

3.2.2 Morphology of CPC Scaffolds

The SEM images in **Figure 3-5** show the surface morphology of CPCs with and without HNTs. These scaffolds showed compact polygonal shaped microstructures of varied sizes ranging from 5 μm to 15 μm. These highly aggregated microstructures had clearly visible interconnecting micropores. All cement formulations had rough surfaces. These rough surfaces may improve cell attachment and viability, making the scaffolds good substrates for cell conduction. Additionally, these micropores promote propagation of cells within the scaffold.

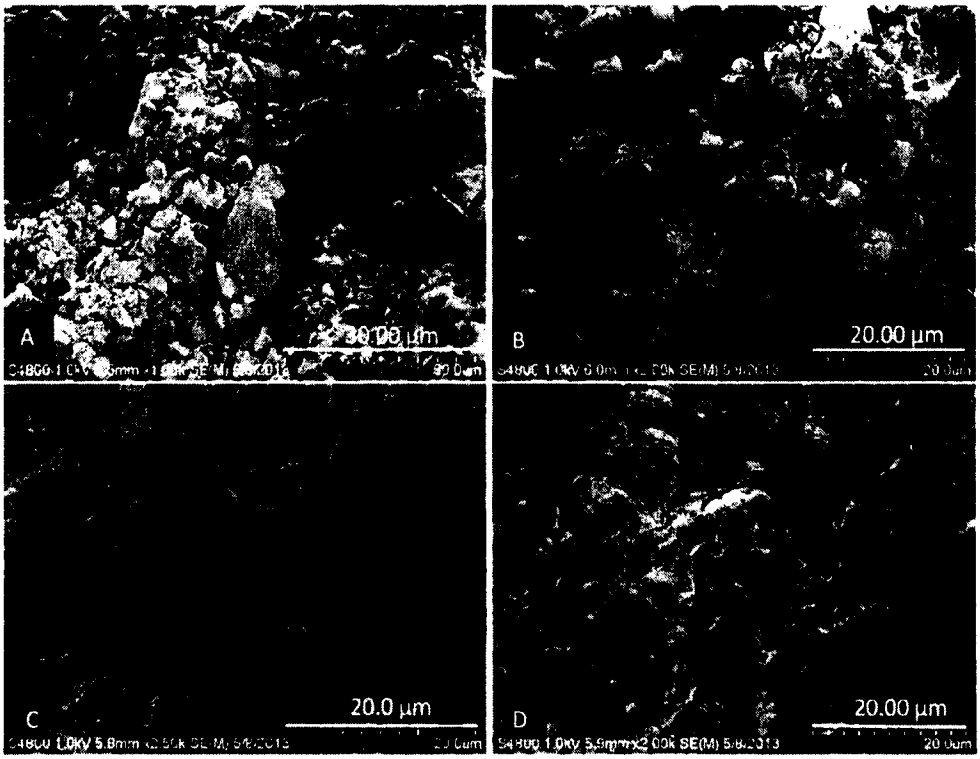

Figure 3-5: SEM of CPC scaffolds with different concentrations of HNTs. A) 0%, B) 5%, C) 10%, and D) 15% [105].

Upon further magnification, traces of HNTs were found on the surface of the scaffolds. **Figure 3-6** shows the cluster of HNTs on the CPC surface.

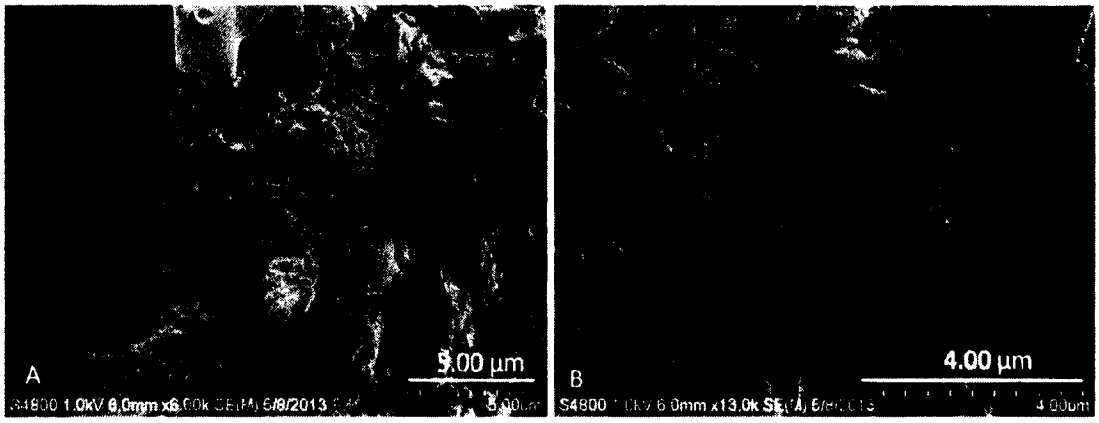

Figure 3-6: SEM showing cluster of HNTs on the surface of the CPC-HNT (5% wt) scaffolds. Image B was also used in Uday Jammalamadaka's dissertation [106].

3.2.3 XTT Assay

The viability of human osteoblast cells on the surface of the CPC scaffolds was analyzed at days 3, 7 and 14 (**Figure 3-7**). Higher absorbance values indicate greater cell viability. Six wells of each batch were tested and one-way ANOVA was conducted to analyze the significant changes among the groups. The mean values of absorbance varied strongly with HNT concentration. On day 3, a 20.35% increase in absorbance values was observed for control CPC scaffolds when compared to wells containing only cells. On addition of 5% HNTs to the CPC scaffolds, a 28.3% significant increase in absorbance value was noticed. For 10% and 15% HNTs, absorbance was 9.8% and 12.8% larger, respectively. However, when compared with control CPC scaffold (no HNTs added), 8.7% and 6.1% decrease in absorbance values for 10% and 15% CPC-HNT scaffolds were seen.

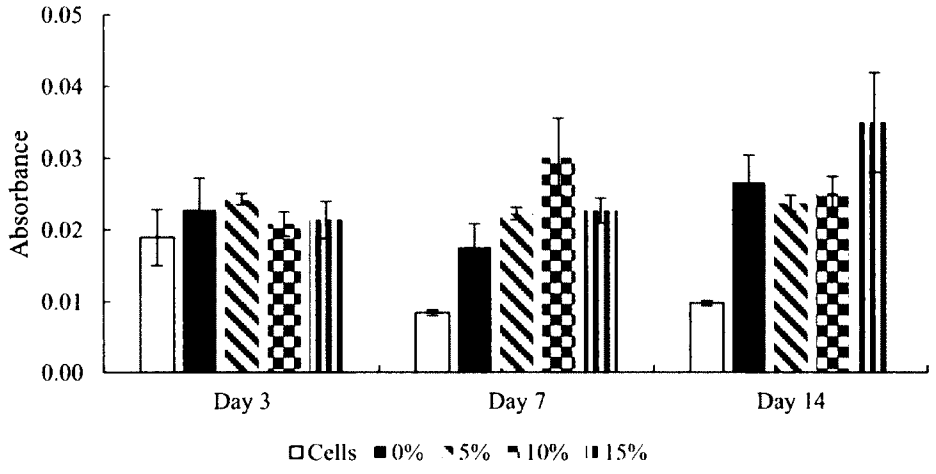

Figure 3-7: Cell viability assessed in human osteoblast culture on different CPC-HNT scaffolds (mean ± SD, n = 6). Statistical significant differences are marked with * for $p < 0.05$.

On day 7, absorbance was larger for CPC scaffolds than for control wells. Wells containing 5% HNT samples showed 26.7% larger absorbance compared to CPC samples without HNTs. CPCs with 10% HNTs had the highest absorbance value.

On day 14, all wells containing CPC scaffolds showed higher absorbance values than the control wells and it was largest in scaffolds with 15% HNTs.

The absorbance values of the XTT assay reflects the mitochondrial activity of the live cells. The results suggest that CPC scaffolds do not cause cyto-compatibility issues instead, they enhance the viability of the osteoblast cells. In addition, further increase in viability was seen upon addition of HNTs to the cement samples.

3.2.4 Drug Release Profile

An elution study was performed to estimate the amount of drugs released over one week. A NanoDrop 2000c Spectrophotometer was used to measure GS absorbance at 333 nm and NS at 277 nm. From the standard-graph curve, an equation was derived and was used to back calculate the amount of drugs released. **Figure A-1** in the Appendix section shows the standard graph and linear equation used to back calculate the unknown samples concentration.

Figure 3-8 and **Figure 3-9** shows the cumulative concentrations of GS and NS released from HNTs and CPC-HNT scaffolds. Both scaffolds exhibit a burst release of drugs for the first 24 hours, followed by an extended and sustained release.

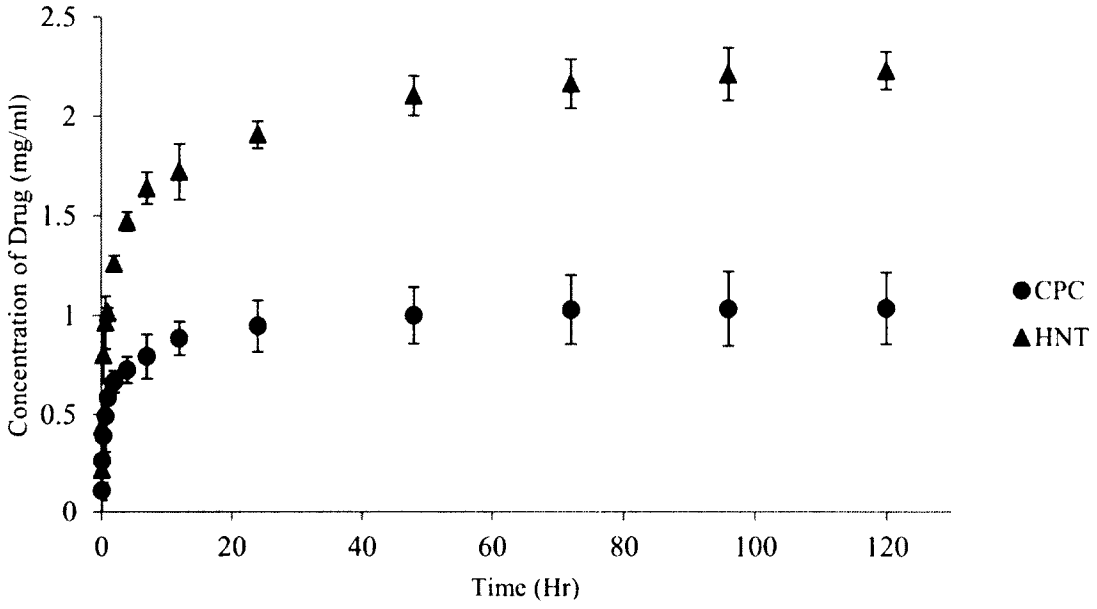

Figure 3-8: Cumulative concentration of GS released from HNTs and CPC-HNT scaffolds (mean ± SD, n = 3) [105].

Within 24 hours, 1.9 mg/ml of drug was released from HNTs and 0.9 mg/ml from the CPC scaffolds. This initial outburst may be caused by release of drug from the surface of the HNTs. Only a small amount was released thereafter, but it was steady and extended. Once the release amount reached 0.94 mg/ml by 48 hours, the release rate decreased. Scaffolds could only release 0.05 mg/ ml from 48-120 hours, which was within the working concentration (4 μg/ml) of the drug.

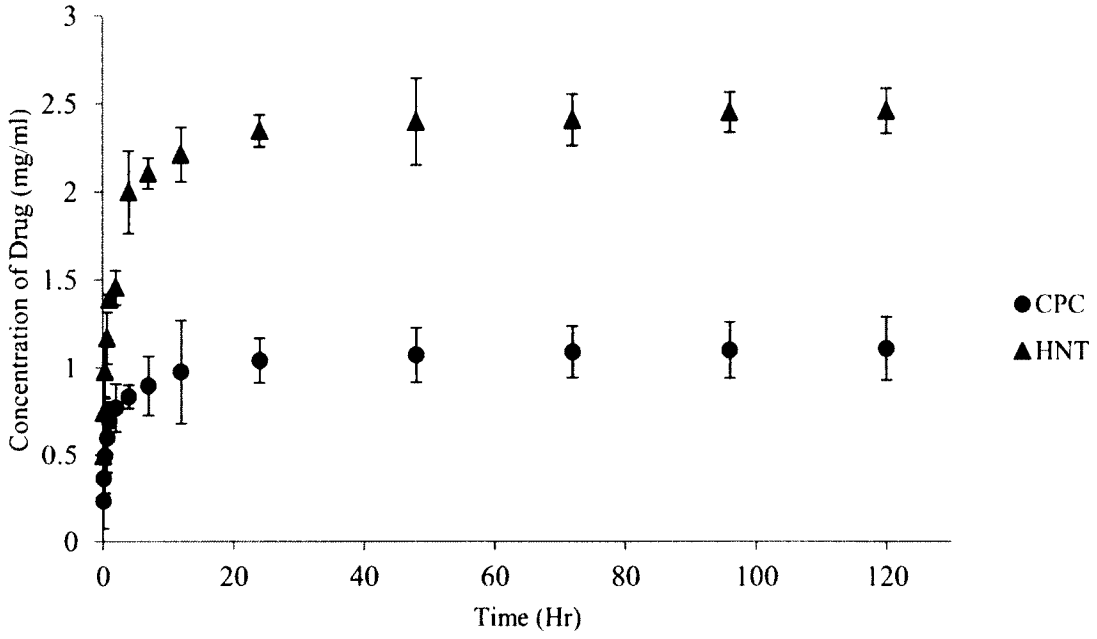

Figure 3-9: Cumulative concentration of NS released from HNTs and CPC-HNT scaffolds (mean ± SD, n = 3) [105].

The NS showed 1.04 mg/ml of drug release from CPC scaffolds within 24 hours, whereas HNTs alone showed 2.39 mg/ml release. A cumulative concentration of 1.12 mg/ml was released from scaffolds for a total of 120 hours. In all the samples, even after 120 hours of release, NS released from the constructs did not drop below the minimum inhibitory concentration (16 μg/ml). The graph in **Figure A-2** of the Appendix shows the standard curve and linear equation used to calculate the NS concentrations from the unknown samples.

The two graphs show that after 24 hours of release, elution decreased steadily. This decrease might be because the anti-infective agent inside the HNTs present on the surface of the scaffolds would have already emptied, and those HNTs entrapped inside the scaffold matrix might have not been exposed to sampling liquid. The antibiotic release might have continued if the scaffolds were left to degrade.

3.2.5 Bacterial Culture

Images in **Figure 3-10** shows the inhibition zones for *E. coli* and *P. aeruginosa* incubated with CPC scaffolds loaded with different concentrations of HNT-GS. Control samples (0% HNT) exhibited no inhibition zones. Images in **Figure 3-10** (A-B) shows the inhibition diameters for *E.coli* and (C-D) for *P. aeruginosa*. Clearly delineated inhibition zones were seen in all the CPC-HNT-GS scaffolds. With the increase in concentration of HNTs, inhibition diameter also increased.

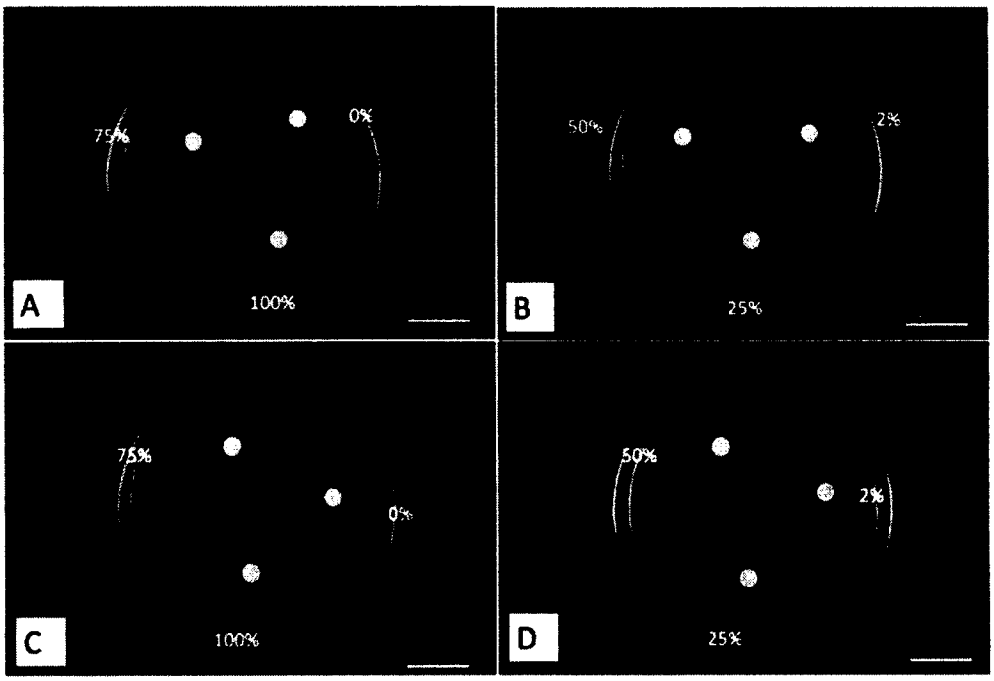

Figure 3-10: Inhibition zones of CPCs loaded with different concentrations of HNT-GS against *E. coli* (A-B) *P. aeruginosa* (C-D).

Images in **Figure 3-11** shows the inhibition zones of CPC scaffolds loaded with different concentrations of HNT-NS. Control sample (0% HNT) had no inhibition zones. Images in **Figure 3-11** (A-B) shows the inhibition diameters for *E.coli* and (C-D) for *P. aeruginosa*. Similar to HNT-GS, clear delineating inhibition zones were seen in all the

CPC-HNT-NS scaffolds. Inhibition diameter also increased with the increase in HNT concentration.

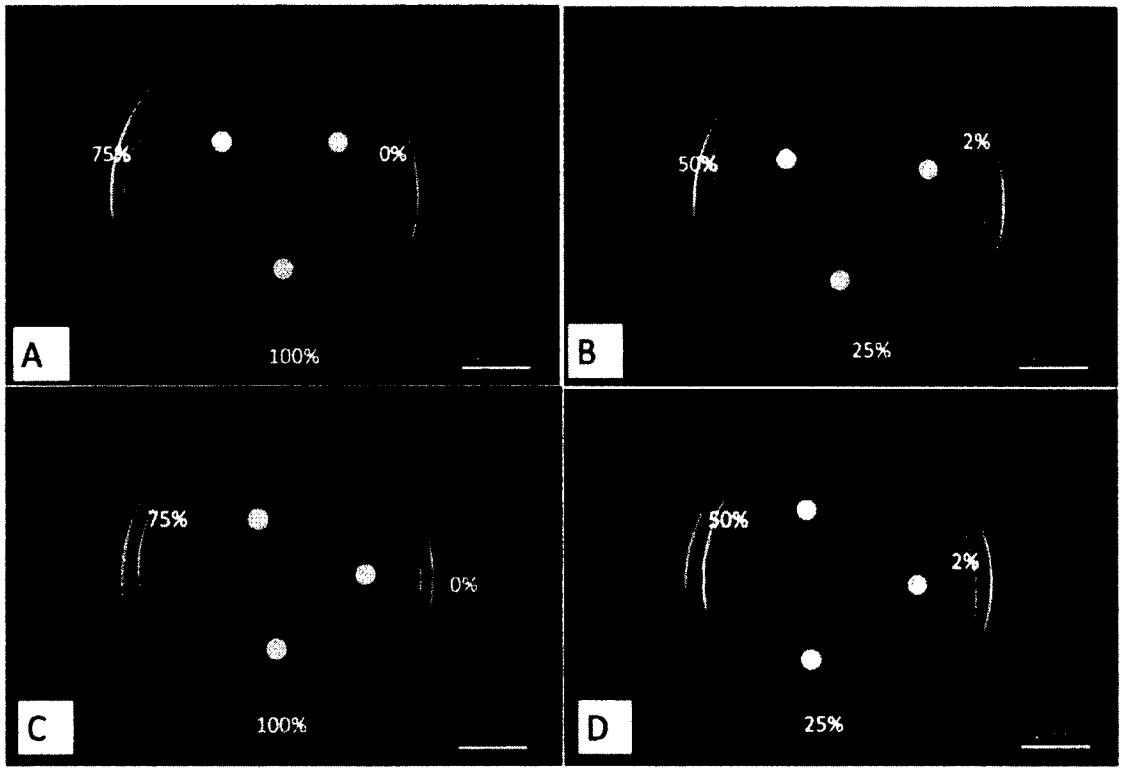

Figure 3-11: Inhibition zones of CPCs loaded with different concentrations of HNT-NS against *E. coli* (A-B) and *P. aeruginosa* (C-D).

All these experiments were conducted in multiples of three and one-way ANOVA was conducted at the significance level of 0.05. Inhibition diameters were significantly different among the groups containing different concentrations of HNT's. **Figure 3-12** shows the Inhibition values of different concentrations of CPC-HNT-GS against *E.coli* and *P. aeruginosa*. With the increase in HNT-GS concentration, zone of inhibition diameters also increased for both *E.coli* and *P. aeruginosa*.

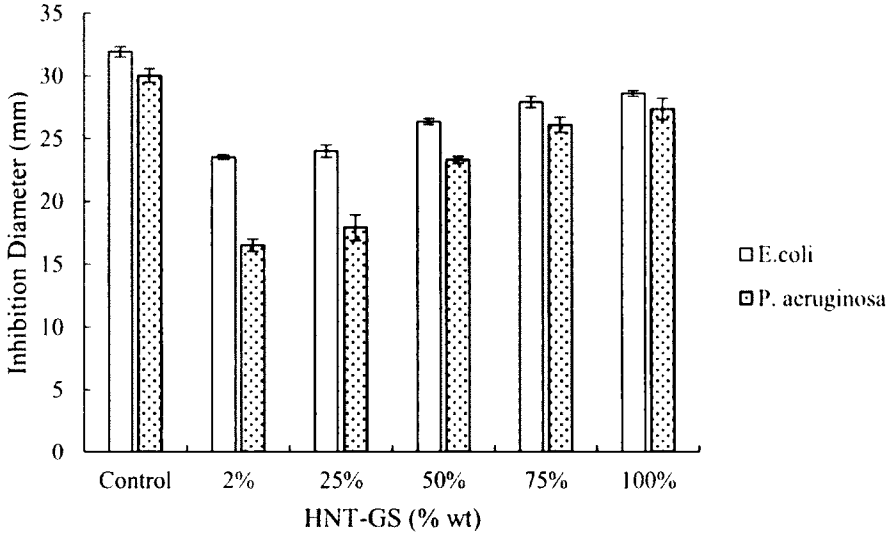

Figure 3-12: Inhibition diameters for *E. coli* and *P. aeruginosa* at different concentrations of HNT-GS in CPC scaffolds (mean ± SD, n = 3).

Graph in **Figure 3-13** shows the inhibition diameters for CPC scaffolds loaded with HNT-NS. Inhibition zones for *E.coli* and *P. aeruginosa* were also compared.

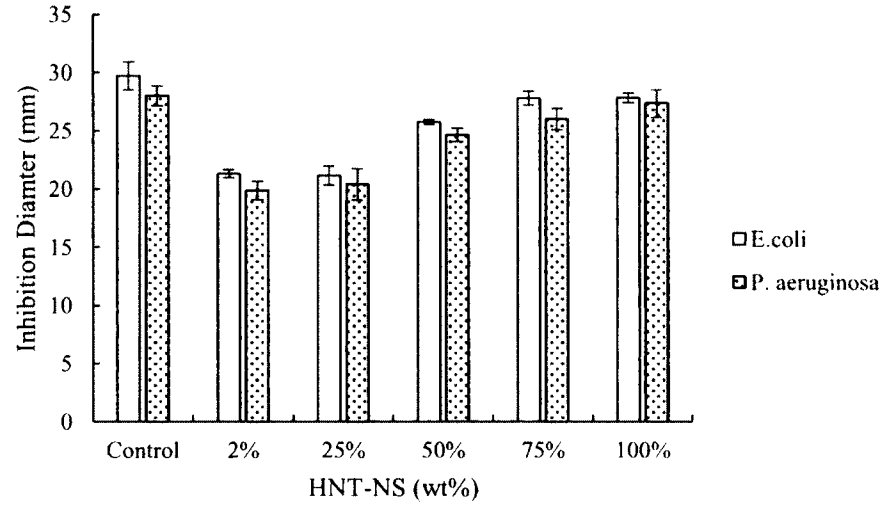

Figure 3-13: Inhibition diameters for *E. coli* and *P. aeruginosa* at different concentrations of HNT-NS in CPC scaffolds (mean ± SD, n = 3).

One-way ANOVA conducted on these samples showed a significant difference among mean values at the significance level of 0.05. With increase in HNT-NS concentration, zone of inhibition diameters also increased.

3.3 Conclusions and Future Work

3.3.1 Conclusions

Calcium-phosphate cements have been investigated for several decades, and in this study, we have manipulated the formulations to yield enhanced mechanical properties and extended-drug release. Previous studies had shown that incorporation of antibiotics directly into the cement yielded an improper drug release and reduced mechanical strength [107]. This reduced strength might be caused by a change in the crystal's structure or the dissolution of antibiotics to leave pores [14]. The cement must be formulated such that it can give an antibiotic property to the cement without compromising the mechanical properties. This result was achieved by the addition of HNTs in the CPC mixture. HNTs worked here both as the drug carrier and mechanical property enhancer.

In this study, addition of HNTs to the cement mixture increased compression and flexural strengths. SEM imaging reveals that the CPC scaffolds have rough surface with embedded micro-pores. This surface roughness might increas the cell attachment and the micro-pores aid in propagation of cells within the scaffold making the cement osteoconductive.

Cell viability assay on human osteoblast cells with CPC-HNT scaffolds showed no deleterious effects on the cells, proving that formulated CPC scaffolds do not cause harm *in vivo*. In addition, an increased viability was recorded with the addition of HNTs.

As HNTs are hollow and have high length/diameter ratio, they naturally have the ability to be loaded with substances and to yield a prolonged release. Because of this property, when HNTs loaded with antibiotics are mixed with the CPCs, they gave extended-release profiles. As the loaded HNTs are also present inside the scaffolds, we believe drug release would continue for several days when cement starts degrading to form bone. Zone of inhibition studies show that the scaffolds were able to inhibit bacterial growth and provide an anti-infective field at the site of implantation.

3.3.2 Future Work

In this study, only antibiotics were used for testing the anti-microbial properties of the CPCs. Multiple anti-infective agents such as anti-viral and anti-fungal can also be loaded into HNTs for synergistic and wide range anti-microbial properties. Bone growth hormones such as BMP-2, BMP-6 and others can also be loaded in the HNTs and can be used to promote bone healing along with providing an anti-infective field around it.

The present *in vitro* study showed that CPC scaffolds are osteoconductive and can be considered as a potential implant material. These scaffolds can be tested *in vivo* in mice, rats or other suitable specimens.

CHAPTER 4

3D PRINTING ANTIBIOTIC AND CHEMOTHERAPEUTIC LOADED BIODEGRADABLE SCAFFOLDS

4.1 Introduction

Currently used implants include metallic rods, pins, plates, screws, and acrylic cements which support the injured bone and hold it in position. Although these traditionally used implants have been proved clinically efficacious, they stay at the site of implantation permanently, need secondary revisions and surgical removal upon healing [5]. Metal implants are often removed to prevent or correct complications such as accumulation of metals in tissues [108], cessation of tissue growth in and around the implant [109], trauma, and implant migration [110]. Most of these implants are bulk manufactured, do not account for individual differences, and must often be machined according to the patient's requirements. This approach could increase both operative time and cost.

Additionally, the risk of microbial infection, especially for open-fractured bone fixation and joint-revision surgeries, is always high [111]. Sources of the infection include bacteria on the patient's skin, microbes already residing in the patient's body, surgical equipment used, environment of the operating room, and clothing worn by medical and paramedical staff [112]. Current implant technology could be improved to make the implants more biocompatible and anti-microbial in nature.

Recent advances in biomaterials for medical use have offered a promising alternative to these permanent implants. Biodegradable implants offer economical and clinical advantages over metal implants [113]. They can provide a necessary amount of mechanical strength, and degrade at a pace similar to new tissue formation. These implants can transfer the load safely to the newly formed bone and eliminating the need for revision/removal surgery [114]. Permanent implants including metals (titanium alloys, stainless steel, cobalt-chromium alloy), ceramics, acrylic cements and rigid synthetic plastics (polyethylene and polyurethane) are often cited for stress shielding due to their rigid nature [115] and interfere with the imaging techniques during post-operative analysis.

In the present work, methods to introduce anti-infective and chemotherapeutic properties to the filaments used in 3D printing were fabricated. Different constructs resembling the medical implants currently used, such as beads and catheters, were 3D printed. Changes in compression and flexural strengths with print orientation, infill ratio and drug addition were studied. Surface morphology was studied using SEM. Bacterial culture and osteosarcoma cell culture were performed to test the bioactivity of the constructs.

The basic foundation for this work was a part of a group project with Jeffery Weisman. Data obtained from SEM imaging, bacterial inhibition cultures and XTT assay were shared with Jeffery Weisman.

4.2 Materials

All plastic wares such as 2 ml Eppendorf tubes, 96 well plates, and pipettes were purchased from Mid Scientific, St. Louis, MO. Dulbecco's Phosphate Buffered Saline

(DPBS), Dulbecco's Modified Eagle's Medium (DMEM), Fetal Bovine Serum (FBS), and penicillin-streptomycin-amphotericin (PSA) antibiotics were purchased from Life Technologies, Grand Island, NY. For bacterial culture, 100 mm Mueller Hinton agar plates were purchased from Fischer Scientific (Hampton, NH) and Escherichia coli ATCC 11775 Vitroids 1000 CFU were from Sigma Aldrich (St. Louis, MO). Methotrexate (MTX), Gentamicin Sulfate (GS), tobramycin and nitrofurantoin were ordered from Sigma Aldrich (St. Louis, MO). PLA pellets used for extruding filaments were obtained from Push Plastic (Springdale, AR), KJLC 705 silicone oil used for coating pellets was purchased from Kurt J. Lesker Company (Jefferson Hills, PA). ExtrusionBot filament extruder was bought from ExtrusionBot, LLC (Pheonix, AZ), MakerBot replicator 3D printers were purchased from MakerBot (Brooklyn, NY), Nanodrop used for spectrophotometry was from Thermo Scientific (Wilmington, DE), and the Vulcan A550 series benchtop Muffle furnaces from Thomas Scientific (Swedesboro, NJ) was used for heating biomaterials. OPTA reagent, isopropyl alcohol and sodium tetra borate were ordered from Sigma Aldrich (St. Louis, MO). For modeling 3D constructs, Solidworks 2015 was used. For 3D scanning of objects, A Roland Corporation LP-250 desktop 3D scanner (Osaka, Japan) was used.

4.2.1 Bioplastics

PLA is an aliphatic polyester, approved by the US Food and Drug Administration (FDA) for direct contact with biological fluids [116]. Pellets with diameters 3-5 mm were ordered from Push Plastic, Springdale, AR. **Figure 4-1** shows the chemical structure of PLA and a bag of pellets.

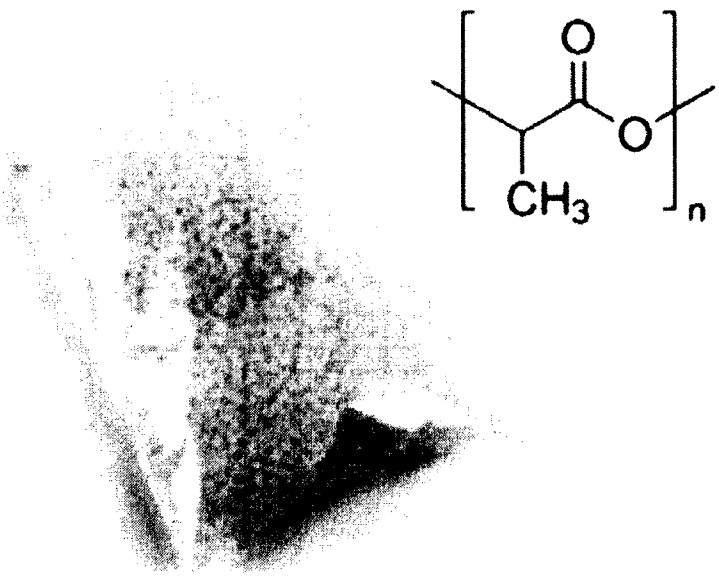

Figure 4-1: A bag of PLA pellets and its molecular structure.

In this study, these PLA pellets were used for extruding filaments and 3D printing constructs with drugs loaded.

4.2.2 Computer Modeling

The Solidworks 2015 was used to desgin all the constructs required for testing the properties of printed scaffolds. **Figure 4-2** shows the interface of the program with a stent design.

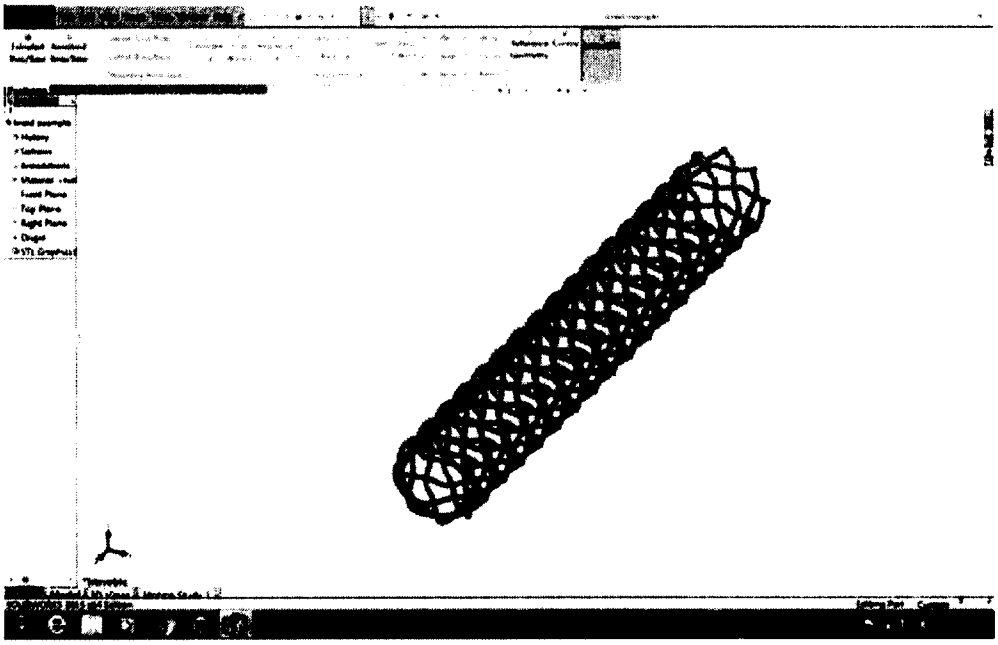

Figure 4-2: Solidworks 2015 interface showing a design of the stent.

All the constructs designed in this CAD program were saved in STL format in order to make these files readily available for the 3D printer to print.

4.2.3 Filament Extruder

For extruding filaments out of coated PLA pellets, a first generation ExtrusionBot filament extruder, shown in **Figure 4-3**A, was used.

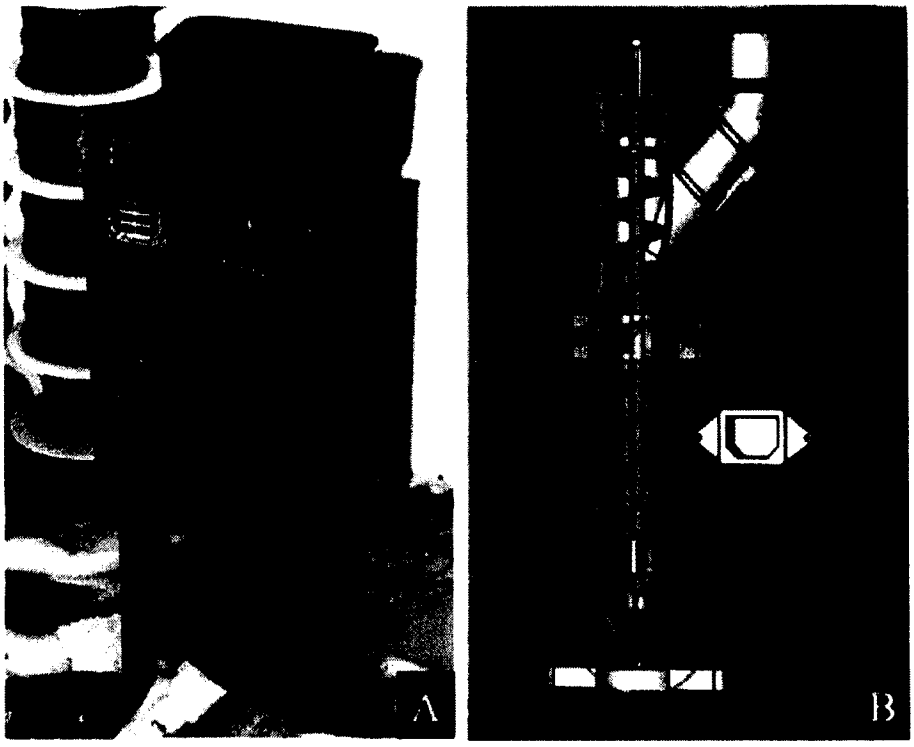

Figure 4-3: A) ExtrusionBot filament extruder, B) Piston based auger system inside ExtrusionBot.

This device works on a principle of piston based auger mechanism. Plastic pellets were fed into the hopper at the top of the device. The piston pushes the pellets down to the metallic die through heated element as shown in **Figure 4-3**B. Sensors arranged around this heating element regulate the temperature. Dies of different diameter at the bottom of the device can be used to customize the thickness of the extruded filament.

4.2.4 3D Printer

MakerBot 1st generation and MakerBot 5th generation, shown in **Figure 4-4**A and B, respectively, were used to print the extruded filaments.

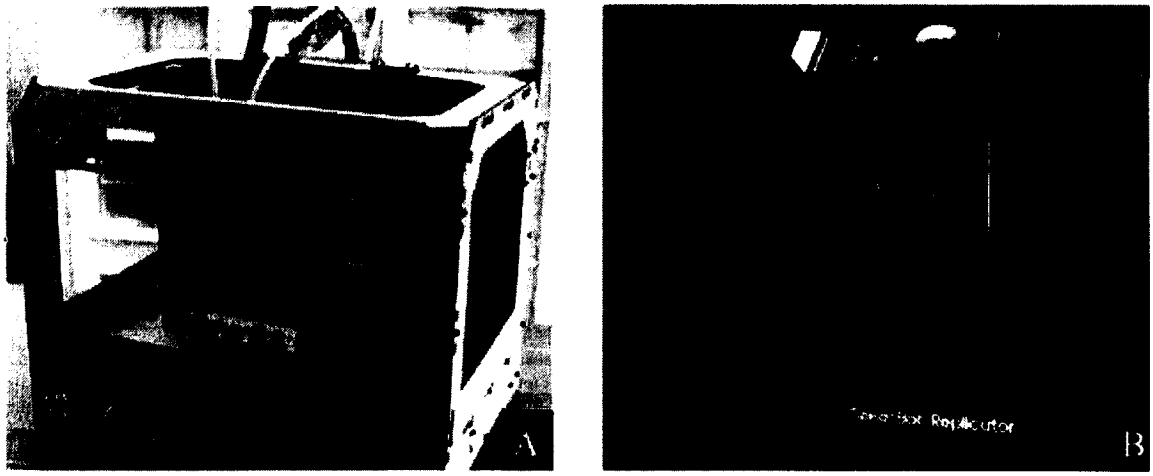

Figure 4-4: A) MakerBot Replicator 1st Generation, B) MakerBot Replicator 5th Generation.

These printers work on FDM principle. These devices provide a three-axis movement consisting of two simultaneous translational movements of a printer-head along the x and y axes and an additional movement by the printer platform along the z axis. Inside the printer-head lies a metallic barrel where filaments are electrically heated and extruded under computer control through a nozzle. **Figure 4-5** shows the interface of the Makerware software and its customizable settings.

Figure 4-5: Screenshot of Makerware software showing customizable settings.

The MakerBot replicator 1st Generation has two printer heads, whereas the 5th Generation has only one head attached. Both of these require filament of 1.75 mm in diameter to print objects. They are designed to print PLA and ABS plastics. The temperature they used to print is typically 220°C for PLA and 235°C for ABS. As with the temperature, the resolution of the object to be printed can also be customized within the range of 50-400 microns. The percentage of infill for the constructs can also be modified.

4.2.5 3D Scanner

A Roland LP-250 desktop 3D scanner was used (**Figure 4-6**) to scan 3D objects.

Figure 4-6: Roland LP-250 desktop 3D scanner.

This scanner uses a software called PICZA to convert the scanned data into a STL file for either CAD program or a 3D printer to read. An object is placed on the rotating bed of the scanner and it rotates the object 360°. At the same time, a laser beam travels vertically upwards collecting the data from the object into a digital file. For complex shaped objects, it scans multiple times and merges all the scans to generate an accurate representation.

4.3 Extruding Drug Loaded Filaments

Loading drugs into biopolymers and engineering them into a suitable form for printing into constructs was a challenge. Added to that, PLA is not available

commercially as fine powder. It is obtained easily in the form of pellets of different shapes and sizes. Since these are plastic, grinding them into fine powder was a difficult task. Freeze fracturing pellets into powder is an expensive and difficult option. We have come up with the following method to coat pellets with the drugs and these coated pellets were extruded into filaments of 1.75 mm in diameter for 3D printing constructs.

4.3.1 Coating Pellets with Drugs

To enable an even dispersion of drugs on the surface of the commercially available PLA pellets, an oil coating method was used. **Figure 4-7** shows an illustration of oil coating method. To surface coat pellets, KJL 705 silicone oil was chosen because of its thermal stability at extrusion temperatures (170-180°C). The method required 20 gm batch of pellets, to which was added 15 μL of silicone oil and then vortexed to make sure all the pellets were evenly and completely coated. Once vortexed, the pellets were transferred to another container in order to avoid loss of drug powder due to sticking to the surface of the oil coated mixing container. After switching containers, a calculated amount of a drug in powdered form (gentamicin sulfate for anti-infective filament and methotrexate for chemotherapeutic filament) was added and vortexed again.

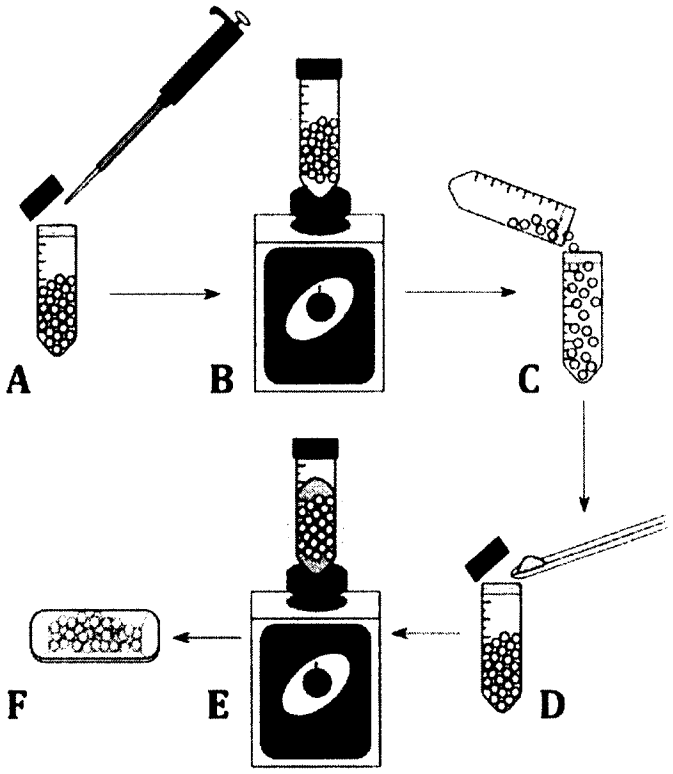

Figure 4-7: The process of coating PLA pellets with drugs. A) Coating oil is added, B) Tube is vortexed, C) Pellets are transferred to a new tube, D) Drug is added, E) Tube is vortexed, F) Coated pellets are removed [117].

Using this method, 1%wt GS-PLA pellets and 1%wt MTX-PLA pellets were made as shown in **Figure 4-8**. To make sure of uniform distribution, drugs were grounded with mortar and pestle prior to the addition.

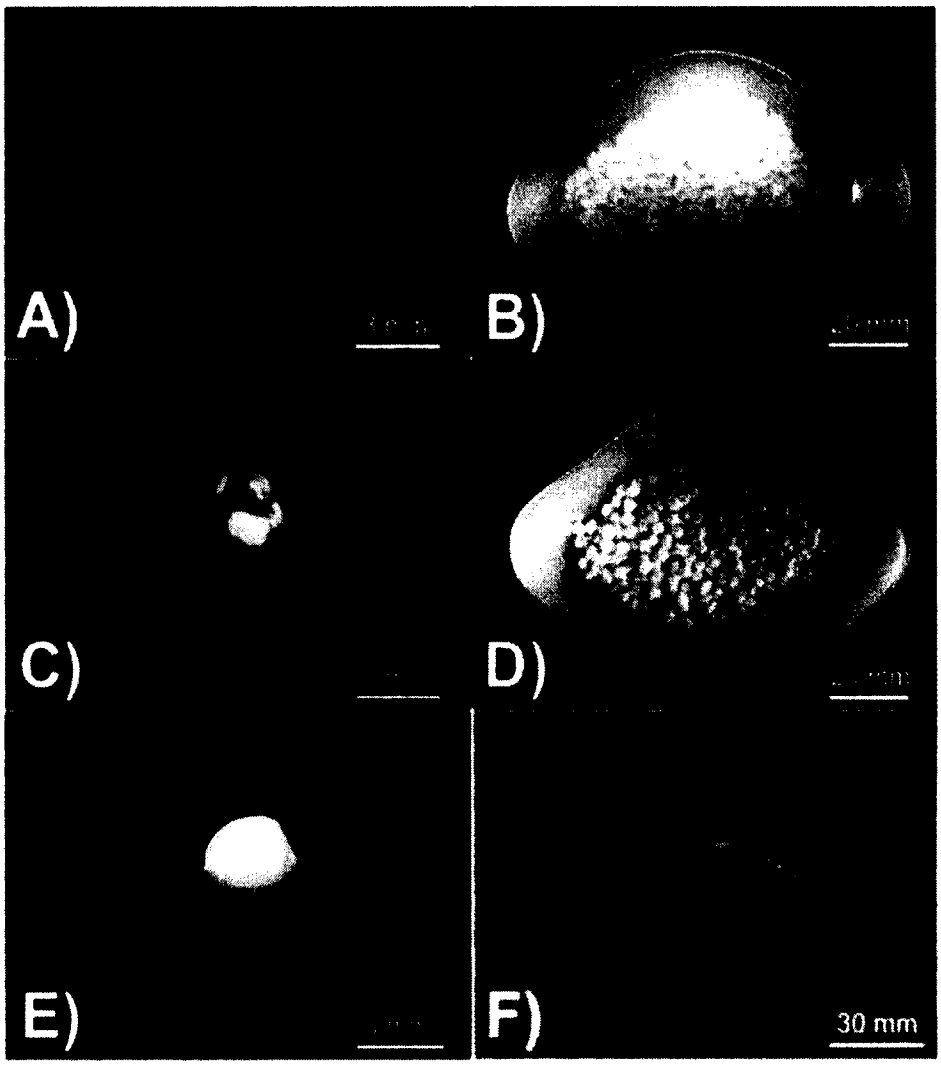

Figure 4-8: Drug coated PLA pellets. A-B) Control PLA, C-D) 1% wt GS coated pellets, E-F) 1% wt MTX coated pellets [117].

In addition to this, other methods such as direct mixing of drugs during extrusion and atomizer based coating were tried. These methods resulted in non-uniform coating of drugs.

4.3.2 Filament Extrusion

For extruding these coated pellets, an ExtrusionBot filament extruder was used. Since the 3D printer used requires a filament with a diameter of 1.75 mm to print, we have used metal die of the same diameter to extrude the filament. Each 20 gm of GS and

MTX coated PLA pellets were extruded at 170°C maintaining the outcoming filament diameter as 1.75 mm. We also tried extruding below 170°C, but that slowed down the extrusion speed and resulted in thicker filament which could not be used for printing. At higher temperatures, PLA melts down completely and flows through the metal die causing thermal runaway. Since this equipment works on piston based auger system, back pressure was necessary. Small batches of pellets could not provide sufficient pressure and stayed inside the extruder for a longer time period, resulting in excessive heating of the pellets and thin filament extrusion. For PLA, 20 gm batches extruding at 170°C were optimum conditions for getting a filament with a 1.75 mm diameter.

4.4 Optimization of 3D Printing Parameters

A 3D printer based on FDM is a very delicately balanced machine. If filament temperature, speed of extrusion and speed of the printer-head are not balanced together, it does not yield constructs of the required shape. Also, an optimized 3D printing process involves complex integration between hardware, software and material properties. Preliminary trials revealed that the printer head temperature and filament feed rate have a direct influence on the material flow for the fabrication of the scaffolds. For this reason, optimization of printing parameters for PLA was focused mostly on printer-head temperature and filament feed rate. We first determined the minimum temperature of the printer-head that could print PLA, and then we adjusted the filament extruding rate accordingly.

On the MakerBot 1st generation 3D printer, PLA could print at a lowest temperature of 215°C, and to compensate this, we had to decrease the printer-head speed from a default 40 mm/s to 10 mm/s and increase the filament feed rate from a default 18

mm/s to 23 mm/s. The workable range of parameter for a 1.75 mm diameter PLA filament was determined to be a 215°C printing temperature, 20-23 mm/s of filament feed rate and 12-8 mm/s printer-head speed.

4.5 Scaffold Design and Fabrication

All 3D CAD models were designed using Solidworks 2015 and Blender software. PLA scaffolds were fabricated for two sets of experiments. The first set of experiments was to study the effect of infill and printing axis on the mechanical properties of the scaffolds. The second set was to investigate the printed construct's bioactivity.

For the first set, compression cylinders with dimensions 6 x 12 mm and dumb-bell (dog bone) shaped bars of 75 x 10 x 4 mm were designed in solidworks CAD software. These models were sliced using replicatorG software and exported as .stl and .x3g formats for the printer to read. A honeycomb pattern of infill was used for all the constructs. To determine the effect on physical properties, scaffolds with different infill ratios 25%, 50%, 75%, and 100% were printed. Scaffolds were printed along different x, y and z axes, to check if the printing axis has any effects on mechanical strength.

For the second set, antibiotic loaded discs of 5 x 1 mm were printed for bacterial studies and chemotherapeutic discs of the same dimensions for osteosarcoma culture were printed. To replicate the currently used bone cement implants, beads of 6 mm diameter and 14 French catheters of 30 mm in length were also printed and tested for drug release and bacterial cultures. All the fabrication conditions were maintained the same as the first experimental set, except that these scaffolds were all printed at a default 10% infill.

4.6 Thermal Decomposition Testing

For extruding PLA filaments from pellets, they were run through the extruder at 170°C and for printing these extruded filaments, the printer-head needs a temperature of 220°C. To test the thermal stability, small batches of drugs (1 mg each) were heated in a Vulcan oven for five minutes at different temperatures (175°C, 195°C, 205°C, 215°C, 225°C, and 235°C) and were subjected to bioactivity testing. For antibiotics, standard muller hinton agar plates were used and for chemotherapeutics, a XTT assay on an osteosarcoma cell line was performed. All these samples were investigated in triplicate.

4.7 Scaffold Characterization

4.7.1 Morphology

For external morphology studies, the S4800 Field Emission SEM, HITACHI (Schaumburg, IL) at different magnifications was used. Extruded filaments, 3D printed constructs (discs, beads, and catheters) and controls were subjected to SEM.

4.7.2 Mechanical Properties

An ideal implant should have a proper balance of mechanical and physical properties. The optimization of properties such as hardness, elasticity, yield stress, wearability and time of degradation completely depends on type and functionality of the implant [118]. For example, sutures, catheters, surgical meshes and other smaller implants such as cochlear or vascular grafts do not need strong mechanical properties, whereas dental and orthopedic implants need higher load bearing capabilities. Due to this, we aim to customize the properties of the implants by changing the printing parameters to make them available for wide applications.

Scaffolds with different infill ratios, different orientations and with drugs loaded, as shown in **Figure 4-9** and **Figure 4-10**, were printed. These constructs were subject to compression and flexural testing.

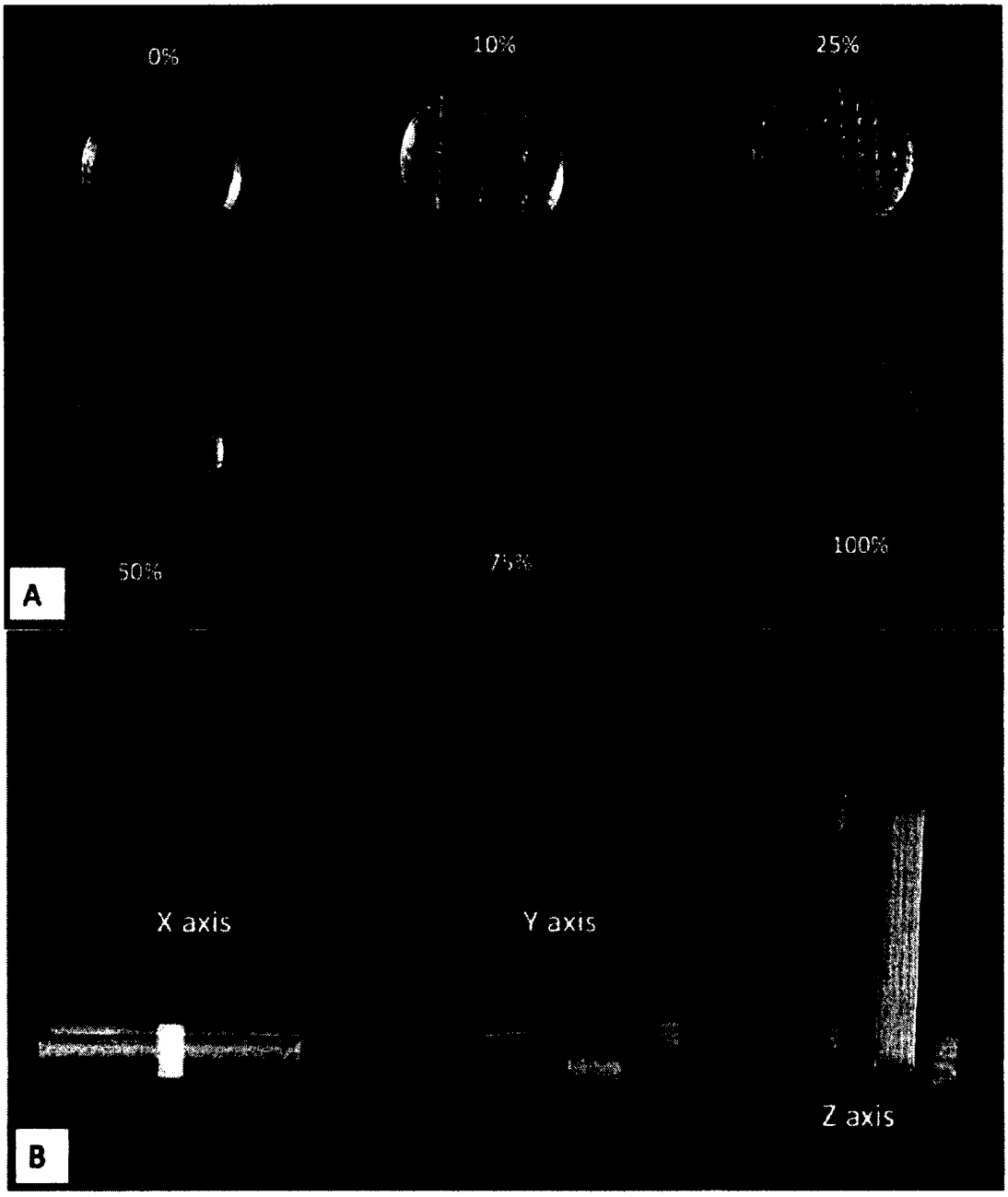

Figure 4-9: Printing PLA constructs with A) Different Infill ratios, B) Different Orientations.

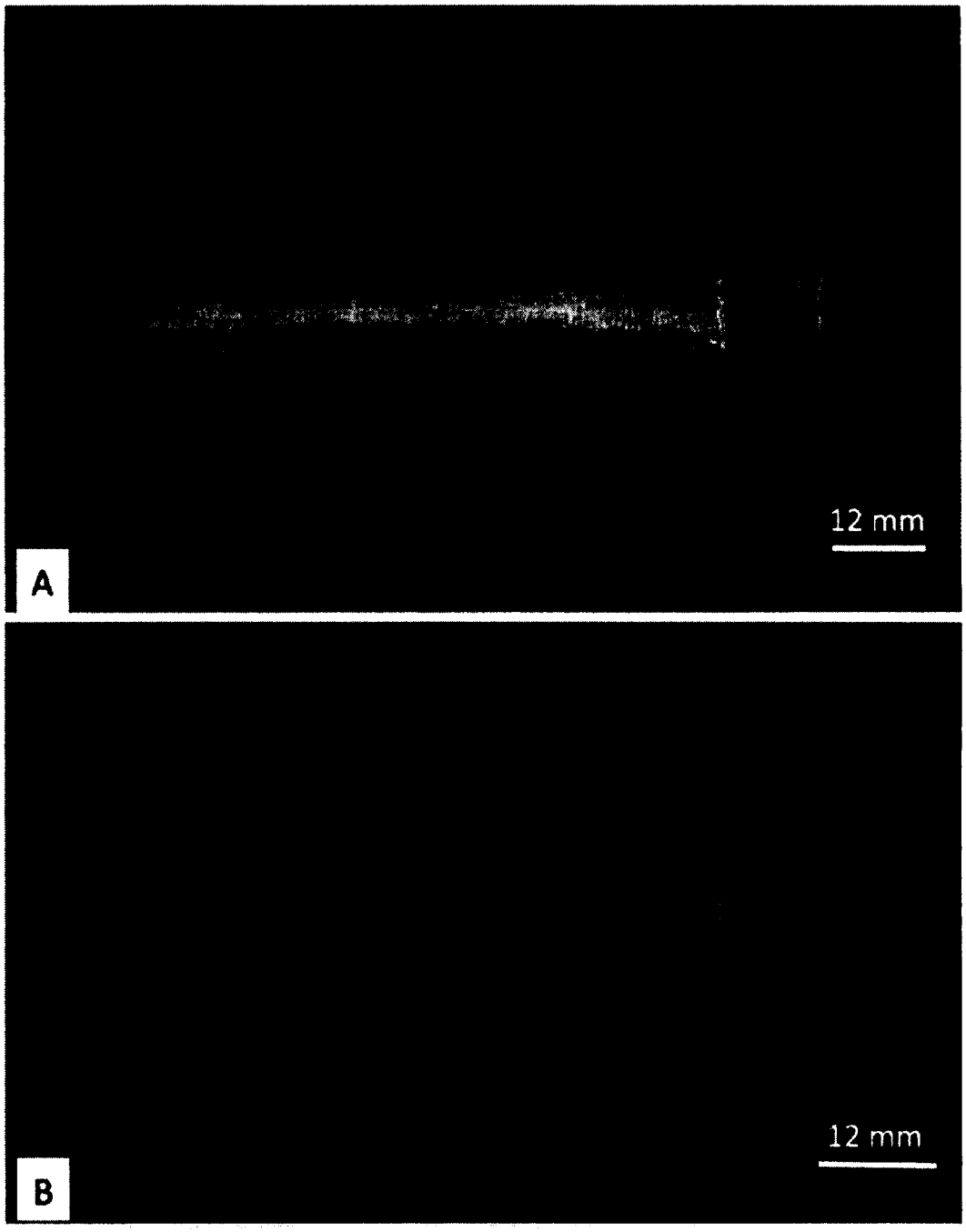

Figure 4-10: Printing PLA constructs. A) MTX-PLA mechanical testing samples, B) GS-PLA mechanical testing samples.

For testing the mechanical properties, both compression and flexural testing was performed using an Admet 2600 Dual Column Bench Top Universal Testing Machine.

For data acquisition and analysis, MTESTQuattro software was used and this was company equipped along with the instrument. For both tests, ASTM F451-99a (characterization of mechanical properties of bioresorbable scaffolds) guidelines were followed. Load capacity of 1 KN was laid on the scaffolds at a rate of 1 mm/min. The flexural testing three-point bending method, as shown in **Figure 4-11**, was followed.

Figure 4-11: Image showing three point bend testing performed on PLA samples.

4.7.3 Drug Release Profile

For drug elution profiles, a NANODROP 2000 UV-Visible Spectrophotometer from Thermo Scientific was used. Drug loaded extruded filaments (1 cm length), beads, catheters and control PMMA beads were subjected to this study. Simulated Body Fluid (SBF) was used to collect the samples from the constructs periodically. The time intervals for collecting samples were 1 minute, 2 minutes, 5 minutes, 10 minutes, 20 minutes, 40

minutes, 1 hour, 2 hours, 4 hours, 6 hours, 12 hours, and then daily for a week. For MTX, direct detection at 300 nm was performed. Since GS could not be directly detected, indirect determination using OPTA reagent was done. Equal volumes of collected sample, isopropyl alcohol and OPTA reagent were added, and this mixture was analyzed using spectrophotometer at 330 nm. SBF was used as a blank for all these tests. Measured quantities of drugs were used to draw standard graphs and from these absorbance values, the amount of drug eluted in the collected samples were back calculated. The graphs in **Error! Reference source not found.** and **Error! Reference source not found.** of the Appendix section were used as standards for calculating concentrations of GS and MTX from unknowns, respectively.

4.7.4 Bacterial Cultures

To assess the bacterial activity of GS, zone of inhibition studies were conducted on standard Muller Hinton Agar Plates using *E.coli* and *S. aureus*. For repeatability, vitroids of these two bacterial strains were ordered from Sigma Aldrich and used. These vitroids were rehydrated and inoculated into agar plates as per the procedures suggested in the manual. Plain PLA pellets, coated PLA pellets, extruded PLA filament, GS loaded PLA filament, beads and constructs were tested. To make sure there was no contamination among agar plates, a blank plate was cultured. An agar plate with just the bacteria acting as negative control and another with standard GS disc as positive control were also cultured. Under aseptic conditions, samples were inoculated along with the bacteria in the plates and incubated at 37°C for 24 hours. The diameter of inhibition zones was measured at three different points including the samples at the center of the zone and averaged.

4.7.5 Osteosarcoma Cell Culture

To test the chemotherapeutic activity of MTX, osteosarcoma cell line (CRL 2836) bought from ATCC (Manassas, VA) was used. These cells were incubated in complete DMEM having 10% FBS and 1% PSA at 37°C until they were confluent. These confluent cultures were passaged and seeded on to 96 well plates containing test scaffolds. A XTT assay was conducted on the third day of the experiment.

For this assay, control filaments, MTX coated filaments, control 3D printed discs and MTX PLA 3D printed discs were cultured along with the cells in 96 well plates. The XTT assay procedure was conducted as per the manufacturer's protocol. After aspiration of the media, each well was added with 100 μL buffer and 20 μL XTT dye. These plates were then incubated for 4 hours and photometric absorption of each well was measured using Phenix LT-4000 absorbance microplate reader at 450 and 690 nm. The manufacturer's protocol followed for this assay is mentioned in **Appendix B**.

4.7.6 Statistics

All mechanical testing samples were studied in multiples of five to make sure the results are consistent, reproducible and not altered by random events. For comparing the means of the strengths among the different groups, the one-way ANOVA test was performed at a significance level of 0.05. Post hoc analysis was used to calculate the highest average among the groups. Standard deviation was calculated and used in the graphs as error bars.

For drug elution studies and bacterial cultures, three samples of each batch were tested. Standard deviation of the means was calculated and used as error bars in the graph.

4.8 Results and Discussion

PLA pellets were successfully coated with drugs GS and MTX using oil coating methods. Optimization of the amount of silicone oil used to coat the pellets was challenging. Excess oil resulted in clumping of pellets together and clogging the extruder during extrusion process. However, low amounts of oil would only allow pellets to hold small proportions of drugs on to their surface. For a batch of 20 gm pellets, 10-15 μL of silicone oil was found to yield the best results. Filaments of 1.75 mm diameter were successfully extruded from coated pellets using the ExtrusionBot extruder at 170°C. These filaments were used in MakerBot 3D printers and scaffolds were printed. **Figure 4-12** shows images of scaffolds 3D printed using custom extruded bioactive filaments.

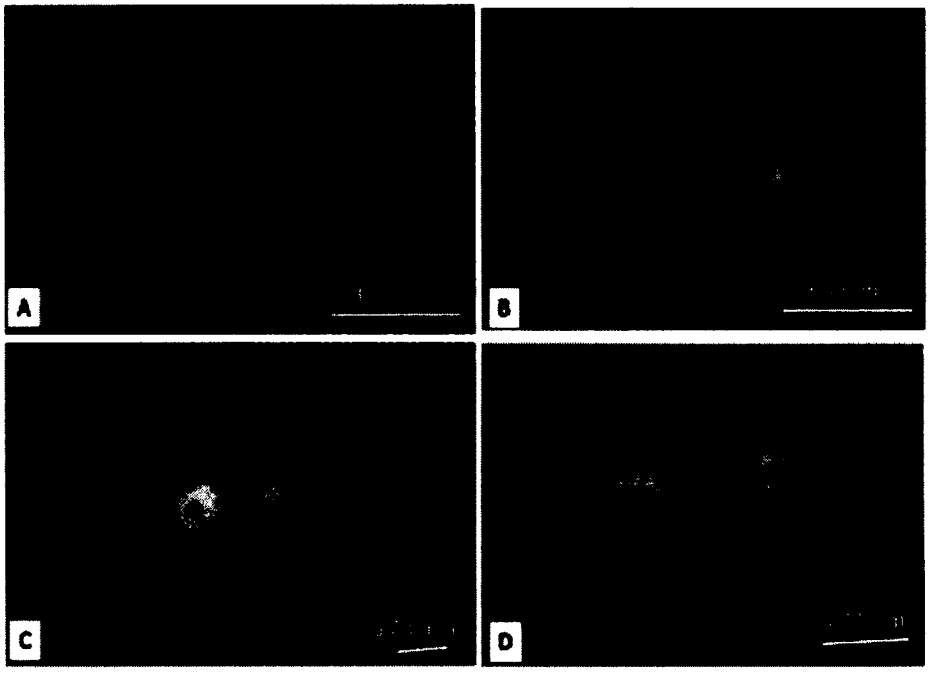

Figure 4-12: A) 1% wt GS-PLA catheters, B) 1% wt MTX-PLA catheter, compression cylinder and bead, C) 1% wt GS-PLA beads, D) 1% wt MTX-PLA beads.

4.8.1 Scanning Electron Microscopy (SEM)

SEM was used for studying the surface morphology of the coated pellets, extruded filaments and printed scaffolds. **Figure 4-13** shows images of pellets coated with drugs. GS particles were round in shape and the spheres had a wide range of diameters (from 1 μm to more than 50 μm), whereas MTX particles were polygonal in shape and are varied in sizes.

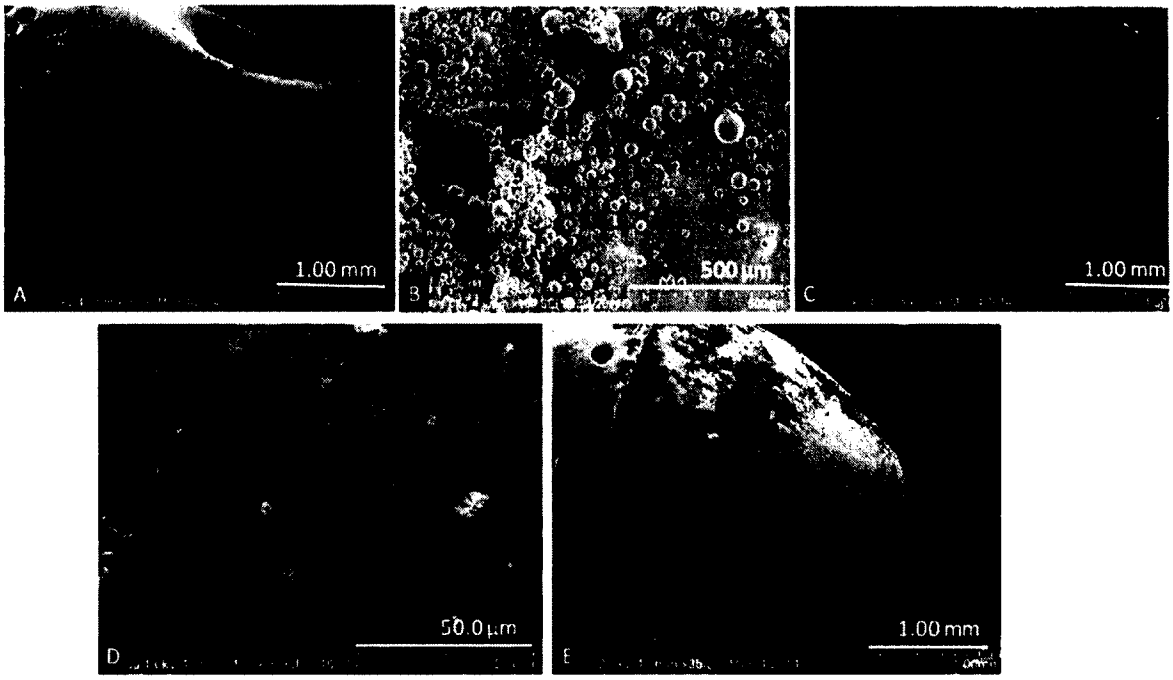

Figure 4-13: SEM of A) Control pellet, B) GS powder, C) 1% wt GS-PLA pellet, D) MTX pellet, E) 1% wt MTX-PLA pellet. Images D and E were also used in Jeffery Weisman's dissertation [117, 119].

Extruded filaments comprise a cylindrical shape with a 1.75 mm diameter. The SEM images in **Figure 4-14** show the surface morphology of Control, GS and MTX filaments.

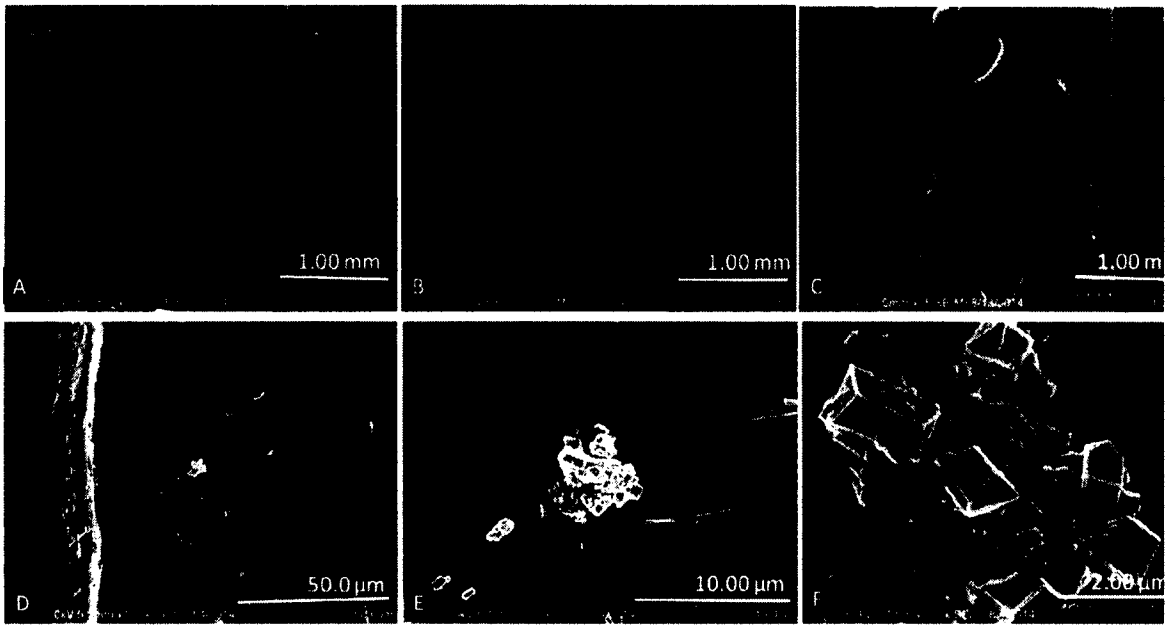

Figure 4-14: SEM of A) Control filament, B) 1% wt GS-PLA filament, C) 5% wt GS-PLA filament, D) 1% wt MTX-PLA filament, E-F) MTX crystals on the surface of filament at different levels of magnification. Images D and F were also used in Jeffery Weisman's dissertation [117, 119].

The images of control and 1%wt GS filaments does not show much difference between them. However, increasing the concentration of GS showed distortion on the surface of the filament as shown in **Figure 4-14 C**. This might be the reason for 5% wt GS filaments to be brittle and not print smoothly. The surface of the 1% wt MTX filaments were also smooth, cylindrical in shape and deep yellow in color. On further magnification, trace amounts of MTX crystals were seen on the surface of the 1% wt MTX filament.

SEM images in **Figure 4-15** shows the surface morphology of 3D fabricated beads and catheters.

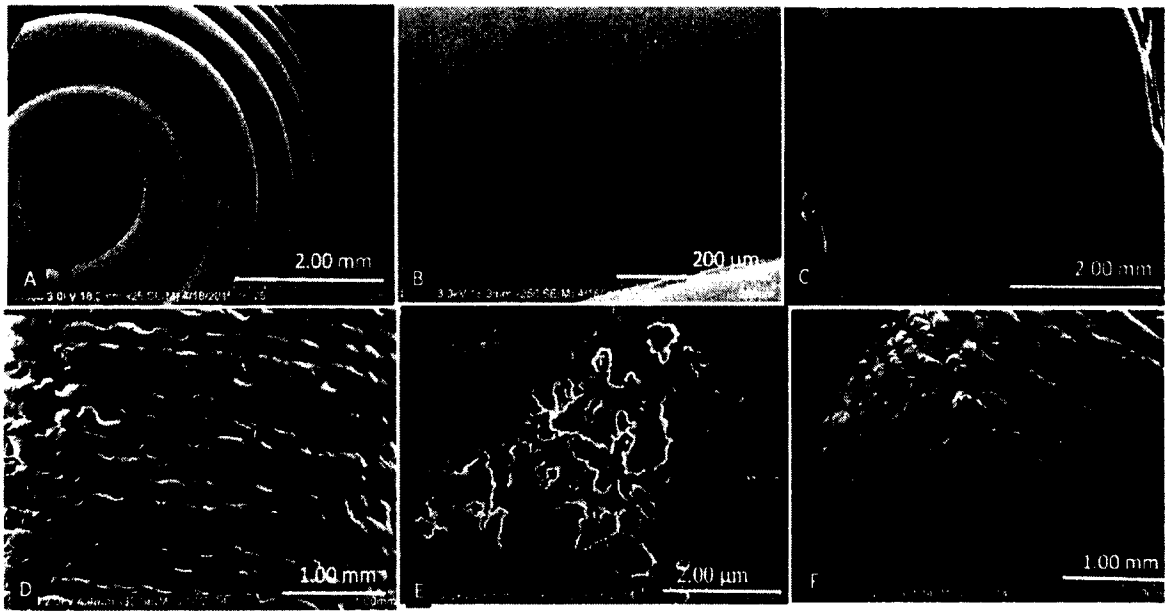

Figure 4-15: SEM of A) 1% wt MTX-PLA bead, B) MTX powder on surface of the bead, C) 1% wt MTX-PLA catheter, D) 1% wt GS-PLA catheter, E) GS on the surface of the catheter, F) 1% wt GS-PLA bead. Images D-F were also used in Jeffery Weisman's dissertation [119].

These images show the layers of filament being deposited on top of each other like a stack of rope. These filament layers comprise a cylindrical shape with 300 µm in diameter and good sintering between the layers. The image in **Figure 4-15** (A) shows the sintered layers of the 1% wt MTX-PLA bead, on increased magnification MTX particles can be seen on the surface. Similarly, the image in **Figure 4-15** (D) shows the surface of the sintered layers of 1% wt GS-PLA catheter and upon further magnification individual GS particles can be seen on its surface in **Figure 4-15** (E).

4.8.2 Mechanical Properties

The flexural strengths of different 3D printed control PLA scaffolds with different infill ratios and orientations are summarized in **Figure 4-16**.

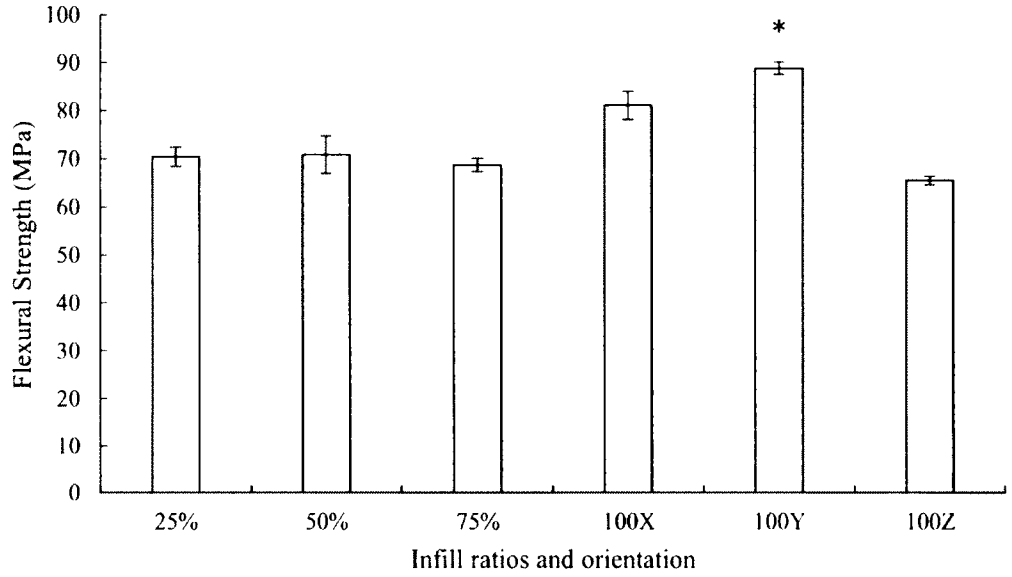

Figure 4-16: Flexural strengths of PLA constructs printed in different infill ratios and orientations (mean ± SD, n = 5). Statistical significant differences are marked with * for $p < 0.05$.

There was no significant difference seen between 25%, 50% and 75% infill samples and the 100% infill samples had the highest flexural strengths. Among different orientations, samples printed along the Y axis showed high flexural strengths. Samples printed along the X axis had 8% less and along the Z axis had 26% less flexural strengths when compared to Y axis prints. This might be due to the alignment of filament layers along the length of the specimens, whereas in other orientations, filaments were sintered with each other perpendicular to the length of the specimen.

The graph in **Figure 4-17** shows the flexural strengths of PLA samples printed with and without drugs. Extruded control PLA prints had mean flexural strength of 78 MPa. Samples printed with GS and MTX showed a 14.4% and 17.1% decrease in strengths, respectively.

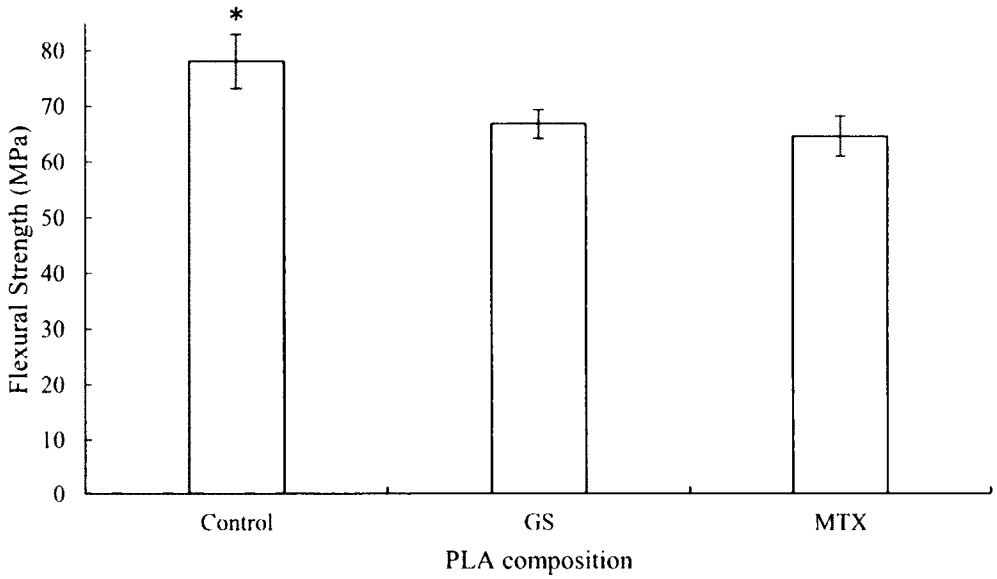

Figure 4-17: Flexural strengths of control, GS and MTX-PLA constructs. (mean ± SD, n = 5). Statistical significant differences are marked with * for $p < 0.05$.

Unlike flexural strengths, compression strengths of the samples printed with different infill ratios showed a significant difference in their mean values. Graph in **Figure 4-18** shows the stress-strain curves of PLA constructs and **Figure 4-19** shows the compression strengths of samples printed with different infill ratios and in various orientations. Samples printed at 100% infill ratio showed the highest compression resistance among other infills. There was no significant difference in means of compressive strengths printed at different orientations.

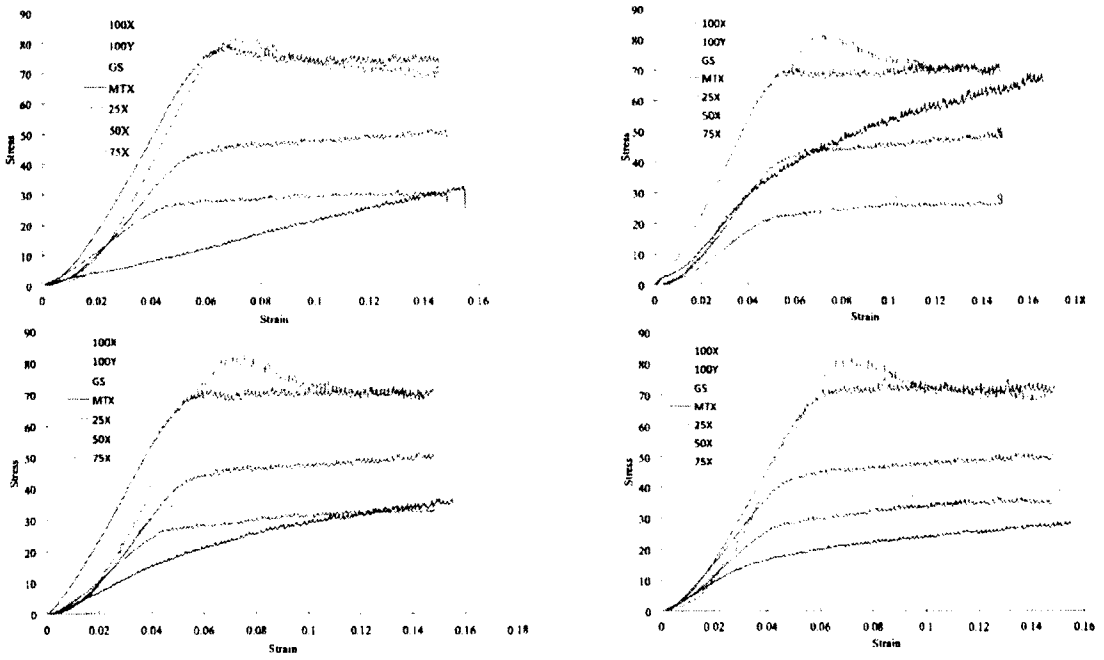

Figure 4-18: Stress-Strain curves for different trails of PLA constructs.

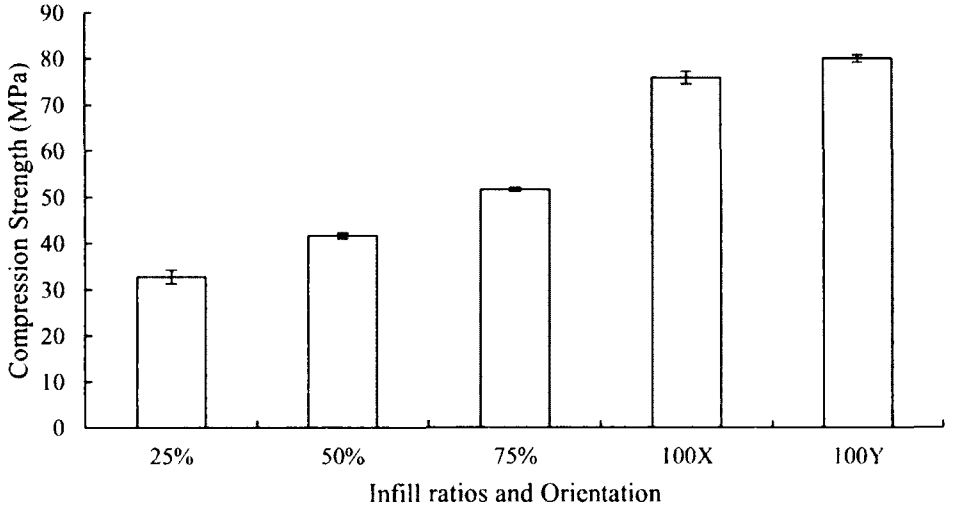

Figure 4-19: Compression strengths of PLA constructs printed at different infill ratios and orientations (mean ± SD, n = 5). Statistical significant differences are marked with * for $p < 0.05$.

The graph in **Figure 4-20** shows the compression strengths of PLA samples with different drugs. The control PLA scaffolds had compression pressure of 67.66 MPa. Scaffolds with GS and MTX had 48% and 42% reduction in compression strength, respectively.

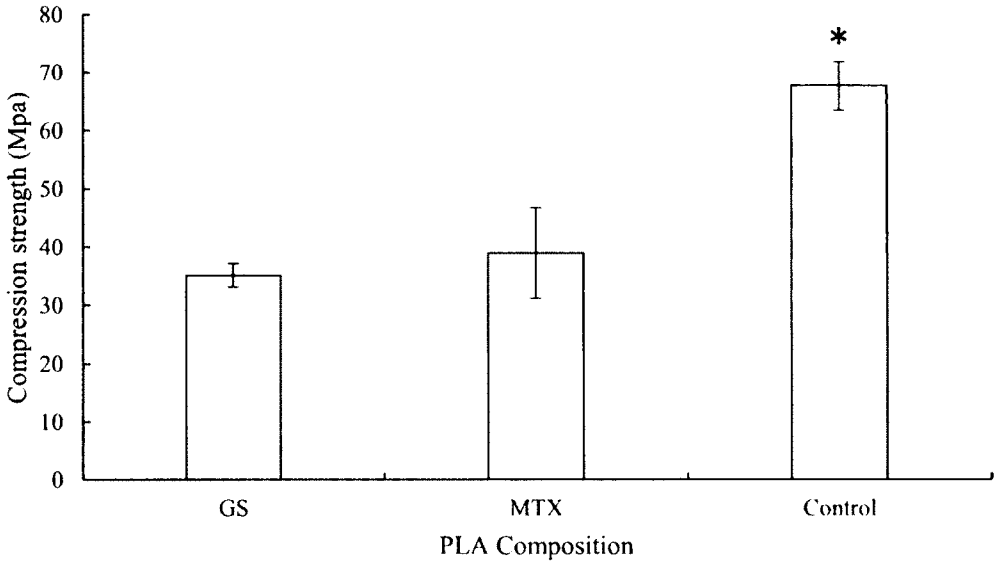

Figure 4-20: Compression strengths of control, GS and MTX-PLA constructs (mean ± SD, n = 5). Statistical significant differences are marked with * for $p < 0.05$.

4.8.3 Drug Release Profiles

The graph in **Figure 4-21** shows the cumulative concentration of drug released from the 3D printed PLA-GS scaffolds and PMMA bead at different intervals of time. The cumulative concentration of drugs released were plotted with respect to time. As it can be seen, all scaffolds showed an initial outburst during the first few hours followed by a steady release. This initial burst may be due to rapid diffusion of drug from the external surface of the scaffolds. The following steady release may be attributed to

diffusion of drug from the scaffold matrix. The active ingredient dissolves into the liquid within the scaffold matrix and then diffuses into the bulk medium.

The amount of GS released from the 3D printed bead was less when compared to a GS loaded PMMA bead. Even after a week, all the scaffolds were still releasing GS within the working concentration.

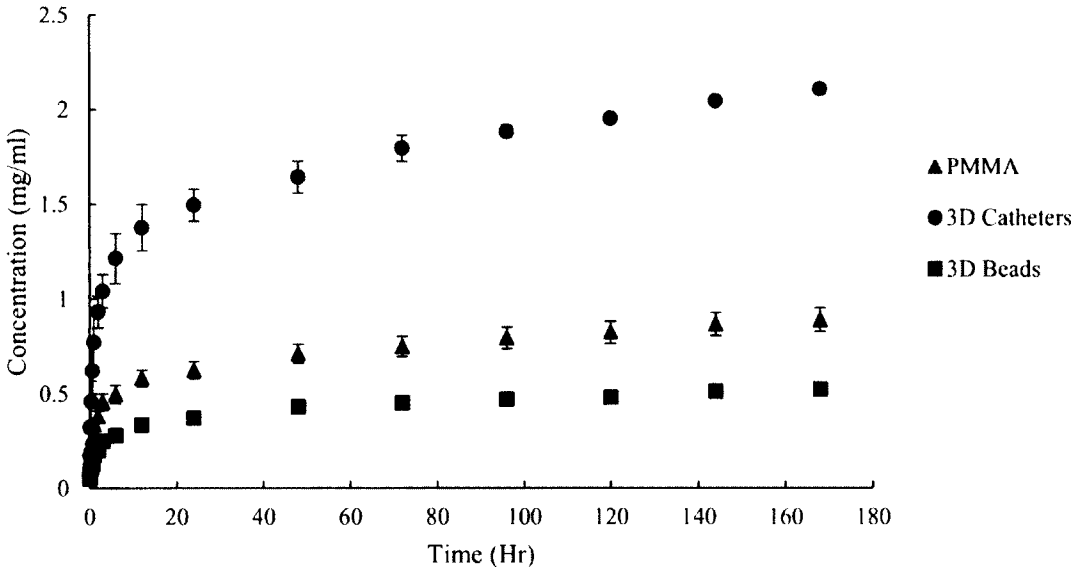

Figure 4-21: Cumulative concentration of GS eluted from 3D printed PLA bead, catheter and hand mold PMMA bead (mean ± SD, n = 3).

For MTX release study, 3D printed bead and catheter along with PMMA bead was used. Among these samples, only 3D printed catheter and PMMA bead were eluting drug within the detectable range. This might be due to hydrophobic nature of the drug or may be drug-polymer interactions. Higher concentrations (2.5% wt and 5% wt) of MTX filaments were extruded, catheters were 3D printed and used for elution. Graphs in **Figure 4-22** and **Figure 4-23** show the cumulative drug elution from different concentrations of PLA-MTX catheters and PLA-PMMA bead.

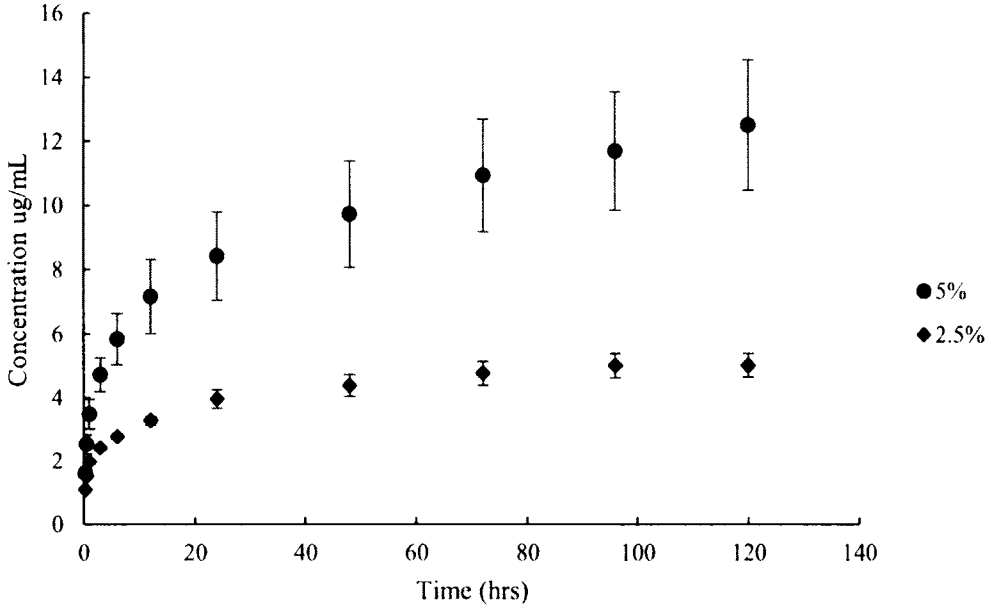

Figure 4-22: Cumulative concentration of MTX released from 3D printed PLA catheters (mean ± SD, n = 3).

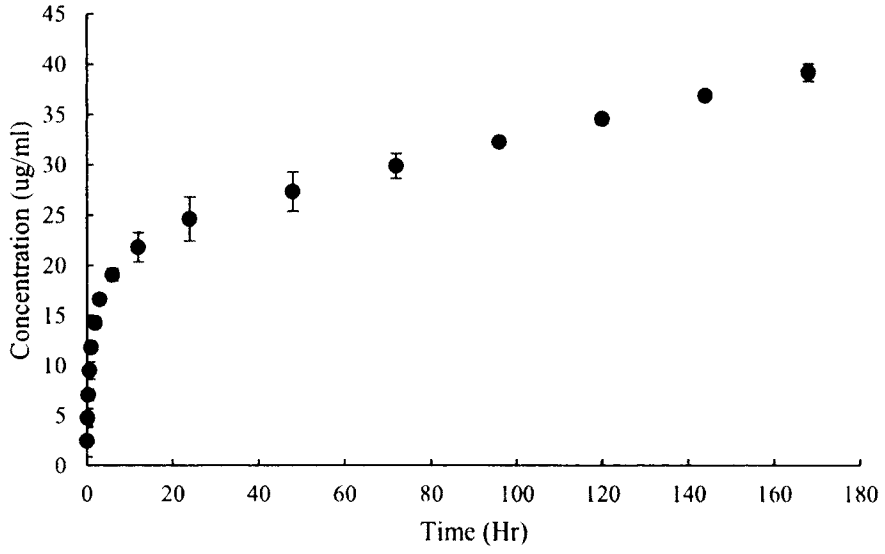

Figure 4-23: Cumulative concentration of MTX eluted from PMMA bead (mean ± SD, n = 3).

The release profile of MTX from PMMA was similar to GS-PMMA elution. At the end of 120 hours, 34.57 µg/ml (cumulative concentration) of drug was released from the PMMA bead, whereas 2.5% and 5% MTX 3D printed catheters could elute only 5 µg/ml and 12.5 µg/ml (cumulative concentration) of MTX, respectively.

4.8.4 Bacterial Culture

For a PLA thermoplastic to be extruded and 3D printed, it has to undergo heating process up to 170°C for filament extruding and 215°C for 3D printing. So studying the thermal degradation of drugs used is necessary. GS batches of each 100 mg were heated at different temperatures for five minutes in a Vulcan oven and 1 mg of it is incubated along with the *E. coli* in agar plates. All these experiments were performed in multiples of three. **Figure 4-24** shows the zones of inhibition for GS heated at different temperatures.

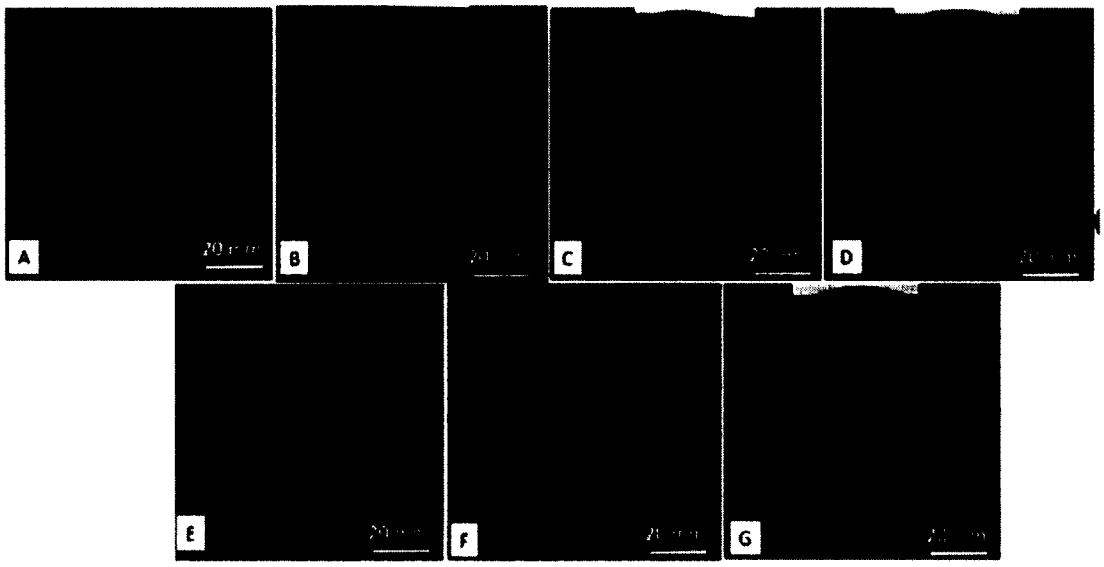

Figure 4-24: Zone of Inhibitions for GS heated at different temperatures on *E. coli* cultures A) Controlled uncooked, B) 175°C, C) 195°C, D) 205°C, E) 215°C, F) 225°C and G) 235°C.

The average zone of inhibition for control GS was 37.39 mm and for GS heated at 175°C was 36.62 mm. ANOVA analysis showed no significant difference between the two means. **Figure 4-25** shows the mean zone of inhibition values for GS heated at different temperatures for five minutes. A total of 11.07% reduction in inhibition diameter for GS heated at 195°C when compared with control. Similar inhibitions were recorded for 195°C and 205°C heated GS groups. Makerbot 3D printer used temperature of 215°C for printing PLA filaments. For GS group, heated at 215°C, at total of 21.03% reduction in inhibition zone and 54.2% reduction for 235°C group was recorded.

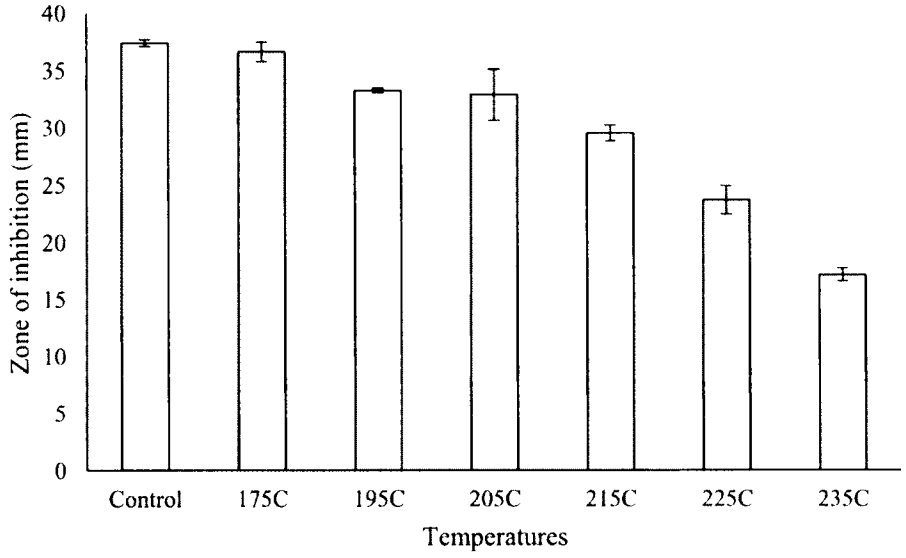

Figure 4-25: Zone of inhibition for GS heated at different temperatures (mean ± SD, n = 3).

The images in **Figure 4-26** shows the zone of inhibition for GS coated pellets, filaments and 3D printed discs. PLA pellets coated with 2.5% wt GS showed an average of 29.04 mm diameter zone of inhibition. Control PLA and PMMA filaments, as shown in **Figure 4-26 A**, did not show any kill zones. Clear demarcating inhibition zones were

seen for PLA and PMMA filaments loaded with GS. The mean zone of inhibition for 2.5% wt PLA-GS was 23.13 mm and 2.5% wt PMMA-GS was 22.58 mm. ANOVA analysis showed no significant difference between the two means.

Similarly, the mean zone of inhibition diameters of 3D printed discs and hand mold PMMA discs were 21.36 mm and 22.02 mm, respectively. ANOVA analysis showed no significant difference in the mean values of both groups.

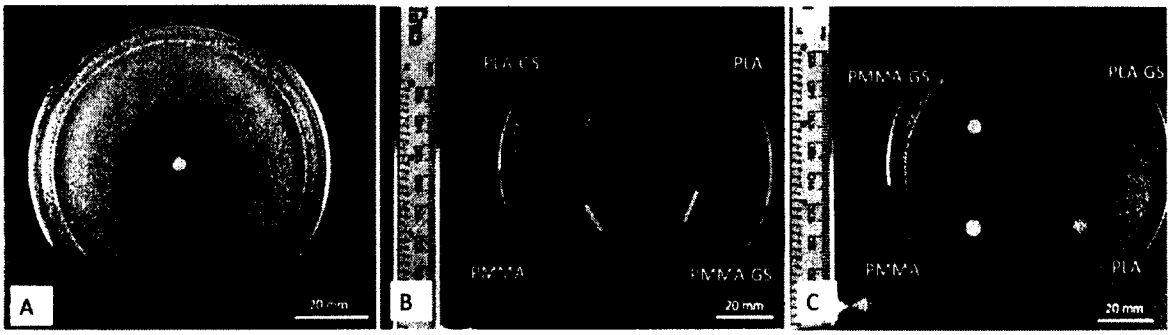

Figure 4-26: Zone of Inhibitions for *E. coli* cultures A) PLA-GS pellet, B) PLA and PMMA filaments with and without GS, C) PLA and PMMA discs with and without GS. Image A was also used in Jeffery Weisman's dissertation.

The 3D printed beads and catheters also showed a clear demarcating zone of inhibitions. **Figure 4-27** shows the inhibition zones for PLA-GS beads and catheters incubated with *E. coli*.

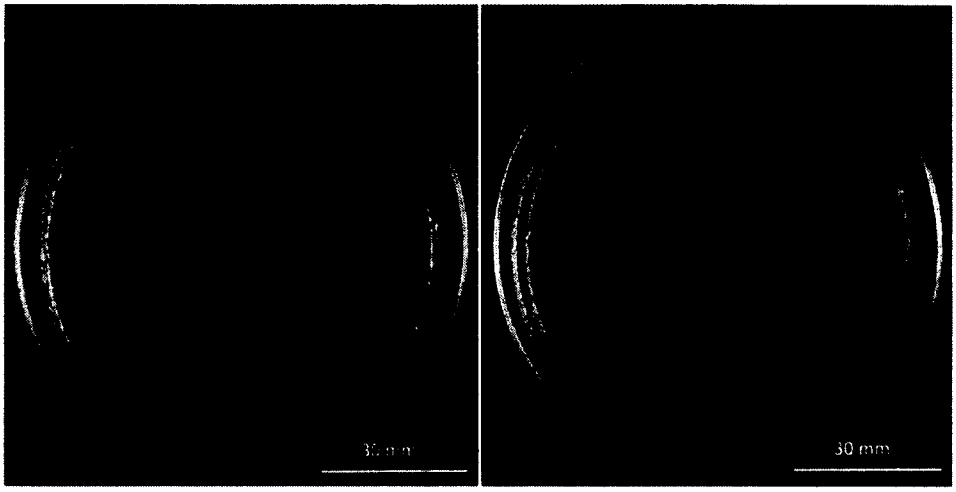

Figure 4-27: Zone of Inhibitions for PLA-GS bead and catheter on *E. coli.*

The same method was followed for fabricating tobramycin-PLA constructs. The tobramycin laden discs showed no zones of inhibition as shown in **Figure 4-28**. However, clear zones were seen for PMMA-tobramycin discs. This may be due to low melting of tobramycin or its interactions with the polymer.

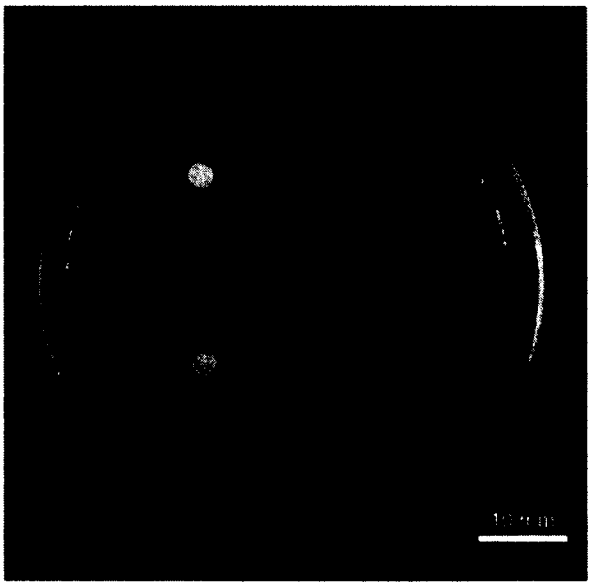

Figure 4-28: A) 1 wt% tobramycin PMMA disc, B) 1 wt% tobramycin PLA disc, C) 2.5 wt% tobramycin PMMA disc, D) 2.5 wt% tobramycin PLA disc [119, 117].

4.8.5 Osteosarcoma Cell Culture

Since bioactive compounds undergo fabrication process involving temperatures up to 215°C, thermal stability study was necessary. **Figure 4-29** shows the absorbance values of XTT assay performed on osteosarcoma cells at day one. It is to be noted that these absorbance values correspond to the growth of the cells. The absorbance of the well was directly proportional to the susceptibility of the cells. Five wells of each sample was used for the assay. Both control MTX and heated MTX showed significant differences in absorbance values when compared to control cells. A total of a 65.41% reduction in absorbance values was recorded for groups containing MTX. ANOVA was performed and there was no statistical difference between the mean values of MTX control and MTX heated.

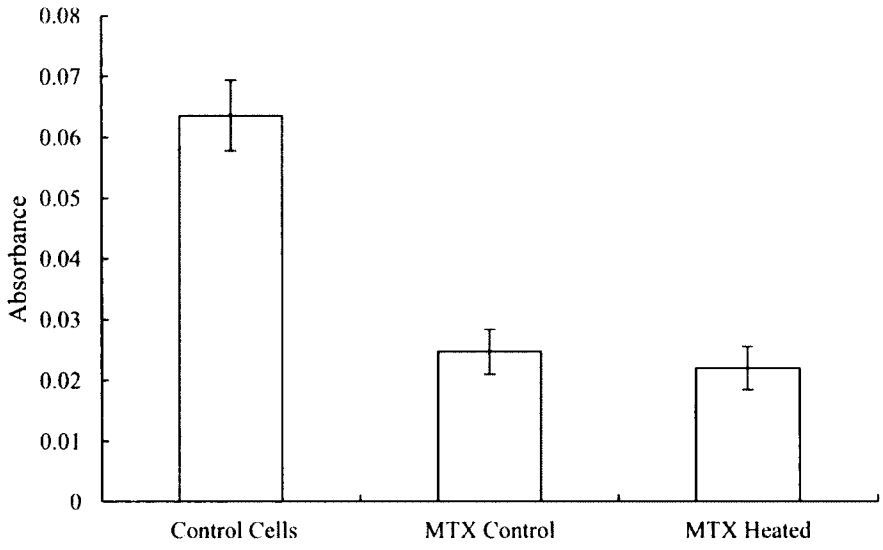

Figure 4-29: Absorbance values of XTT assay performed on osteosarcoma cells with different MTX groups at day one (mean ± SD, n = 3).

MTX enhanced PLA filaments were also tested on 96 well plates. In this study, eight test groups with six wells each were used: control cells, control MTX, heated MTX,

control PLA pellet, oil coated PLA pellet, MTX coated PLA pellet, control PLA filament, MTX PLA filament. An enhanced cell growth was recorded in groups lacking MTX as shown in **Figure 4-30**.

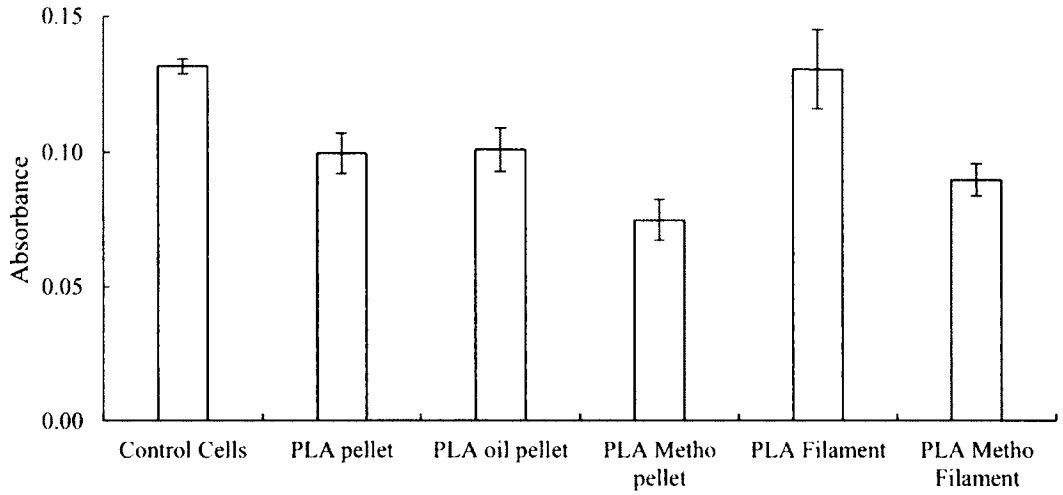

Figure 4-30: Absorbance values of XTT assay performed on osteosarcoma cells with different PLA scaffolds enhanced with MTX (mean ± SD, n = 6) [117].

PLA pellets coated with silicon oil and uncoated PLA pellets showed no statistical differences in their mean absorbance values when compared with control cells. There was no significant difference between PLA filament and control cell groups either. Wells containing MTX pellets and MTX filaments showed a significant decrease in cell proliferation when compared to both the control well and PLA filament control well. A total of 43.15% and 31.72% reduction in absorbance values was shown in MTX pellets and MTX filament groups. ANOVA analysis confirms statistical differences between XTT viability assays of the methotrexate enhanced filament/pellet and the respective control groups.

4.8.6 Scanning Bone Defects

In bone diseases such as osteomyelitis and osteosarcoma, affected regions of the bone will be debrided out by the surgeon and those defects could be refilled with drug eluting spacers. Using CT scans of the bone, defective parts can be identified and spacers can be 3D printed with accurate dimensions before the physician could even start surgery. This process will help in reducing the total duration of time taken for the surgery. In this part of the study, a cow femur was used to model this concept. Irregular and standard 6 mm defects were made using drill press machine on the femur bone as shown in **Figure 4-31**.

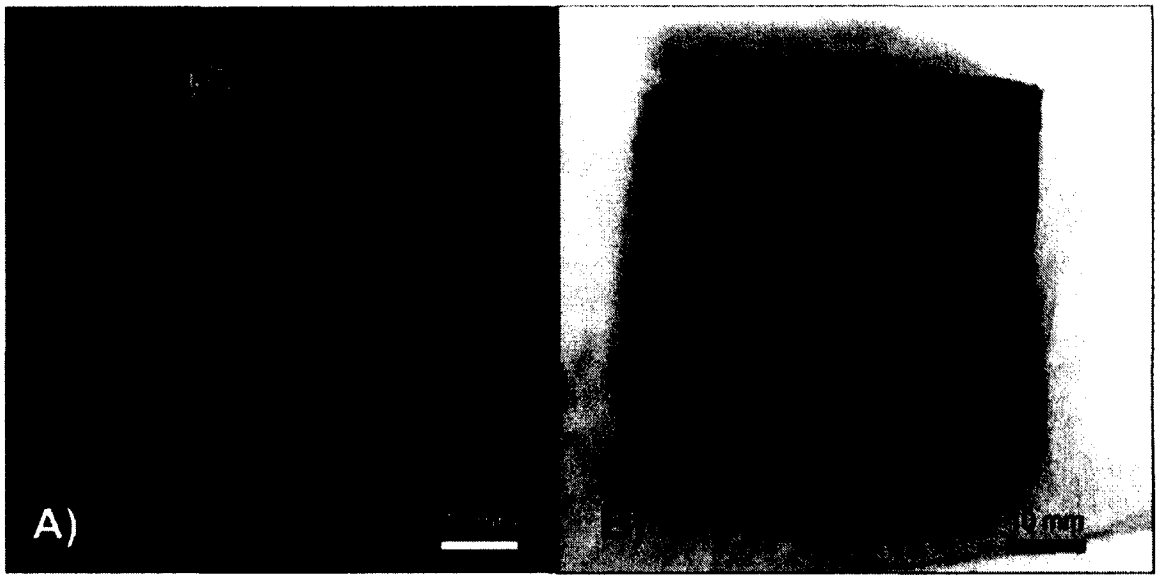

Figure 4-31: A) Cow femur with irregular bone defect, B) Cow femur with 6 mm diameter defects 1 wt% [119].

Using the Roland Desktop 3D scanner, the bone was scanned and defective regions were manually processed using blender and solidworks software. These processed bone defects were saved as STL files and 3D printed using customized drug

loaded filaments. **Figure 4-32** shows the images of a 3D scan of the bone, processed bone plugs and 3D printed bone plugs.

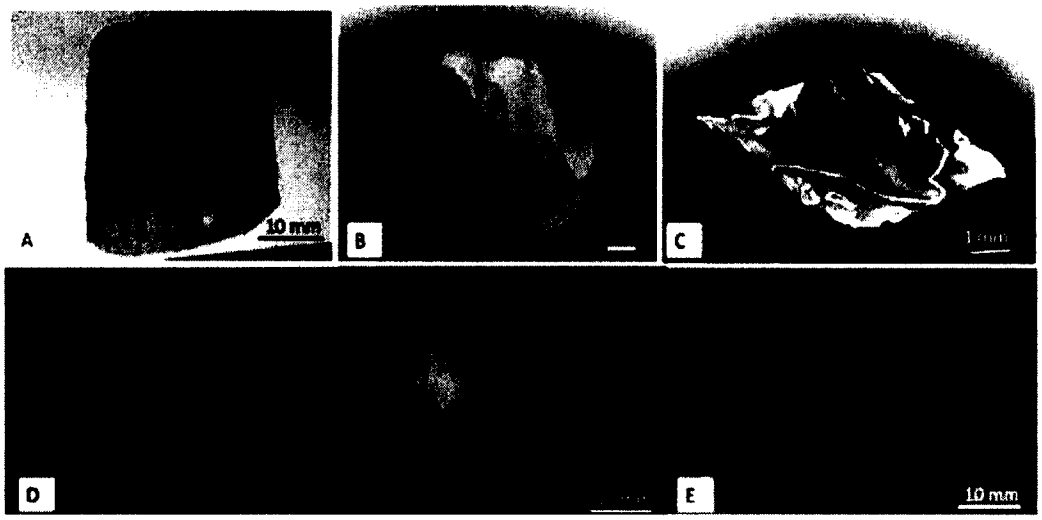

Figure 4-32: A) 3D raw scan of cow femur showing 360 degrees of defect in 180 degree image, B) CAD rendering of negative 6 mm diameter defect, C) CAD rendering of negative of irregular defect, D) 1wt% gentamicin print of irregular defect with control, E) MTX print of irregular defect. Images in A-D were also used in Jeffery Weisman's Dissertation.

Control PLA, GS-PLA and MTX-PLA bone defects were printed and test fitted over the defects. 3D fabricated bone plugs were found to fit the defects precisely. Images in **Figure 4-33** shows bone plugs fitted into the bone defects.

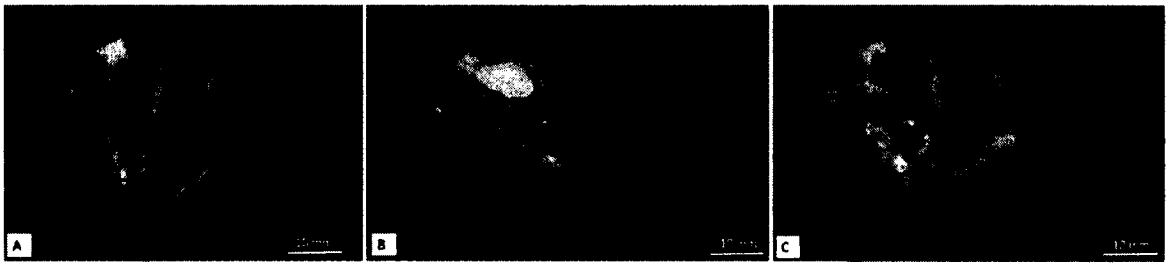

Figure 4-33: A) Femur with irregular defect, B) Femur with control-PLA fitted insert, C) Femur with GS-PLA fitted insert [119].

4.9 Conclusion

Recent advances in additive manufacturing and biomaterials provide the potential to 3D fabricate custom constructs for personalized medicine with targeted drug delivery. A novel method for coating biodegradable PLA pellets with bioactive compounds and extruding them as filaments of required diameter was developed. These extruded filaments were successfully printed into constructs of required shapes such as beads, catheters and others. Antibiotic coated pellets, extruded filaments and 3D printed beads were tested in bacterial cultures to confirm their anti-infective property. The results indicated that the GS loaded constructs retained their bioactivity and provided clear anti-infective regions around them. Similarly, XTT assay performed on osteosarcoma cells showed significant reduction in cell growth among groups containing MTX filaments and printed discs when compared to control groups.

SEM images showed coating of drugs on the surface of the pellets. These images also showed the presence of bioactive compounds on the surfaces of the extruded filaments and 3D printed constructs. Comparison testing done with PMMA bone cements showed equivalent or superior bioactive properties of these fabricated scaffolds.

There was a significant reduction in mechanical strengths of the PLA constructs due to addition of bioactive compounds. Increasing the strengths of the constructs using nanoparticle technology or by using other additive polymers should be further investigated. Drug elution data showed a burst release of bioactive compounds for the first couple of hours and then a steady release for 144 hours. Furthermore, by regulating the 3D printing parameters such as infill ratio and resolution, external surface area and

hollowness of the constructs vary and thus increase or decrease the amount of drug elution.

Finally, novel techniques were engineered to 3D scan and print custom constructs using bioactive filaments. These techniques show the potential of 3D printing to create personalized medicines with targeted drug delivery.

CHAPTER 5

3D PRINTING HORMONES LOADED BIODEGRADABLE CONSTRUCTS

5.1 Introduction

Osteoporosis is a critical bone health issue with devastating effects, especially for the aging population. Estrogen deficiency causes postmenopausal women to be at high risk of developing osteoporosis and subsequent bone fractures [120]. Estrogen is a crucial hormone in the pathogenesis of osteoporosis, although the exact mechanism by which estrogen deficiency causing bone-mineral loss is not clearly understood [121, 122]. Some studies have focused on the role of estrogens in down-regulating the proinflammatory cytokines (IL-1, IL-6, TNF-α, PGE_2 and other macrophage colony-stimulating factors) that aids in osteoclast functions and increases the bone resorption [123, 124]. Other studies have found that estradiol prevents the activation of caspase-3 enzyme, which is a crucial initiating factor for apoptosis of osteoblast cells [125, 126]. Cenci *et al.* reported an increased bone loss/bone resorption in ovariectomized (OVX) mice, mediated by TNF-α [127]. These authors also showed that administration of estrogen hormones prevented ovariectomy-induced bone loss.

Hormonal Replacement Therapy (HRT) with estrogen is the most common and effective FDA approved pharmacotherapy used to treat postmenopausal osteoporosis [125]. Estrogens are available in various formulations and are administered via different

routes such as intramuscular, subcutaneous, percutaneous, transdermal, vaginal, and oral. Depending on the patient's profile and requirement, HRT is administered either as short-term (2-4 years) or in long-term (usually more than 5 years) therapy. HRT implants are usually in the shape of a small pellet or apple pips, made by fusing pure crystals of hormones, and they are available in doses of 50 mg -100 mg. These pellets are administered subcutaneously (under the fat lining of the skin) to provide a steady release of drug for a long period of time [125, 128]. Thigh, upper leg or lower abdomen are the common locations for implantation. In some cases, continuous administration of estrogen alone may cause uterus hyperplasia [129]. To prevent this, a combination therapy of estrogen and progesterone is prescribed.

In addition to osteoporosis, estrogen along with progesterone can cure vasomotor symptoms such as hot flashes, night sweats, dyspareunia and atrophic vaginitis. HRT is also used for a woman who has undergone hysterectomy (surgery where woman's uterus is removed) and for contraceptive effects. Intrauterine devices (IUDs) are considered to be excellent long-term birth control implants because of their safe, effective, and easy to use properties [130]. These are small T-shaped devices, as shown in **Figure 5-1**, made of flexible plastic and are placed directly into the uterus, releasing small amounts of hormones (estrogen and/or progesterone) for up to 12 years. These devices work by impairing sperm functions and preventing the fertilization of egg.

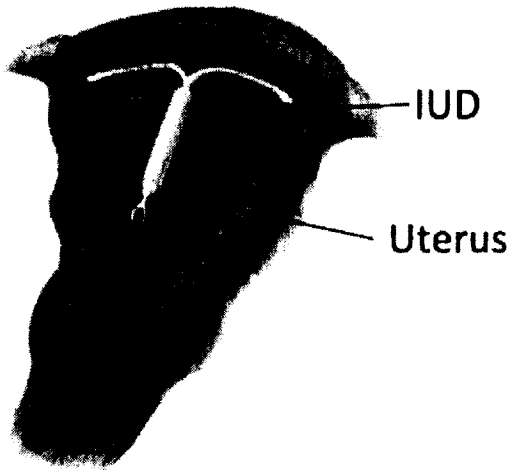

Figure 5-1: IUD positioned in the uterus [131].

Anatomically, the uterus is positioned in the pelvic region with various muscle tissues and ligaments. Age, pregnancy, or estrogen deficiency cause these muscles to weaken in some women, and the uterus drops into the vaginal canal causing a prolapsed uterus. Pessaries are medical devices used to treat these pelvic organ prolapses by providing structural support to the uterus, vagina, bladder, rectum and deliver female sex hormones locally [132]. These devices are made in different sizes and shapes as shown in **Figure 5-2**. A physician decides the best fit of the pessary to the patient by a trial and error testing procedure [133]. Locally released estrogen could strengthen the pelvic floor tissues by making the muscles stronger and thicker [134].

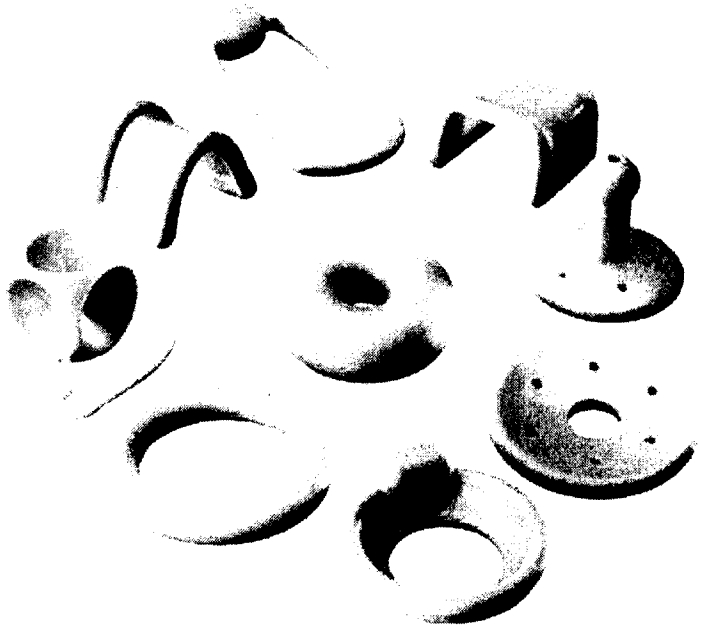

Figure 5-2: Pessaries of different shapes and sizes [135].

Currently available HRT implants are bulk manufactured with fixed doses, whereas every individual is unique and needs varied amounts of hormones. Commercially available HRTs do not account for the differences between individuals. 3D printing technology has simplified the generation of customized medications for patients. The advantage of customizing HRT is that it can be modeled specifically to fit the individual's body and hormone level. In this part of the research, methods to fabricate customized hormonal implants will be discussed. These printed constructs will be tested for external morphology, hormonal elution profiles and therapeutic efficacy.

5.2 Materials

The Polycaprolactone (PCL) pellets used for filament extrusion were purchased from Sigma Aldrich (St. Louis, MO). Estrogen hormone E1 (SLE 1048) was purchased from ScienceLab.com, Inc. (Houston, TX). E2 (CAS 57-63-6) and E3 (CAS 50-27-1)

were obtained from U.S. Pharmacopeia (Rockville, MD). Cell culture plates and other lab plastics were purchased from MidSci, St. Louis, MO. Rosewell Park Memorial Institute Medium (RPMI), Dulbecco's Modified Eagle's Medium (DMEM), fetal bovine serum (FBS), and penicillin-streptomycin-amphotericin (PSA) antibiotics were obtained from Life Technologies, Carlsbad, CA. Estrogen receptor luciferase reporter T47D stable cell line (Sl-0002-NP) was purchased from Signosis, Inc. (Santa Clara, CA). KJLC 705 silicone oil used for coating the beads prior to extrusion was purchased from Kurt J. Lesker Company (Jefferson Hills, PA). The 3D printing equipment consists of an ExtrusionBot extruder purchased from ExtrusionBot, LLC (Pheonix, AZ) and a MakerBot Replicator 5th Generation Desktop 3D printer (Brooklyn, NY). The nanodrop spectrophotometer was from Thermo Scientific (Wilmington, DE). The Solidworks 2015 student edition 3D CAD program Dassault Systèmes (Waltham, MA) and Blender (Amsterdam, NL) were used for modeling. ELISA kits for E2 and E3 were purchased from Enzo Life Sciences (Farmingdale, NY). To analyze ELISA assays, a SpectraMax M2e Multimode mircroplate reader purchased from Molecular Devices (Sunnyvale, CA) was used. The SEM was a hitachi S-4800 (Schaumburg, IL).

The filament extrusion devices, 3D printers, modeling software were previously described in Chapter 4. New materials are described in detail below.

5.2.1 Bioplastics

PCL was used as a thermoplastic polymer for loading hormones due to its lower melting temperature. It has a glass transition temperature of -60°C and melting point at 60°C. It starts to melt and flow between 80°C to 110°C depending upon the pressure applied.

5.2.2 Hormones

Synthetic female sex hormones E1, E2 and E3 were used for this research. These hormones are commercially available in powdered form, have chemical structures similar to natural hormones and act by competitively attaching to the estrogen receptors in the body. They have high melting temperatures of E1 (255°C), E2 (180°C), E3 (280°C) and are thermally stable [136].

5.2.3 Micro-plate Reader

A SpectraMax M2e multimode microplate reader from Molecular Devices was used to measure the absorbance values of the ELISA kits. Like any other plate reader, this works on principles of Beer-Lambert's law. SoftMax Pro software was used to run this machine. It also has the ability to run standards and calculate the concentrations of unknowns from the standard values. **Figure 5-3** shows the image of the microplate reader.

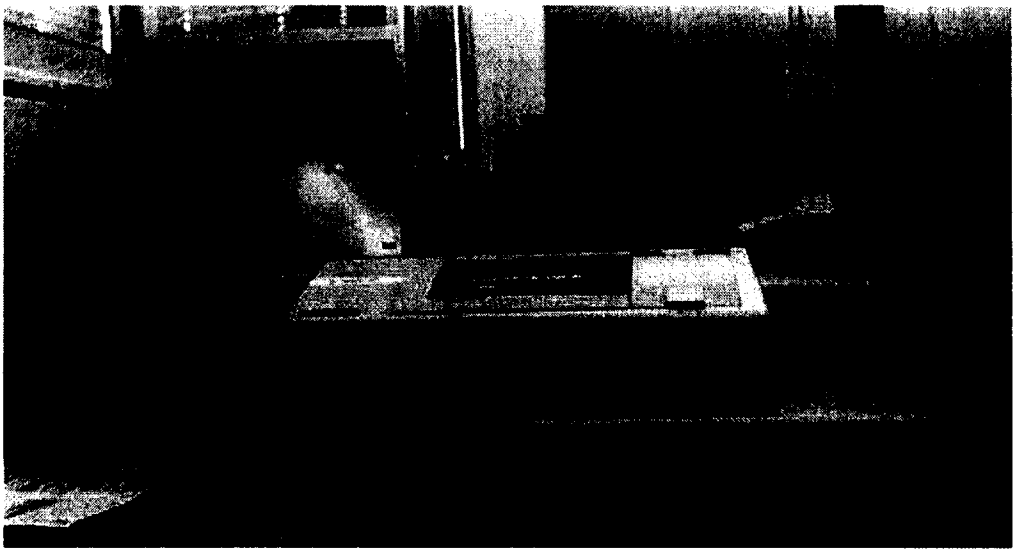

Figure 5-3: SpectraMax M2e multimode multiplate reader.

5.2.4 ELISA Kits for Hormone Quantification

ELISA kits for E2 and E3 were ordered form Enzo Life Sciences, Farmingdale, NY. There are no current active suppliers for E1-ELISA kits. These kits were competitive immunoassays for quantitative determination of hormonal concentrations in the samples. These kits use polyclonal antibodies to bind competitively to hormones present in the sample. After incubating at room temperature, excess reagents were removed, the substrate was added and the process was halted using stop solution. The optical density of the substrate was measured using microplate reader, and from those readings, concentration of hormones in the samples were calculated.

5.2.5 Estrogen Receptor Luciferase Reporter Cell Line

Estrogen receptors belong to the nuclear receptor family. They are wide spread and are responsible for varied physiological functions. Estrogen receptor luciferase reporter T47D stable cell lines were purchased from Signosis, Santa Clara, CA. In these cell lines, when estrogen or similar stimulants attach to the estrogen receptors in the nucleus, dimerization of these receptors takes place. These dimerized receptors attach to specific elements, located at the promoter site of genes, known as Estrogen Response Elements (EREs). Upon attachment with these EREs, genes get activated and start expressing. These particular cell lines express luciferase on estrogen stimulation and thus provide a sensitive and responsive *in vitro* system to detect estrogen activity.

5.3 Fabricating Hormone Loaded Scaffolds

For filament extrusion and 3D printing, methods mentioned in Chapter 4, Sections 4.3.1 and 4.3.2 were followed. PCL thermoplastic was used for loading hormones due to its low melting temperatures and excellent biodegradable and biocompatibility properties.

5.3.1 Extruding Hormone Loaded Filaments

PCL pellets were coated with calculated amounts of hormones and extruded using ExtrusionBot filament extruder in similar manner to PLA. Each 20 gm batches of E1, E2 and E3 were extruded at 90-100°C. Filaments extruded were more flexible when compared to PLA. Unlike PLA, to maintain the filament diameter of 1.75 mm, manual regulation of temperatures between 90°C to100°C were needed.

5.3.2 Optimizing 3D Printing Parameters

These extruded filaments were used in MakerBot 1st generation desktop 3D printer to print constructs. All E1, E2 and E3 constructs were printed at 110°C at a printer-head speed of 10 mm/s. A constant filament-feed rate of 23 mm/s was maintained throughout the printing process.

5.3.3 Scaffold Design and Fabrication

All 3D models such as IUDs and pessaries were designed using Solidworks 2015 CAD designing software. Discs of 5 x 1 mm dimensions were printed for drug elution testing and *in vitro* cell cultures. IUDs and pessaries of different dimensions and shapes were also printed using the extruded filaments.

5.4 Scaffold Characterization

The 3D printed hormonal scaffolds were subjected to physical and bioactive testing. Surface morphology of the constructs were studied using SEM, ELISA kits were used to study hormonal release from scaffolds and Luciferase assay was conducted to test the bioactivity of the hormonal discs.

5.4.1 Morphology

Extruded filaments and printed discs of different hormones were subjected to SEM using S4800 Field Emission SEM, HITACHI (Schaumburg, IL) at different magnifications. The surfaces of the constructs were nano-coated with the gold particles before imaging to make them conductive.

5.4.2 Hormone Elution Profiles

To calculate the amount of hormone eluting from the constructs, an elution study was conducted. Saline was used for sample collection. Samples from E2 and E3 were collected at periodic intervals for a week. These collected samples were analyzed using respective ELISA kits. From the pilot studies we could determine that the concentration of E2 eluting from the scaffolds was over the maximum detection level and all the reading were near saturation. A ten-fold dilution of the E2 samples and ELISA was performed. E3 samples had absorbance values within the ELISA detection range and were not diluted. The SpectraMax M2e multimode microplate reader was used to read the 96 well plates absorbance values. From the absorbance values of standards, the four parameter logistic (4PL) nonlinear regression model was drawn and concentrations of unknown samples were back calculated. For all the assays, the absorbance values at 405 nm were measured and recorded. The manufacturer's protocol followed for this assay is mentioned in **Appendix B**.

5.4.3 Estrogen Receptor Luciferase Cell Culture

This study was conducted to test the hormonal activity in the 3D printed scaffolds. Plain PCL pellets, saline and different concentrations of E2 were used as controls. Extruded filaments and 3D printed discs were used as unknowns. Before these scaffolds

were seeded, 90% confluent cells were detached from the culture tubes and suspended into RPMI medium. Each well was filled with 10 µl of suspension and incubated for 24 hours for attachment. Scaffolds were added to these wells and incubated for another 16 hours. Lysis buffer was added to each well and incubated for two minutes. In a new 96 well plate, 20 µl of this lysate was transferred and 100 µl of luciferase substrate is added. Optical density of each well is immediately read using a luminometer. The manufacturer's protocol followed for this assay is described in **Appendix B**.

5.5 Statistical Analysis

For the ELISA assay, three samples of each batch was tested and averaged for reproducibility. Standard deviation of the means was calculated and mentioned in the elution profile graphs as error bars. For the *in-vitro* study, measurements from five wells of each group were averaged. A one-way ANOVA was conducted to analyze the significant difference between the means among the groups. The standard deviation of the mean was calculated and represented as error bars in the graphs.

5.6 Results and Discussion

PCL pellets were successfully coated with E1, E2 and E3 hormones. Each 20 gm batches of 1.75 mm diameter filaments were extruded and required constructs were successfully printed. **Figure 5-4** shows images of PCL constructs printed with and without hormones using Makerbot 3D printer. Constructs containing a combination of hormones can be printed using this technique. **Figure 5-4** D shows a donut shaped pessary printed with unloaded PLA filament (red) and with PCL filament loaded with E2 hormone.

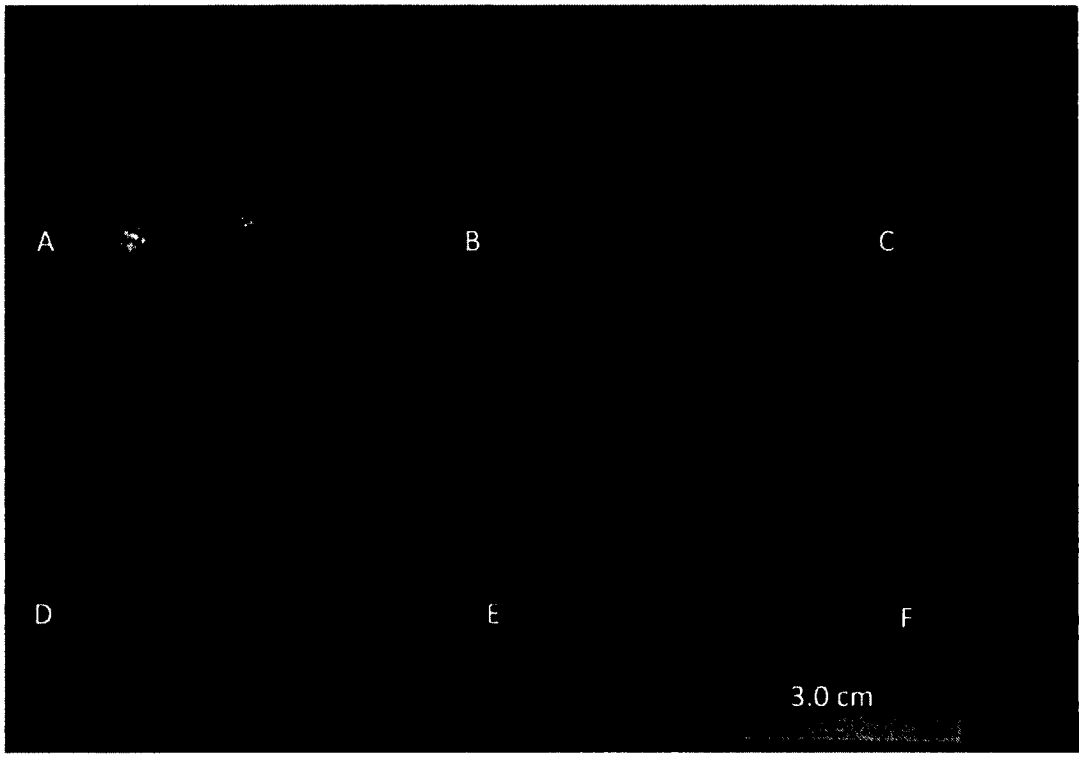

Figure 5-4: 3D printed constructs A) Control donut shaped pessary, B) Control gellhorn shaped pessary, C) Control IUD, D) Pessary printed combinations of filaments (red- PLA and white- PCL-E2), E) PCL-E1 IUD, and F) PCL-E2 IUD.

5.6.1 Scanning Electron Microscopy (SEM)

SEM was used to study the surface morphology of the coated pellets, filaments and printed discs. **Figure 5-5** shows the images of estrogen hormones E1, E2, and E3.

Figure 5-5: SEM images of A) E1, B) E2, C) E3.

All these hormones contain irregular shaped particles of varied sizes. The estimated largest size of these particles was around 5 μm. Filaments extruded from ExtrusionBot were cylindrical in shape and had a smooth external surface. The image in **Figure 5-6** show hormone loaded PCL filaments extruded using ExtrusionBot filament extruder.

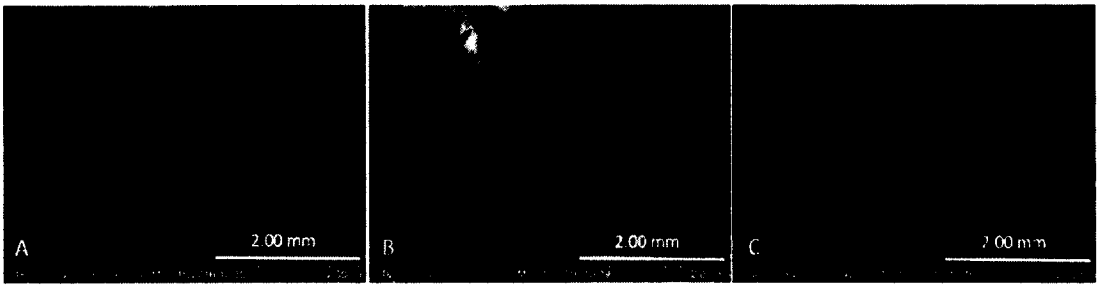

Figure 5-6: SEM images of A) E1, B) E2, C) E3.

These filaments were used in Makerbot 3D printer to print discs of 5 mm × 1 mm dimensions. Images in **Figure 5-7** A-C shows 3D printed discs used for ELISA and cell culture. On further magnification, hormone particles were seen on the surfaces of these discs. Images in **Figure 5-7** D, E and F shows E1, E2, and E3 particles on the surfaces of the discs at 100X magnification.

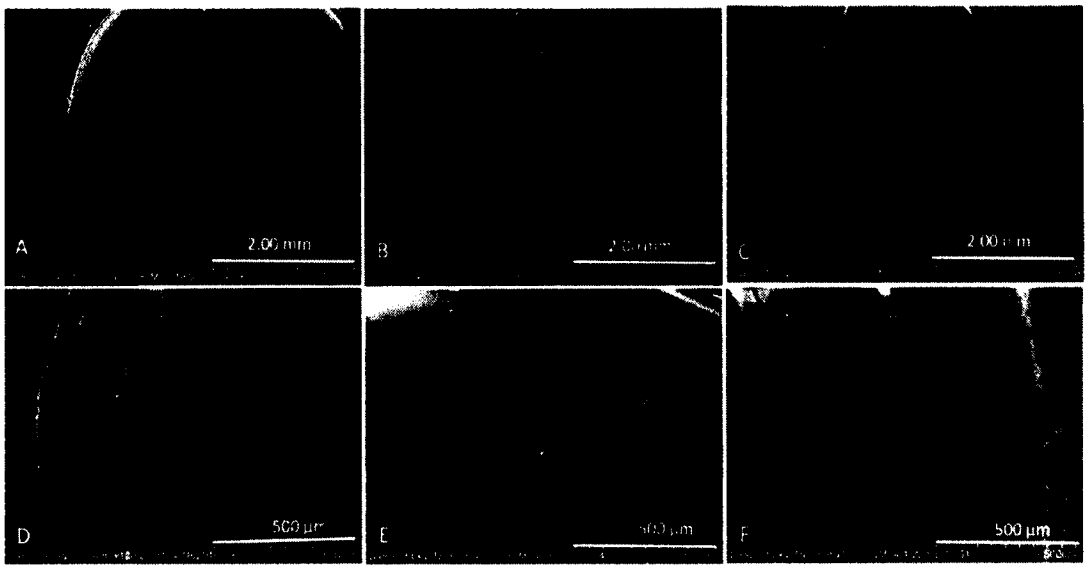

Figure 5-7: SEM images of (A,D) PCL-E1 Disc, (B,E) PCL-E2 Disc, (C,F) PCL-E3 Disc.

5.6.2 Quantification through ELISA

Preliminary studies showed the release of hormones were in nanograms concentration. A ten-fold dilution of the samples were done to meet the ELISA kits detection range. Samples were collected, one for each day. To calculate the concentrations of E2 and E3 released from the constructs, standard graphs shown in **Figure A-5** and **Figure A-6** of the Appendix A were used, respectively. **Table 5-1** shows the concentration of hormone E2 released from 3D printed PCL-E2 discs at a given time period. For the first two days, 35% of total hormone was released from the scaffolds. The release of the hormones from the 3D printed constructs can be regulated by altering infill ratio. Using dual head 3D printer, layers of the constructs can be printed in alternating hormone loaded and unloaded pattern.

Table 5-1: Concentration of E2 hormone released from PCL-E2 discs for individual days. (mean ± SD, n = 3)

Time (Day)	Concentration (ng/ml)
1	30.0
2	57.3
3	34.3
4	32.5
5	27.2
6	21.5
7	12.8

The graph in **Figure 5-8** shows the concentration of hormone E2 released over a period of one week. A total of 215 ng/ml of cumulative concentration of E2 hormone was released at the end of day seven. Even after seven days, small quantities of hormone release within the working concentration (2 ng/ml -5 ng/ml) were measured.

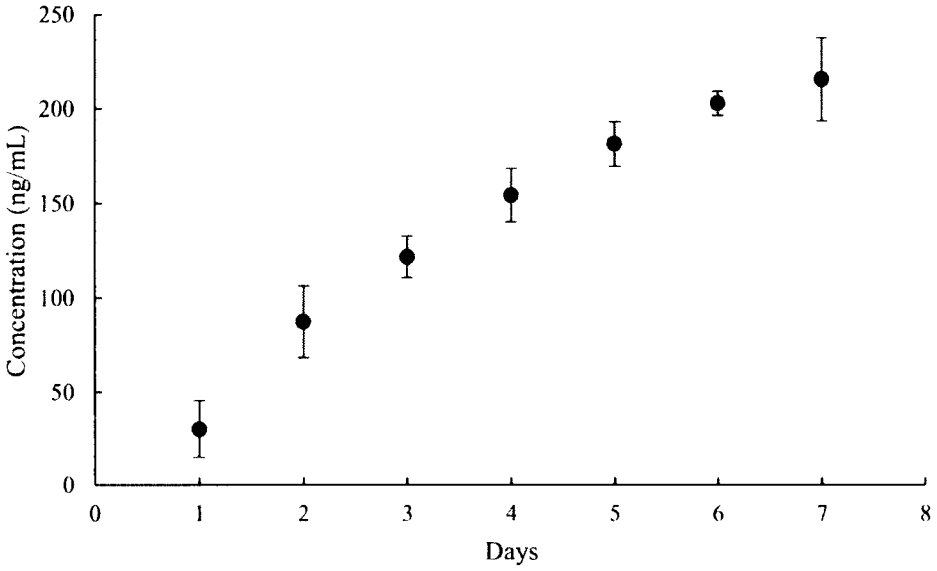

Figure 5-8: Cumulative concentration of E2 released from PCL-E2 discs (mean ± SD, n = 3).

The resolution of the 3D printed constructs can be changed by altering the layer height of the filament deposited. With decrease in layer height of the filament, surface area of the construct increases and in turn increases the hormonal release. All the hormone loaded discs were 3D printed at 300 μm resolution. **Table 5-2** shows the concentration of hormone E3 released per day from 3D printed discs. Preliminary tests showed the release of E3 hormones from the constructs were within the detectable range of the ELISA kits. So no further dilution of these samples were done. For the first two days, 46% of total hormone was released from the scaffolds. On day seven, 1.3 ng/ml hormone was released.

Table 5-2: Concentration of E3 hormone released from PCL-E3 discs for individual days.

Time (Day)	Concentration (ng/ml)
1	22.7
2	55.1
3	24.1
4	16.1
5	6.5
6	7.6
7	1.3

Figure 5-9 shows the cumulative concentration of E3 released from PCL scaffolds for a period of seven days. All samples were tested in multiples of three. Error bars in the graph are standard deviations. A standard graph plotted from the known concentration was used to yield four parameter logistic curve as shown in **Figure A-6**. E3 release increased during the first four days, after which hormonal elution was steady and extended. A total of 118 ng/ml (cumulative concentration) of E3 hormone was released by the end of day four. After that, only 5 ng/ml and 10 ng/ml per day was released.

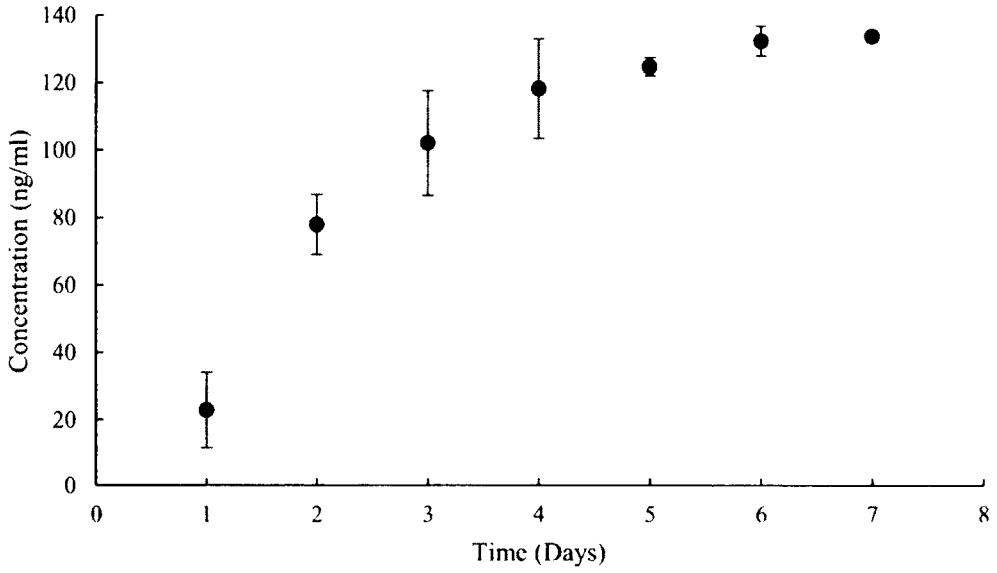

Figure 5-9: Cumulative concentration of E3 released from PCL-E3 discs (mean ± SD, n = 3).

5.6.3 *In vitro* Assay

Figure 5-10 shows the Relative Light Unit (RLU) values of luciferase activity in response to estrogen stimuli. Five wells of each group were tested and ANOVA analysis was conducted. The difference between the control cells and control PCL pellets was not statistically significant, indicating that the PCL pellets are biocompatible and do not promote any estrogen induced pathways. The group containing E2 showed a robust increase in RLU values when compared to groups without inducing agent, indicating the presence of bioactive compounds in the fabricated constructs. Wells containing 100 pg/ml concentration of E2 showed a total of 84.6% more luciferase activity. Luciferase activity for extruded filaments (1 cm length) and 3D printed discs (5 mm X 1mm) increased by 80.85% and 74.9%, respectively, when compared to the control cells activity.

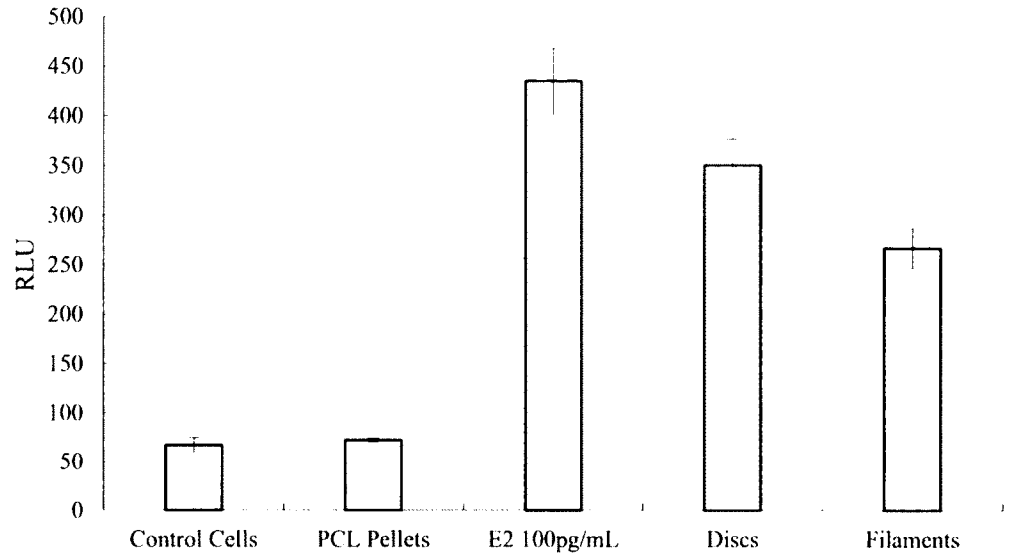

Figure 5-10: RLU values of Estrogen receptor luciferase reporter cells incubated with different groups of E2 scaffolds (mean ± SD, n = 5).

5.7 Conclusions

Fused deposition modeling was used for the first time to fabricate hormone loaded biodegradable implant materials. Female sex hormones (E1, E2, and E3) were coated on to PCL pellets and filaments of required dimensions were successfully extruded. With these bioactive enhanced filaments, constructs of required shapes such as IUD, different sizes and shapes of pessaries were 3D printed using MakerBot 3D printer.

SEM images showed extruded filaments were smooth and cylindrical in nature. The study of release kinetics using ELISA assay showed that the hormones E2 and E3 were released at a steady rate from the scaffolds over an extended period.

In vitro assays conducted on estrogen receptor luciferase reporter cell lines show that scaffolds fabricated were biocompatible. Groups enhanced with hormones showed robust luciferase activity, indicating the presence of bioactive inducing substance (E2) in the scaffolds.

The ability to 3D print estrogen-loaded biodegradable implants holds huge potential in personalized medicine. Using these methods, IUDs and pessaries can be tailored to a patient's specific needs in aspects of the unique anatomy of the individual, hormone dosage and period of hormone therapy.

CHAPTER 6

CONCLUSIONS AND FUTURE WORK

6.1 Conclusions

Novel CPCs enhanced with doped HNTs were successfully formulated and evaluated. The addition of HNTs up to 5%wt increased the compressive and flexural strengths of the scaffolds. A further increase in the concentration of HNTs did not yield higher mechanical strength statistically. SEM showed an increase in surface roughness upon addition of HNTs to the CPC composition. Drug-loaded HNTs added in the CPC scaffolds showed an initial outburst of the bioactive compounds and then an extended release up to a week. CPC discs loaded with different concentrations of HNTs showed clear demarcating zone of inhibitions for *E.coli* and *P. aureus*.

This study demonstrated the novel methods to fabricate 3D constructs with bioactive properties using a desktop 3D printer. Filaments of required bioactive agent (antibiotic, chemotherapeutic or hormone) were successfully prepared using ExtrusionBot filament extruder. This work highlights the advantages and difficulties associated with this novel fabricating technique. SEM was used to characterize the morphology of the extruded filament and 3D printed scaffolds. Traces of bioactive materials were observed on the surface of the scaffolds via SEM. Scaffolds with different mechanical strengths were constructed using different infill ratios. Compression and

flexural strengths increased with an increased infill ratio. Drug release profiles from the 3D printed PLA and PCL scaffolds showed initial outburst and then extended steady release for a week. XTT assays on a human osteoblast cell line confirmed biocompatibility of these fabricated constructs.

E.coli bacterial cultures demonstrated the anti-infective properties of the GS loaded PLA scaffolds. XTT assay conducted on osteosarcoma cell lines confirmed chemotherapeutic ability of MTX loaded PLA constructs. Similarly, luciferase assay conducted on estrogen receptor luciferase reporter cell line showed estrogen hormone activity among E2 loaded PCL scaffolds.

Antibiotic- and chemotherapeutic-loaded beads and catheters were successfully printed, and their bioactivity on bacterial and osteosarcoma cell cultures, respectively, was confirmed. IUDs and Pessaries of different shapes and dimensions were printed using estrogen loaded PCL filaments.

Critical defects were made on a cow's femur bone using standard drilling machine. Defects were 3D scanned, processed and 3D printed successfully using custom extruded drug loaded filaments. Additionally, this study demonstrated strategies for adopting 3D printing technology to fabricate scaffolds for tissue regeneration. The 3D printed constructs were optimized and used as supporting materials to generate live vascular prostheses. The dimensions of these vessels can be customized in terms of its length, diameter and wall thickness by varying dimensions of the scaffolds. The same technique can be used to fabricate complex or branched vascular grafts.

6.2 Future Work

Novel 3D printing machines using additive manufacturing techniques allows the design of the patient's specific prosthetic implants to suit individual anatomy, improve functionality and reduce implant failures. However, much work and research remains to be accomplished. Among a large variety of biopolymers, only PLA and PCL were used in this study. This study can be conducted using other biodegradable polymers such as PLG (poly glycolides) and PLGA (poly (lactic-co-glycolic acid)). Additionally, *in vivo* animal studies can be done. The following are some of the ongoing projects on 3D printing.

6.2.1 Surgical Mesh

Surgical mesh is a medical device used to provide mechanical support to damaged or weakened tissues. These devices are used in procedures such as pelvic organ prolapse, inguinal hernia, and others. These devices are intended to stay at the site, provide support to the tissues and gradually degrade allowing the formation of neotissue at the site.

Depending upon the place of the implantation, various meshes with different weights, filament size, pore size and weaving structures are used. A 3D printer can be used to print biodegradable, and biocompatible meshes can be printed with customizable parameters and inculcating bioactive nature. **Figure 6-1** shows the 3D printed PLA meshes and zone of inhibition of *E.coli* by 1% wt GS-PLA mesh.

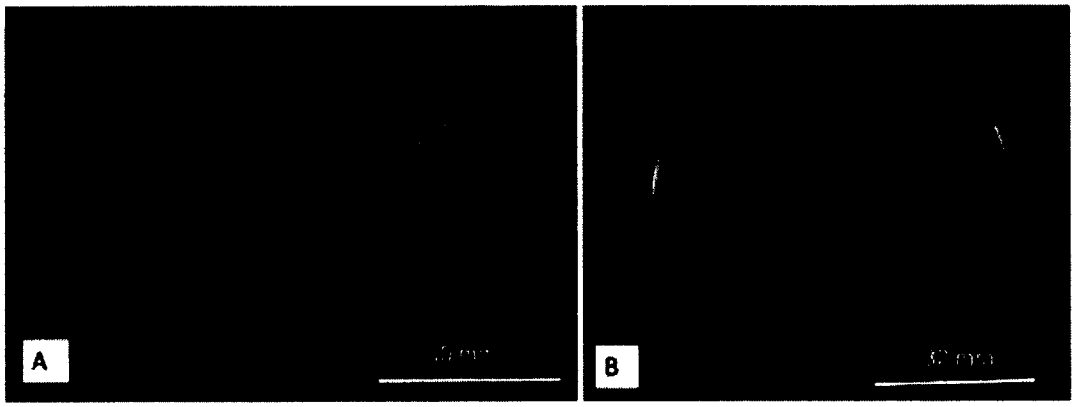

Figure 6-1: A) 3D printed Plain PLA surgical mesh, B) zone of inhibition of 1%wt GS-PLA on *E. coli* bacterial plate.

6.2.2 Live Vascular Grafts

Vascular prosthesis or grafts are medical devices used to replace or bypass damaged or diseased blood vessels. Biological grafts do not cause immunological responses and are preferred over synthetic prosthesis. 3D printing can be used to fabricate vascular scaffolds with a wide variety of shapes and dimensions. Treating these scaffolds chemically can make their surface suitable for cell attachment and growth. **Figure 6-2** shows the process of fabricating a live vascular graft.

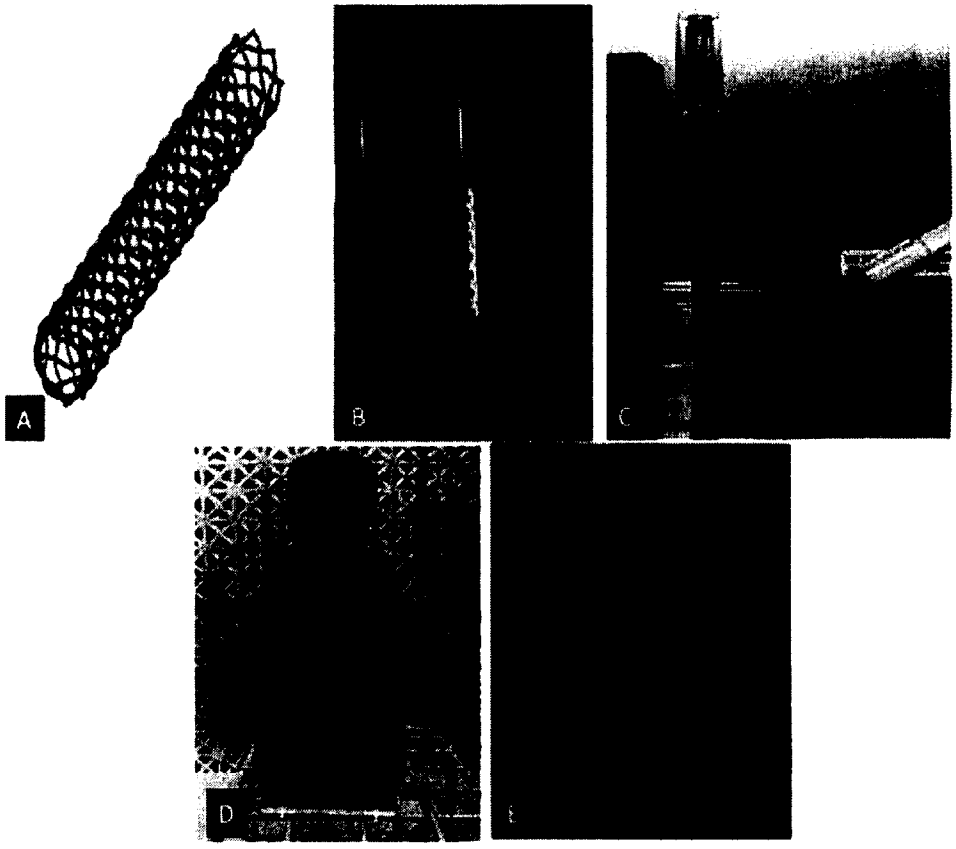

Figure 6-2: A) CAD model of vascular stent, B) 3D printed stent using PVA, C) Seeding cells on to the scaffold, D-E) Cells growing on the stent.

Scaffolds for vascular grafts were 3D printed from a PVA thermoplastic. These scaffolds were sterilized, and the surfaces were chemically treated for cell attachment. Placental stem cells in a collagen matrix were seeded on to the scaffolds and incubated in a cell culture medium. Images in **Figure 6-2** D) and E) show the stem cell layer growing around the vascular scaffold.

APPENDIX A

STANDARD GRAPHS FOR DRUG ELUTION PROFILES

Standard Graphs for GS and NS Used in CPC Evaluation

Figure A-1 shows the standard graph plotted with absorbance values of known concentration of GS. From the graph linear equation was derived and all the unknown concentration of the samples are back calculated from their absorbance values. Similarly, **Figure A-2** was used to calculate unknown values NS from CPC-NS.

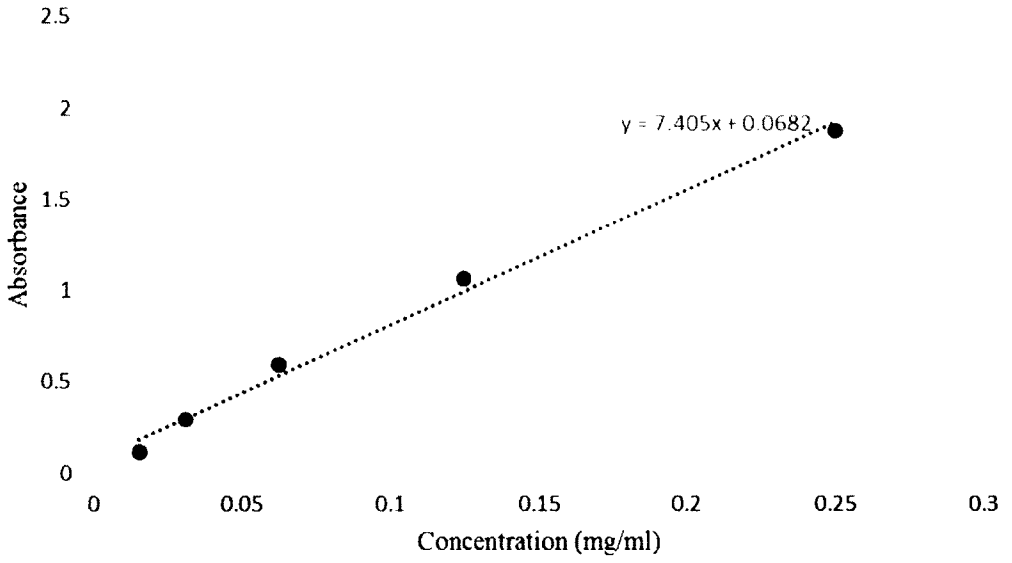

Figure A-1: Standard graph used for calculating GS concentration for CPC samples.

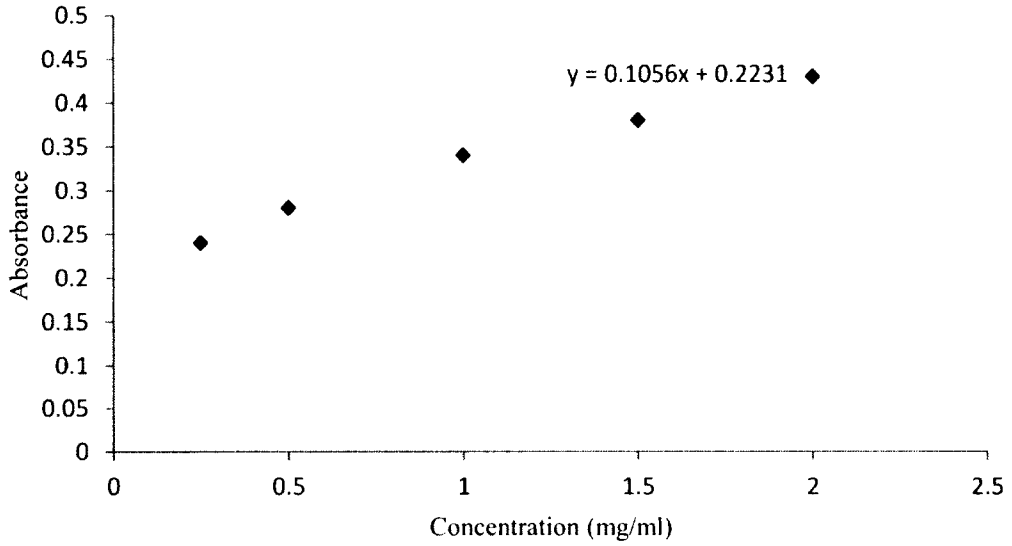

Figure A-2: Standard graph used for calculating NS concentration for CPC samples.

Standard Graphs for GS and MTX Used in PLA Evaluation

The graph in **Figure A-3** was plotted with known values of GS concentrations against their absorbance values. Best fit equation was derived from it and unknown concentrations are back-calculated using the equation.

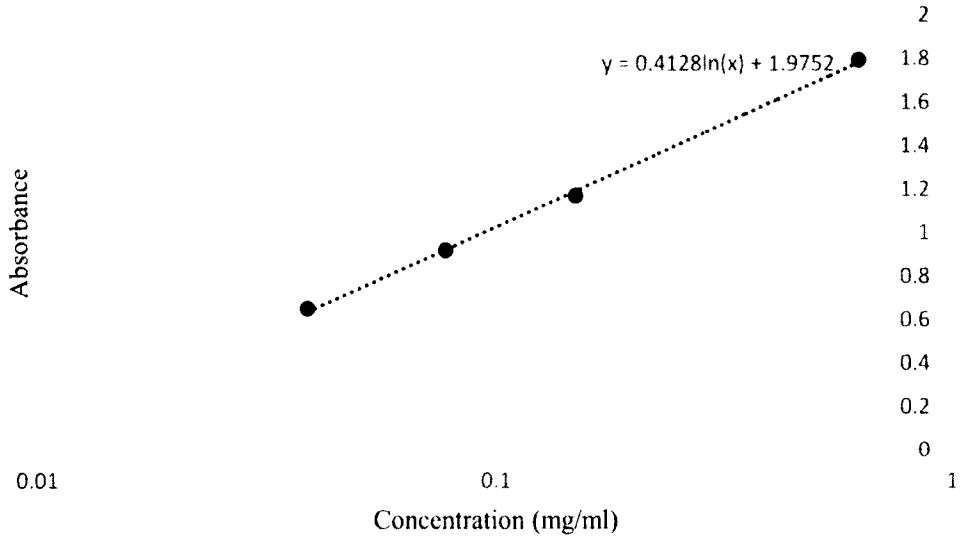

Figure A-3: Standard graph used for calculating GS concentration from 3D printed constructs.

Similarly, **Figure A-4** was used to calculate the best fit equation from the absorbance values. With this equation, the unknown concentrations were back calculated.

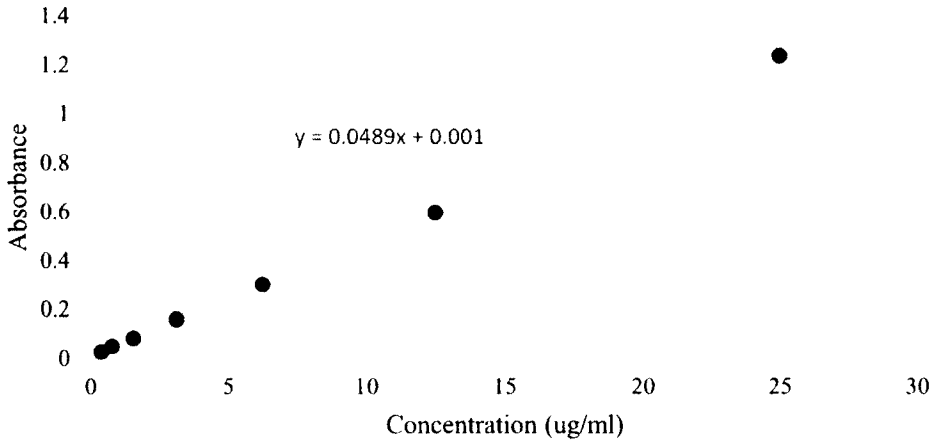

Figure A-4: Standard graph used for calculating MTX concentration from PLA-MTX.

Standard Graphs for E2 and E3 ELISA

Graphs in **Figure A-5** and **Figure A-6** are standard graphs used to calculate the unknown concentrations of hormones E2 and E3 respectively. These graphs were generated using softmax-pro software of micro-plate reader.

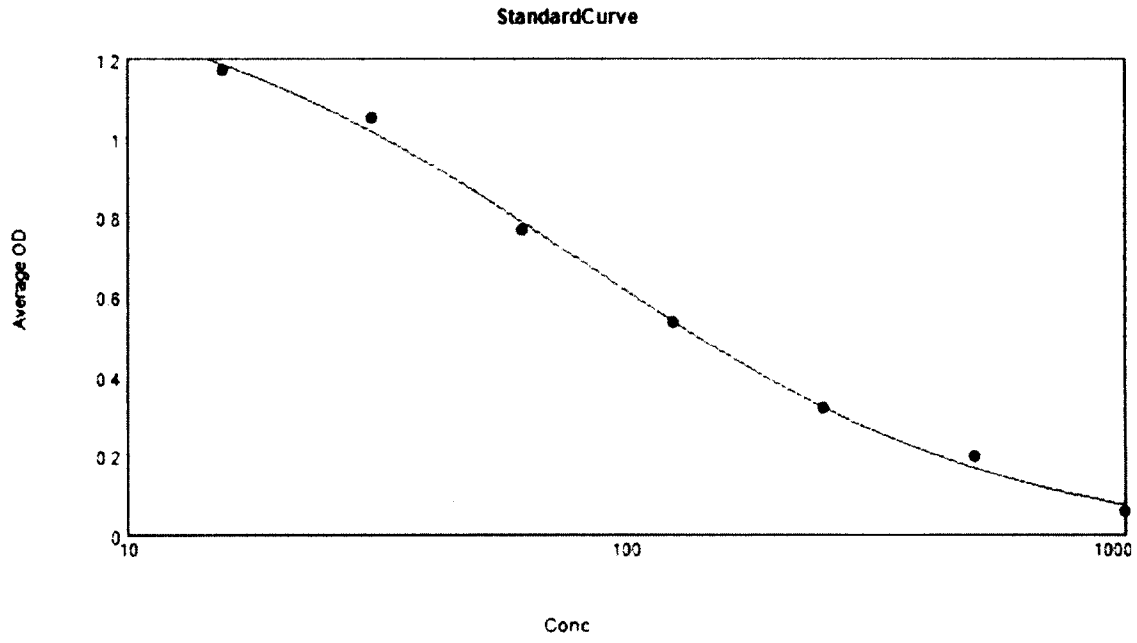

● STD#1 (Standards@ELISA_AP&pNPP AvgOD vs Conc) Weighting: Fixed

Curve Fit Results ▲

Curve Fit : 4-Parameter $y = D + \frac{A - D}{1 + \left(\frac{x}{C}\right)^B}$

	Parameter	Estimated Value	Std. Error	Confidence Interval
STD#1 R^2 = 0.997	A	1.412	0.145	[0.951, 1.873]
EC50 = 81.98	B	1.007	0.218	[0.313, 1.701]
	C	81.98	14.52	[35.76, 128.2]
	D	-0.032	0.082	[-0.293, 0.228]

Figure A-5: Standard graph used for calculating E2 concentration from PCL-E2 Discs.

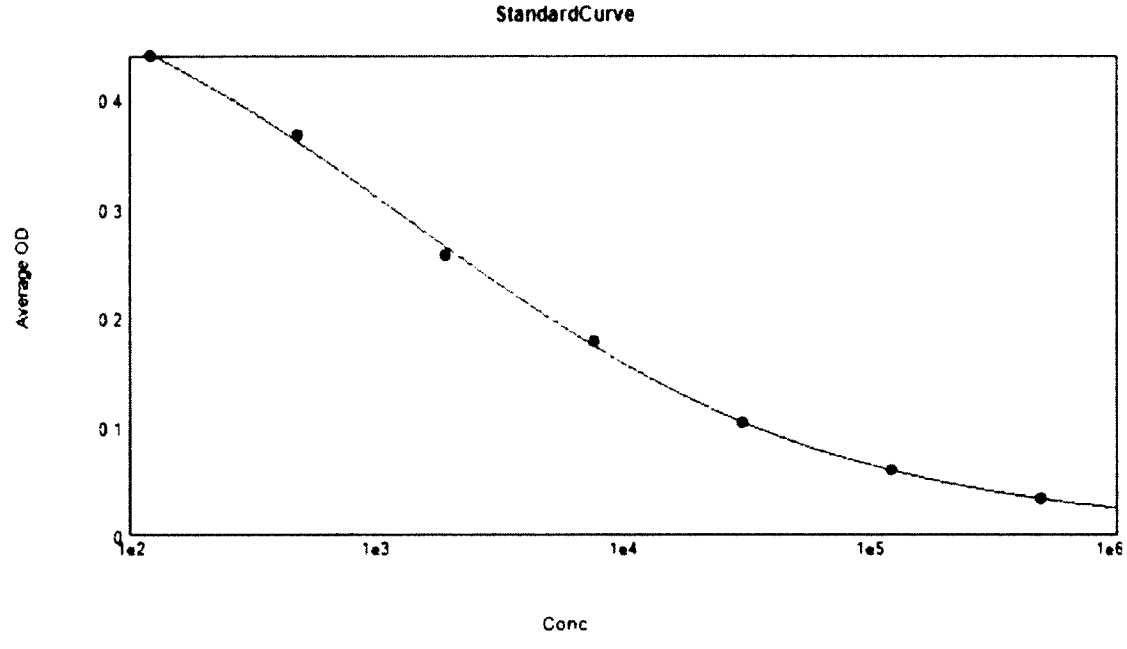

● STD#1 (Standards@ELISA_AP&pNPP: AvgOD vs Conc) Weighting: Fixed

Curve Fit Results ▲

Curve Fit : 4-Parameter $y = D + \frac{A - D}{1 + \left(\frac{x}{C}\right)^B}$

	Parameter	Estimated Value	Std. Error	Confidence Interval
STD#1				
R^2 = 0.999	A	0.573	0.043	[0.436, 0.709]
EC50 = 1399	B	0.494	0.058	[0.308, 0.680]
	C	1399	400.7	[123.4, 2674]
	D	0.003	0.013	[-0.040, 0.045]

Figure A-6: Standard graph used for calculating E3 concentration from PCL-E3 discs.

APPENDIX B

PROTOCOLS FOR CELL CULTURE TECHNIQUES

XTT Assay Protocol for Osteoblast and Osteosarcoma Cells

A 96 well plate was used for this assay. Five wells were set as blank with just medium and without cells. This assay was performed on Days 3,7 and 14.

- Well plates were taken out of the incubator and aspirated completely.
- Each well was added with 80 µl of PBS and 20 µl of XTT stock solution.
- These plates were incubated for 2 hours.
- Absorbance values from wells were read at 450 nm using multiplate reader.

ELISA Protocol for E2 and E3 Hormones

All reagents required for the assay such as assay buffer, E2 standards and conjugates were supplied by the manufacturer and were prepared according to the manufacturers protocol.

- Non-specific binding (NSB) wells were filled with 150 µl of assay buffer and 100 µl of assay buffer into the remaining wells.
- Each 100 µl of standard known concentrations of the samples were added into the specified wells.
- All wells, except for blank wells, were added with 50 µl of blue conjugate.

- Immediately, all wells except for blanks and NSB wells, were added with 50 µl of yellow antibody.
- This plate was sealed and kept on a rocker for two hours at 500 rpm.
- All the contents of the wells were emptied and washed 3-4 times using wash buffer.
- All wells were then added with 200 µl of substrate solution.
- These plate was then incubated for one hour without shaking.
- All wells were then added with 50 µl of stop solution.
- Optical densities of the wells were read immediately at 405 nm.

Luciferase Assay Protocol for Estrogen Receptor Cells

Estrogen receptor luciferase reporter T47D stable cell line was used to perform the luciferase assay. As soon as cells were shipped, entire contents of the vial were thawed and transferred into a culture dish using RPMI medium. On 90% confluent growth, cells were split and used for assay.

- The cells were seeded on a 96 well plate for overnight with DMEM medium containing 10% FBS and incubated.
- Inducing agents or test samples were added to each well directly and incubated for 16 hours.
- Media was aspirated and 100 µl of PBS was added to each well.
- After 5 minutes, media was aspirated again and 50 µl of lysis buffer was added to each well.
- Cells were incubated in lysis buffer for 20 minutes at room temperature.

- To ensure complete lysis of the cells, plate was rock cultured for 5 minutes at 500 rpm.
- One freeze-thaw cycle at -80°C and room temperature was performed to ensure complete lysis of the cells.
- A new 96 well plate was taken and 20 µl of lysate is transferred from each well.
- To this new plate, 100 µl of luciferase substrate was added and gently pipetted up and down for thorough mixing.
- Plate was read under luminometer immediately.

BIBLIOGRAPHY

[1] S. C. Tjong, *Synthesis and Properties of Nano-Hydroxyapatite/ Polymer Nanocomposites for Bone Tissue Engineering*. Bentham Science Publishers, 2012.

[2] "http://www.surgeryencyclopedia.com/A-Ce/Bone-Grafting.html."

[3] C. J. Damien and J. R. Parsons, "Bone graft and bone graft substitutes: a review of current technology and applications," *J. Appl. Biomater.*, vol. 2, no. 3, pp. 187–208, Jan. 1991.

[4] J. P. Schmitz, J. O. Hollinger, and S. B. Milam, "Reconstruction of bone using calcium phosphate bone cements: a critical review," *J. oral Maxillofac. Surg.*, vol. 57, no. 9, pp. 1122–6, Sep. 1999.

[5] A. R. Amini, J. S. Wallace, and S. P. Nukavarapu, "Short-term and long-term effects of orthopedic biodegradable implants.," *J. Long. Term. Eff. Med. Implants*, vol. 21, no. 2, pp. 93–122, Jan. 2011.

[6] J. C. Middleton and A. J. Tipton, "Synthetic biodegradable polymers as orthopedic devices.," *Biomaterials*, vol. 21, no. 23, pp. 2335–46, Dec. 2000.

[7] D. Campoccia, L. Montanaro, and C. R. Arciola, "The significance of infection related to orthopedic devices and issues of antibiotic resistance," *Biomaterials*, vol. 27, no. 11. pp. 2331–2339, 2006.

[8] L. Rimondini, M. Fini, and R. Giardino, "The microbial infection of biomaterials: A challenge for clinicians and researchers. A short review," *J. Appl. Biomater. Biomech.*, vol. 3, no. 1, pp. 1–10, 2005.

[9] A. Bistolfi, G. Massazza, E. Verné, A. Massè, D. Deledda, S. Ferraris, M. Miola, F. Galetto, and M. Crova, "Antibiotic-loaded cement in orthopedic surgery: A review," *ISRN Orthop.*, vol. 2011, pp. 1–8, 2011.

[10] C. P. Scott, P. A. Higham, and J. H. Dumbleton, "Effectiveness of bone cement containing tobramycin. An *in vitro* susceptibility study of 99 organisms found in infected joint arthroplasty.," *J. Bone Joint Surg. Br.*, vol. 81, no. 3, pp. 440–443, 1999.

[11] F. D. Matl, A. Obermeier, S. Repmann, W. Friess, A. Stemberger, and K.-D. Kuehn, "New anti-infective coatings of medical implants," *Antimicrob. Agents Chemother.*, vol. 52, no. 6, pp. 1957–63, Jun. 2008.

[12] S. Gitelis and G. Brebach, "The treatment of chronic osteomyelitis with a biodegradable antibiotic-impregnated implant," *J Orthop Surg (Hong Kong)*, vol. 10, no. 1, pp. 53–60, 2002.

[13] M. Mohamed, G. Borchard, and O. Jordan, "In situ forming implants for local chemotherapy and hyperthermia of bone tumors," *Journal of Drug Delivery Science and Technology*, vol. 22, no. 5. pp. 393–408, 2012.

[14] E. P. Lautenschlager, J. J. Jacobs, G. W. Marshall, and P. R. Meyer, "Mechanical properties of bone cements containing large doses of antibiotic powders," *J. Biomed. Mater. Res.*, vol. 10, no. 6, pp. 929–38, Nov. 1976.

[15] A. H. Gomoll, W. Fitz, R. D. Scott, T. S. Thornhill, and A. Bellare, "Nanoparticulate fillers improve the mechanical strength of bone cement," *Acta Orthop.*, vol. 79, no. 3, pp. 421–7, Jun. 2008.

[16] M. M. Stevens, "Biomaterials for bone tissue engineering," *Mater. Today*, vol. 11, no. 5, pp. 18–25, May 2008.

[17] P. Fratzl, "Hierarchical structure and mechanical adaptation of biological materials," *Leture notes NATO-Advanced Study Inst. "Learining from Nat. how to Des. new Implant. Biomater.*, vol. 1, pp. 15–34, 2004.

[18] P. Downey and M. I. Siegel, "Bone biology and the clinical implications for osteoporosis," *Phys. Ther.*, vol. 86, no. 1, pp. 77–91, Jan. 2006.

[19] I. H. Kalfas, "Principles of bone healing," *Neurosurg. Focus*, vol. 10, no. 4, pp. 7–10, Jan. 2001.

[20] M. Hahn, M. Vogel, M. Pompesius-Kempa, and G. Delling, "Trabecular bone pattern factor—a new parameter for simple quantification of bone microarchitecture," *Bone*, vol. 13, no. 4, pp. 327–330, Jul. 1992.

[21] C. Sfeir and L. Ho, "Fracture repair," in *Bone regeneration and repair*, J. R. Lieberman and G. E. Friedlaender, Eds. Totowa, NJ: Humana Press, 2005, pp. 21–44.

[22] D. W. Sommerfeldt and C. T. Rubin, "Biology of bone and how it orchestrates the form and function of the skeleton," *Eur. spine J.*, vol. 10, pp. S86–95, Oct. 2001.

[23] A. P. Pohl, "Mechanical manipulation of fractures to enhance fracture healing," *J. Bone Jt. Surg.*, vol. 84-B, no. SUPP III, pp. 213–214, Nov. 2002.

[24] C. T. Rubin and L. E. Lanyon, "Regulation of bone formation by applied dynamic loads," *J. Bone Joint Surg. Am.*, vol. 66, no. 3, pp. 397–402, Mar. 1984.

[25] M. M. Beloti and A. L. Rosa, "Osteoblast differentiation of human bone marrow cells under continuous and discontinuous treatment with dexamethasone," *Braz. Dent. J.*, vol. 16, no. 2, pp. 156–61, Jan. 2005.

[26] D. S. Geller and R. Gorlick, "Osteosarcoma: a review of diagnosis, management, and treatment strategies.," *Clin. Adv. Hematol. Oncol.*, vol. 8, no. 10, pp. 705–18, 2010.

[27] J. Gill, M. K. Ahluwalia, D. Geller, and R. Gorlick, "New targets and approaches in osteosarcoma," *Pharmacol. Ther.*, vol. 137, no. 1, pp. 89–99, 2013.

[28] G. Ottaviani and N. Jaffe, "The epidemiology of osteosarcoma," in *Cancer Treatment and Research*, 2009, vol. 152, pp. 3–13.

[29] J. Majó, R. Cubedo, and N. Pardo, "Treatment of Osteosarcoma. A Review," *Rev. Española Cirugía Ortopédica y Traumatol. (English Ed.*, vol. 54, no. 5, pp. 329–336, 2010.

[30] A. Luetke, P. A. Meyers, I. Lewis, and H. Juergens, "Osteosarcoma treatment - Where do we stand? A state of the art review," *Cancer Treat. Rev.*, vol. 40, no. 4, pp. 523–532, 2014.

[31] D. Carrle and S. S. Bielack, "Current strategies of chemotherapy in osteosarcoma," *International Orthopaedics*, vol. 30, no. 6. pp. 445–451, 2006.

[32] S. Smeland, O. S. Bruland, L. Hjorth, O. Brosjö, B. Bjerkehagen, G. Osterlundh, A. Jakobson, K. S. Hall, O. R. Monge, O. Björk, and T. A. Alvegaard, "Results of the Scandinavian Sarcoma Group XIV protocol for classical osteosarcoma: 63 patients with a minimum follow-up of 4 years.," *Acta Orthop.*, vol. 82, no. 2, pp. 211–6, 2011.

[33] B. Kempf-Bielack, S. S. Bielack, H. Jürgens, D. Branscheid, W. E. Berdel, G. U. Exner, U. Göbel, K. Helmke, G. Jundt, H. Kabisch, M. Kevric, T. Klingebiel, R. Kotz, R. Maas, R. Schwarz, M. Semik, J. Treuner, A. Zoubek, and K. Winkler, "Osteosarcoma relapse after combined modality therapy: An analysis of unselected patients in the Cooperative Osteosarcoma Study Group (COSS)," *J. Clin. Oncol.*, vol. 23, no. 3, pp. 559–568, 2005.

[34] G. Maccauro, A. Cittadini, M. Casarci, F. Muratori, D. De Angelis, C. Piconi, M. A. Rosa, A. Spadoni, M. Braden, and A. Sgambato, "Methotrexate-added acrylic cement: Biological and physical properties," *J. Mater. Sci. Mater. Med.*, vol. 18, no. 5, pp. 839–844, 2007.

[35] B. J. Lindbloom, E. R. James, and W. C. McGarvey, *Osteomyelitis of the Foot and Ankle*, vol. 19, no. 3. 2014.

[36] E. J. Boyko, J. H. Ahroni, V. Stensel, R. C. Forsberg, D. R. Davignon, and D. G. Smith, "A prospective study of risk factors for diabetic foot ulcer. The Seattle Diabetic Foot Study.," *Diabetes Care*, vol. 22, no. 7, pp. 1036–1042, 1999.

[37] L. Grammatico-Guillon, S. Baron, S. Gettner, A.-I. Lecuyer, C. Gaborit, P. Rosset, E. Rusch, and L. Bernard, "Bone and joint infections in hospitalized patients in France, 2008: clinical and economic outcomes," *Journal of Hospital Infection*, vol. 82, no. 1. pp. 40–48, 2012.

[38] B. Lipsky, R. Berendt, H. Deery, M. Embil, S. Joseph, W. Karchmer, L. LeFrock, P. Lew, T. Mader, C. Norden, and S. Tan, "Diagnosis and Treatment of Diabetic Foot Infections," *Clin. Infect. Dis.*, vol. 39, pp. 885–910, 2004.

[39] N. Singh, D. G. Armstrong, and B. A. Lipsky, "Preventing foot ulcers in patients with diabetes," *JAMA*, vol. 293, no. 2, pp. 217–228, 2005.

[40] L. A. Lavery, D. G. Armstrong, R. P. Wunderlich, M. J. Mohler, C. S. Wendel, and B. A. Lipsky, "Risk Factors for Foot Infections in Individuals With Diabetes," *Diabetes Care*, vol. 29, no. 6, pp. 1288–1293, 2006.

[41] I. Uçkay, D. Pittet, P. Vaudaux, H. Sax, D. Lew, and F. Waldvogel, "Foreign body infections due to _Staphylococcus epidermidis_," *Ann.Med.*, vol. 41, no. 1365–2060 (Electronic), pp. 109–119, 2009.

[42] F. Waldvogel, G. Medoff, and M. N. Swartz, "Osteomyelitis: a review of clinical features, therapeutic considerations and unusual aspects," *N. Engl. J. Med.*, vol. 282, no. 4, pp. 198–206, 1970.

[43] D. R. Dirschl and L. C. Almekinders, "Osteomyelitis. Common causes and treatment recommendations," *Drugs*, vol. 45, no. 0012–6667 SB - IM, pp. 29–43, 1993.

[44] A. D. Tice, P. A. Hoaglund, and D. A. Shoultz, "Outcomes of osteomyelitis among patients treated with outpatient parenteral antimicrobial therapy," *Am. J. Med.*, vol. 114, no. 9, pp. 723–728, 2003.

[45] E. A. Melamed and E. Peled, "Antibiotic impregnated cement spacer for salvage of diabetic osteomyelitis," *Foot Ankle Int*, vol. 33, no. 3, pp. 213–219, 2012.

[46] P. Sambrook and C. Cooper, "Osteoporosis.," *Lancet (London, England)*, vol. 367, no. 9527, pp. 2010–8, 2006.

[47] N. von Wowern, "General and oral aspects of osteoporosis: a review.," *Clin. Oral Investig.*, vol. 5, pp. 71–82, 2001.

[48] V. Bandela, B. Munagapati, R. K. R. Karnati, G. R. S. Venkata, and S. R. Nidudhur, "Osteoporosis: Its Prosthodontic Considerations - A Review.," *J. Clin. Diagn. Res.*, vol. 9, no. 12, pp. ZE01–4, Dec. 2015.

[49] S. R. Cummings and L. J. Melton, "Osteoporosis I: Epidemiology and outcomes of osteoporotic fractures," *Lancet*, vol. 359, no. 9319. pp. 1761–1767, 2002.

[50] J. Klein-Nulend, R. F. M. van Oers, A. D. Bakker, and R. G. Bacabac, "Bone cell mechanosensitivity, estrogen deficiency, and osteoporosis," *J. Biomech.*, vol. 48, no. 5, pp. 855–865, 2015.

[51] D. Grady, S. M. Rubin, D. B. Petitti, C. S. Fox, D. Black, B. Ettinger, V. L. Ernster, and S. R. Cummings, "Hormone therapy to prevent disease and prolong life in postmenopausal women.," *Ann. Intern. Med.*, vol. 117, no. 12, pp. 1016–37, Dec. 1992.

[52] S. Ahmadzadeh-Asl, S. Hesaraki, and a Zamanian, "Preparation and characterisation of calcium phosphate-hyaluronic acid nanocomposite bone cement," *Adv. Appl. Ceram.*, vol. 110, no. 6, pp. 340–345, Aug. 2011.

[53] E. Puricelli, A. Corsetti, D. Ponzoni, G. L. Martins, M. G. Leite, and L. Santos, "Characterization of bone repair in rat femur after treatment with calcium phosphate cement and autogenous bone graft," *Head Face Med.*, vol. 6, p. 10, Jan. 2010.

[54] K. Padois and F. Rodriguez, "Effects of chitosan addition to self-setting bone cement," *Biomed. Mater. Eng.*, vol. 17, no. 5, pp. 309–20, Jan. 2007.

[55] V. S. Komlev, I. V. Fadeeva, N. Gurin, L. I. Shvorneva, N. V. Bakunova, and S. M. Barinov, "New calcium phosphate cements based on tricalcium phosphate," *Dokl. Chem.*, vol. 437, no. 1, pp. 75–78, Apr. 2011.

[56] R. A. Perez, H. Kim, and M.-P. Ginebra, "Polymeric additives to enhance the functional properties of calcium phosphate cements," *J. Tissue Eng.*, vol. 3, no. 1, pp. 1–20, Jan. 2012.

[57] F. C. M. Driessens, J. Planell, M. G. Boltong, I. Khairoun, and M. P. Ginebra, "Osteotransductive bone cements," *J. Eng. Med.*, vol. 212, no. 6, pp. 427–435, Jun. 1998.

[58] A. Bigi, B. Bracci, and S. Panzavolta, "Effect of added gelatin on the properties of calcium phosphate cement," *Biomaterials*, vol. 25, no. 14, pp. 2893–9, Jul. 2004.

[59] J. T. Zhang, F. Tancret, and J. M. Bouler, "Fabrication and mechanical properties of calcium phosphate cements (CPC) for bone substitution," *Mater. Sci. Eng.*, vol. 31, no. 4, pp. 740–747, May 2011.

[60] S. Perni, V. Thenault, P. Abdo, K. Margulis, S. Magdassi, and P. Prokopovich, "Antimicrobial activity of bone cements embedded with organic nanoparticles.," *Int. J. Nanomedicine*, vol. 10, pp. 6317–29, Jan. 2015.

[61] K. Balasubramanian and M. Burghard, "Biosensors based on carbon nanotubes," *Anal. Bioanal. Chem.*, vol. 385, no. 3, pp. 452–68, Jun. 2006.

[62] K. Balakumar, M. Rajkumar, and C. V. Raghavan, "Carbon nanotubes: A versatile technique for drug delivery," *Int. J. Nanomater. Biostructures*, vol. 2, no. 4, pp. 55–59, 2012.

[63] Y. Qu, Y. Yang, J. Li, Z. Chen, J. Li, K. Tang, and Y. Man, "Preliminary evaluation of a novel strong/osteoinductive calcium phosphate cement," *J. Biomater. Appl.*, vol. 26, no. 3, pp. 311–25, Sep. 2011.

[64] E. Abdullayev and Y. Lvov, "Halloysite clay nanotubes for controlled release of protective agents," *J. Nanosci. Nanotechnol.*, vol. 11, no. 11, pp. 10007–26, Nov. 2011.

[65] M. Du, B. Guo, and D. Jia, "Newly emerging applications of halloysite nanotubes: a review," *Polym. Int.*, vol. 59, no. 5, pp. 574–582, 2010.

[66] N. G. Veerabadran, R. R. Price, and Y. M. Lvov, "Clay nanotubes for encapsulation and sustained release of drugs," *Nano*, vol. 02, no. 02, pp. 115–120, Apr. 2007.

[67] R. Kamble, M. Ghag, S. Gaikawad, and B. K. Panda, "Review article halloysite nanotubes and applications : A review," *J. Adv. Sci. Res.*, vol. 3, no. 2, pp. 25–29, 2012.

[68] S. T. Newman, Z. Zhu, V. Dhokia, and A. Shokrani, "Process planning for additive and subtractive manufacturing technologies," *CIRP Ann. - Manuf. Technol.*, vol. 64, no. 1, pp. 467–470, 2015.

[69] N. Guo and M. C. Leu, "Additive manufacturing: Technology, applications and research needs," *Front. Mech. Eng.*, vol. 8, no. 3, pp. 215–243, 2013.

[70] B. Duan and M. Wang, "Selective laser sintering and its application in biomedical engineering," *MRS Bull.*, vol. 36, no. 12, pp. 998–1005, Dec. 2011.

[71] D. L. Bourell, T. J. Watt, D. K. Leigh, and B. Fulcher, "Performance Limitations in Polymer Laser Sintering," *Phys. Procedia*, vol. 56, pp. 147–156, 2014.

[72] K. V Wong and A. Hernandez, "A Review of Additive Manufacturing," *ISRN Mech. Eng.*, vol. 2012, p. 10, 2012.

[73] F. P. W. Melchels, J. Feijen, and D. W. Grijpma, "A review on stereolithography and its applications in biomedical engineering.," *Biomaterials*, vol. 31, no. 24, pp. 6121–30, 2010.

[74] I. Zein, D. W. Hutmacher, K. C. Tan, and S. H. Teoh, "Fused deposition modeling of novel scaffold architectures for tissue engineering applications," *Biomaterials*, vol. 23, no. 4, pp. 1169–1185, Feb. 2002.

[75] "Laminated Object Manufacturing (LOM)." [Online]. Available: http://blog.nus.edu.sg/u0804594/common-rp-techniques/laminated-object-manufacturing-lom/.

[76] C. K. Chua, K. F. Leong, and C. S. Lim, *Rapid Prototyping: Principles and Applications*. World Scientific, 2010.

[77] J. Banks, "Adding value in additive manufacturing: Researchers in the United Kingdom and Europe look to 3D printing for customization," *IEEE Pulse*, vol. 4, no. 6, pp. 22–26, 2013.

[78] B. C. Gross, J. L. Erkal, S. Y. Lockwood, C. Chen, and D. M. Spence, "Evaluation of 3D printing and its potential impact on biotechnology and the chemical sciences," *Anal Chem*, vol. 86, no. 7, pp. 3240–3253, 2014.

[79] R. J. Morrison, S. J. Hollister, M. F. Niedner, M. G. Mahani, A. H. Park, D. K. Mehta, R. G. Ohye, and G. E. Green, "Mitigation of tracheobronchomalacia with 3D-printed personalized medical devices in pediatric patients.," *Sci. Transl. Med.*, vol. 7, no. 285, p. 285ra64, 2015.

[80] L. Mertz, "Dream it, design it, print it in 3-D: What can 3-D printing do for you?," *IEEE Pulse*, vol. 4, no. 6, pp. 15–21, 2013.

[81] X. Cui, T. Boland, D. D. D'Lima, and M. K. Lotz, "Thermal inkjet printing in tissue engineering and regenerative medicine.," *Recent Pat. Drug Deliv. Formul.*, vol. 6, no. 2, pp. 149–55, 2012.

[82] I. T. Ozbolat and Y. Yu, "Bioprinting toward organ fabrication: challenges and future trends.," *IEEE Trans. Biomed. Eng.*, vol. 60, no. 3, pp. 691–9, 2013.

[83] B. Duan, L. A. Hockaday, K. H. Kang, and J. T. Butcher, "3D bioprinting of heterogeneous aortic valve conduits with alginate/gelatin hydrogels.," *J. Biomed. Mater. Res. A*, vol. 101, no. 5, pp. 1255–64, May 2013.

[84] G. T. Klein, Y. Lu, and M. Y. Wang, "3D printing and neurosurgery--ready for prime time?," *World Neurosurg.*, vol. 80, no. 3–4, pp. 233–5, Jan. 2013.

[85] C. L. Ventola, "Medical Applications for 3D Printing: Current and Projected Uses.," *P T*, vol. 39, no. 10, pp. 704–11, Oct. 2014.

[86] R. K. KULKARNI, "Polylactic Acid for Surgical Implants," *Arch. Surg.*, vol. 93, no. 5, p. 839, Nov. 1966.

[87] Z. Sheikh, S. Najeeb, Z. Khurshid, V. Verma, H. Rashid, and M. Glogauer, "Biodegradable materials for bone repair and tissue engineering applications," *Materials*, vol. 8, no. 9. pp. 5744–5794, 2015.

[88] L. G. Griffith, "Polymeric biomaterials," *Acta Mater.*, vol. 48, no. 1, pp. 263–277, 2000.

[89] C. Shi, Y. Zhu, X. Ran, M. Wang, Y. Su, and T. Cheng, "Therapeutic potential of chitosan and its derivatives in regenerative medicine.," *J. Surg. Res.*, vol. 133, no. 2, pp. 185–192, 2006.

[90] B. M. Chesnutt, A. M. Viano, Y. Yuan, Y. Yang, T. Guda, M. R. Appleford, J. L. Ong, W. O. Haggard, and J. D. Bumgardner, "Design and characterization of a novel chitosan/nanocrystalline calcium phosphate composite scaffold for bone regeneration.," *J. Biomed. Mater. Res. A*, vol. 88, no. 2, pp. 491–502, Feb. 2009.

[91] K. Rezwan, Q. Z. Chen, J. J. Blaker, and A. R. Boccaccini, "Biodegradable and bioactive porous polymer/inorganic composite scaffolds for bone tissue engineering.," *Biomaterials*, vol. 27, no. 18, pp. 3413–31, Jun. 2006.

[92] W. T. Godbey and A. Atala, "*In vitro* systems for tissue engineering.," *Ann. N. Y. Acad. Sci.*, vol. 961, pp. 10–26, Jun. 2002.

[93] A. M. S. Ibrahim, P. G. L. Koolen, K. Kim, G. S. Perrone, D. L. Kaplan, and S. J. Lin, "Absorbable Biologically Based Internal Fixation," *Clinics in Podiatric Medicine and Surgery*, vol. 32, no. 1. pp. 61–72, 2015.

[94] J. M. Brady, D. E. Cutright, R. A. Miller, and G. C. Barristone, "Resorption rate, route, route of elimination, and ultrastructure of the implant site of polylactic acid in the abdominal wall of the rat.," *J. Biomed. Mater. Res.*, vol. 7, no. 2, pp. 155–66, Mar. 1973.

[95] T. Barrows, "Degradable implant materials: A review of synthetic absorbable polymers and their applications," *Clinical Materials*, vol. 1, no. 4. pp. 233–257, 1986.

[96] J. E. Gough and S. Downes, "Osteoblast cell death on methacrylate polymers involves apoptosis," *J. Biomed. Mater. Res.*, vol. 57, no. 4, pp. 497–505, Dec. 2001.

[97] E. Mitzner, P. Albertus, H. Maria, C. Mueller, and D. Berlin, "Material properties and *in vitro* biocompatibility of a newly developed bone cement," *Mater. Res.*, vol. 12, no. 4, pp. 447–454, 2009.

[98] J. C. J. Webb and R. F. Spencer, "The role of polymethylmethacrylate bone cement in modern orthopaedic surgery," *J. Bone Joint Surg. Br.*, vol. 89, no. 7, pp. 851–7, Jul. 2007.

[99] M. Stańczyk and B. van Rietbergen, "Thermal analysis of bone cement polymerisation at the cement-bone interface," *J. Biomech.*, vol. 37, no. 12, pp. 1803–10, Dec. 2004.

[100] R. M. Khashaba, M. M. Moussa, D. J. Mettenburg, F. Rueggeberg, N. B. Chutkan, and J. L. Borke, "Polymeric-calcium phosphate cement composites-material properties: *in vitro* and *in vivo* investigations," *Int. J. Biomater.*, vol. 2, pp. 1–14, Jan. 2010.

[101] S. M. Kurtz, M. L. Villarraga, K. Zhao, and A. A. Edidin, "Static and fatigue mechanical behavior of bone cement with elevated barium sulfate content for treatment of vertebral compression fractures," *Biomaterials*, vol. 26, no. 17, pp. 369–712, Jun. 2005.

[102] M. Aviv, I. Berdicevsky, and M. Zilberman, "Gentamicin-loaded bioresorbable films for prevention of bacterial infections associated with orthopedic implants," *J. Biomed. Mater. Res.*, vol. 83, no. 1, pp. 10–19, 2007.

[103] T. Phromsopha and Y. Baimark, "Chitosan microparticles prepared by the water-in-oil emulsion solvent diffusion method for drug delivery," *Biotechnology*, vol. 9, no. 1, pp. 61–66, 2010.

[104] B. Szaniszlo, C. Iuga, and M. Bojiţă, "Indirect Determination of Neomycin by Derivative Spectrophotometry," *Clujul Med.*, vol. 84, no. 3, p. 398, 2011.

[105] K. K. Tappa, U. M. Jammalamadaka, and D. K. Mills, "Design and evaluation of a nanoenhanced anti-infective calcium phosphate bone cements.," *Conf. Proc. ... Annu. Int. Conf. IEEE Eng. Med. Biol. Soc. IEEE Eng. Med. Biol. Soc. Annu. Conf.*, vol. 2014, pp. 3921–4, Jan. 2014.

[106] U. Jammalamadaka, K. Tappa, and D. Mills, "Osteoinductive calcium phosphate clay nanoparticle bone cements (CPCs) with enhanced mechanical properties.," *Conf. Proc. ... Annu. Int. Conf. IEEE Eng. Med. Biol. Soc. IEEE Eng. Med. Biol. Soc. Annu. Conf.*, vol. 2014, pp. 3917–20, Jan. 2014.

[107] N. J. Dunne, J. Hill, P. McAfee, R. Kirkpatrick, S. Patrick, and M. Tunney, "Incorporation of large amounts of gentamicin sulphate into acrylic bone cement: effect on handling and mechanical properties, antibiotic release, and biofilm formation.," *Proc. Inst. Mech. Eng. H.*, vol. 222, no. 3, pp. 355–365, 2008.

[108] Y. K. Kim, H. H. Yeo, and S. C. Lim, "Tissue response to titanium plates: a transmitted electron microscopic study.," *J. Oral Maxillofac. Surg.*, vol. 55, no. 4, pp. 322–6, Apr. 1997.

[109] L. Wong, C. R. Dufresne, J. T. Richtsmeier, and P. N. Manson, "The effect of rigid fixation on growth of the neurocranium.," *Plast. Reconstr. Surg.*, vol. 88, no. 3, pp. 395–403, Sep. 1991.

[110] M. Taylor and K. E. Tanner, "Fatigue failure of cancellous bone: a possible cause of implant migration and loosening.," *J. Bone Joint Surg. Br.*, vol. 79, no. 2, pp. 181–2, Mar. 1997.

[111] M. Ribeiro, F. J. Monteiro, and M. P. Ferraz, "Infection of orthopedic implants with emphasis on bacterial adhesion process and techniques used in studying bacterial-material interactions.," *Biomatter*, vol. 2, no. 4, pp. 176–94, Jan. .

[112] J. Chevalier and L. Gremillard, "Ceramics for medical applications: A picture for the next 20 years," *J. Eur. Ceram. Soc.*, vol. 29, no. 7, pp. 1245–1255, Apr. 2009.

[113] P. Rokkanen, O. Böstman, S. Vainionpää, E. A. Makela, E. Hirvensalo, E. K. Partio, K. Vihtonen, H. Pätiälä, and P. Törmälä, "Absorbable devices in the fixation of fractures.," *J. Trauma*, vol. 40, no. 3 Suppl, pp. S123–7, Mar. 1996.

[114] O. Böstman, "Economic considerations on avoiding implant removals after fracture fixation by using absorbable devices.," *Scand. J. Soc. Med.*, vol. 22, no. 1, pp. 41–5, Mar. 1994.

[115] R. Huiskes, H. Weinans, and B. van Rietbergen, "The relationship between stress shielding and bone resorption around total hip stems and the effects of flexible materials.," *Clin. Orthop. Relat. Res.*, no. 274, pp. 124–34, Jan. 1992.

[116] L. Xiao, B. Wang, G. Yang, and M. Gauthier, "Poly(Lactic Acid)-Based Biomaterials : Synthesis , Modification and Applications," *Biomed. Sci. Eng. Technol.*, pp. 247–282, 2006.

[117] J. A. Weisman, J. C. Nicholson, K. Tappa, U. Jammalamadaka, C. G. Wilson, and D. K. Mills, "Antibiotic and chemotherapeutic enhanced three-dimensional printer filaments and constructs for biomedical applications.," *Int. J. Nanomedicine*, vol. 10, pp. 357–70, Jan. 2015.

[118] S. Nag and R. Banerjee, "Materials for medical devices, fundamentals of medical implant materials," *ASM Handb.*, vol. 23, pp. 6–16, 2012.

[119] J. A. Weisman, "Nanotechnology and additive manufacturing platforms for clinical medicine: An investigation of 3D printing bioactive constructs and halloysite nanotubes for drug delivery and biomaterials," Louisiana Tech University, 2014.

[120] J. P. Levine, "Long-term estrogen and hormone replacement therapy for the prevention and treatment of osteoporosis," *Curr. Womens. Health Rep.*, vol. 3, no. 3, pp. 181–186, 2003.

[121] P. Taxel, H. Kaneko, S. K. Lee, H. L. Aguila, L. G. Raisz, and J. A. Lorenzo, "Estradiol rapidly inhibits osteoclastogenesis and RANKL expression in bone marrow cultures in postmenopausal women: A pilot study," *Osteoporos. Int.*, vol. 19, no. 2, pp. 193–199, 2008.

[122] L. G. Raisz, "Pathogenesis of osteoporosis: Concepts, conflicts, and prospects," *Journal of Clinical Investigation*, vol. 115, no. 12. pp. 3318–3325, 2005.

[123] H. K. Väänänen and P. L. Härkönen, "Estrogen and bone metabolism," *Maturitas*, vol. 23, no. SUPPL. 1996.

[124] R. Pacifici, "Estrogen, cytokines, and pathogenesis of postmenopausal osteoporosis.," *J. Bone Miner. Res.*, vol. 11, no. 8, pp. 1043–1051, 1996.

[125] P. G. Bradford, K. V Gerace, R. L. Roland, and B. G. Chrzan, "Estrogen Regulation of Apoptosis in Osteoblasts," *Physiol. Behav.*, vol. 99, no. 2, pp. 181–185, 2011.

[126] T. Kameda, H. Mano, T. Yuasa, Y. Mori, K. Miyazawa, M. Shiokawa, Y. Nakamaru, E. Hiroi, K. Hiura, A. Kameda, N. N. Yang, Y. Hakeda, and M. Kumegawa, "Estrogen Inhibits Bone Resorption by Directly Inducing Apoptosis of the Bone-resorbing Osteoclasts," *J. Exp. Med.*, vol. 186, no. 4, pp. 489–495, 1997.

[127] C. Roggia, Y. Gao, S. Cenci, M. N. Weitzmann, G. Toraldo, G. Isaia, and R. Pacifici, "Up-regulation of TNF-producing T cells in the bone marrow: a key mechanism by which estrogen deficiency induces bone loss *in vivo*.," *Proc. Natl. Acad. Sci. U. S. A.*, vol. 98, no. 24, pp. 13960–5, Nov. 2001.

[128] M. Savvas, J. W. Studd, I. Fogelman, M. Dooley, J. Montgomery, and B. Murby, "Skeletal effects of oral oestrogen compared with subcutaneous oestrogen and testosterone in postmenopausal women.," *BMJ*, vol. 297, no. 6644, pp. 331–3, Jul. 1988.

[129] S. Furness, H. Roberts, J. Marjoribanks, and A. Lethaby, "Hormone therapy in postmenopausal women and risk of endometrial hyperplasia.," *Cochrane database Syst. Rev.*, vol. 8, no. 8, p. CD000402, 2012.

[130] C. Kailasam and D. Cahill, "Review of the safety, efficacy and patient acceptability of the levonorgestrel-releasing intrauterine system.," *Patient Prefer. Adherence*, vol. 2, pp. 293–302, Jan. 2008.

[131] "Intra Uterine Device." [Online]. Available: http://theodysseyonline.com/kalamazoo-college/straight-talk-having-iud/284090.

[132] J. E. Jelovsek, C. Maher, and M. D. Barber, "Pelvic organ prolapse," *Lancet*, vol. 369, no. 9566. pp. 1027–1038, 2007.

[133] B. Roehl and E. M. Buchanan, "Urinary incontinence evaluation and the utility of pessaries in older women.," *Care Manag. J.*, vol. 7, no. 4, pp. 213–7, Jan. 2006.

[134] M. Kokot-Kierepa, A. Bartuzi, B. Kulik-Rechberger, and T. Rechberger, "[Local estrogen therapy--clinical implications--2012 update].," *Ginekol. Pol.*, vol. 83, no. 10, pp. 772–7, Oct. 2012.

[135] "Pessaries." [Online]. Available: http://www.coopersurgical.com/Our-Brands/Milex.

[136] E. Braekevelt, B. P. Y. Lau, B. Tague, S. Popovic, and S. A. Tittlemier, "Effect of cooking on concentrations of β-estradiol and metabolites in model matrices and beef.," *J. Agric. Food Chem.*, vol. 59, no. 3, pp. 915–20, Feb. 2011.